MOLECULAR AND CELLULAR MAGNETIC RESONANCE IMAGING OF MYOCARDIAL INFARCT HEALING

MOLEKULARE UND ZELLULÄRE MAGNETRESONANZTOMOGRAPHIE DER WUNDHEILUNG NACH MYOKARDINFARKT

DOCTORAL THESIS FOR A DOCTORAL DEGREE
AT THE GRADUATE SCHOOL OF LIFE SCIENCES
JULIUS-MAXIMILIANS-UNIVERSITÄT WÜRZBURG
SECTION BIOMEDICINE

Submitted by

Yuxiang Ye

From Zhanjiang, China

Würzburg 2012

Submitted on: ……………………………………………

Members of the Promotion committee:

Chairperson: Prof. Dr. med. Manfred Gessler

Primary Supervisor: Prof. Dr. med. Dr. rer. nat. Wolfgang Rudolf Bauer

Supervisor (Second): Prof. Dr. rer. nat. Peter Michael Jakob

Supervisor (Third): Prof. Dr. med. Roland Jahns

Date of Public Defence: ………………………………

Date of receipt of Certificates: ………………………

Contents

Summary

Myocardial infarction (MI) is a leading cause of death worldwide. Timely restoration of coronary blood flow to ischemic myocardium significantly reduces acute infarct mortality and attenuates ventricular remodeling. However, surviving MI patients frequently develop heart failure, which is associated with reduced quality of life, high mortality rate (10% annually), as well as high healthcare expenditures. The main processes involved in the evolution of heart failure post-MI are the great loss of contractile cardiomyocytes during ischemia-reperfusion and the subsequent complex structural and functional alterations, which are rooted in modifications at molecular and cellular levels in both the infarcted and non-infarcted myocardium. However, we still lack efficient treatments to prevent the development and progression of left ventricular remodeling. The improved survival rate of acute MI patients combined with the lack of effective therapy for post-MI remodeling contributes to the high prevalence of heart failure.

Cardiac Magnetic Resonance Imaging (MRI) is an important tool for diagnosis and assessment of MI. With the advancement of this technology, the frontier of MRI has been extended to probing molecular and cellular events *in vivo* and non-invasively. In

combination with assessment of morphology and function, the visualization of essential molecular and cellular markers *in vivo* could provide comprehensive, multifaceted views of the healing process in infarcted hearts, which might give new insight for the treatment of acute MI. In this thesis, molecular and cellular cardiac MRI methods were established to visualize and investigate inflammation and calcium flux in the healing process of acute MI *in vivo*, in a clinically relevant rat model.

Healing of MI is a delicately orchestrated inflammatory process, in which monocytes are central effectors and regulators. In Chapter 3 of the thesis, fluorine-19 (^{19}F) MRI was utilized to unambiguously visualize the spatiotemporal distribution of monocytes and their descendant macrophages in reperfused MI complicated by microvascular obstruction (MVO) and intramyocardial hemorrhage (IMH), two strong indicators of poor prognosis. As in previous studies, we found that IMH and MVO were closely associated. However, they differ with respect to innate immune responses. While monocyte recruitment was observed proportional to the severity of ischemia-reperfusion injury when MVO was absent, a distinct mismatch was observed between the severity of the ischemia-reperfusion injury and monocyte recruitment in the MVO region. This result is surprising because monocyte infiltration is expected to be high in the severely damaged MVO; we observed that few monocytes were recruited to this region. Four weeks after MI of similar initial size, MVO hearts in comparison to those with only IMH, demonstrated significantly reduced recovery of ejection fraction, which was associated with more intense replacement fibrosis consisting of significantly less thick collagen fibers. The above findings support that MVO is a stronger predictor of worse functional prognosis after acute MI. However, the relationship between the increased post-MI fibrosis and the monocyte infiltration pattern of MVO hearts needs further investigation. The monocyte recruitment might present a potential diagnostic and therapeutic target that could be longitudinally monitored by the combination of ^{19}F-MRI and proton MRI.

During the healing process of MI, remodeling also takes place in structure and function of non-infarcted myocardium. As one of the most important ions in the ion

signal system of the heart, calcium signaling has been found to be altered in acute and chronic MI hearts. We improved and applied the quantitative manganese enhanced MRI (MEMRI) method in both sub-acute and chronic MI rats, to probe the influx and efflux of calcium in infarcted and non-infarcted myocardium *in vivo*. In addition, fundamental questions concerning the relationship between manganese ion infusion rate, its cumulative dose, and the enhancement of the spin-lattice relaxation rate constant (R1) in blood, myocardium and other tissues were addressed. We were able to reveal the R1 dynamics of infarcted and non-infarcted myocardium *in vivo* with high spatiotemporal resolution. Interestingly, significantly reduced R1 enhancement was observed in various tissues in sub-acute MI rats, in comparison to both control and chronic MI rats. This phenomenon seems largely, if not entirely, due to the significantly reduced manganese ion concentration in arterial blood in sub-acute MI rats. Moreover, we discovered that intravenous infusion rates of manganese significantly influence the change of R1 in blood and thus that of R1 in myocardium, given the same total infusion dose. These findings highlight the importance of relating R1 enhancement in myocardium to the changes of R1 in blood and the myocardial arterial perfusion, when interpreting quantitative MEMRI as a surrogate of calcium activities in myocardium.

Zusammenfassung

Myokardinfarkte (MI) sind eine der häufigsten Todesursachen weltweit. Eine rechtzeitige Wiederherstellung des koronaren Blutflusses im ischämischen Myokard reduziert signifikant die Sterblichkeitsrate akuter Infarkte und vermindert das ventrikuläre Remodeling. Überlebende MI-Patienten entwickeln jedoch häufig eine Herzinsuffizienz, die mit einer reduzierten Lebensqualität, hohen Sterblichkeitsrate (10% jährlich), sowie hohen Kosten für das Gesundheitssystem einhergeht.

Die Entwicklung der Herzinsuffizienz nach einem MI ist auf den hohen Verlust kontraktiler Kardiomyozyten, während der Ischämie-Reperfusion zurückzuführen. Anschließende komplexe strukturelle und funktionelle Veränderungen resultieren aus Modifikationen des infarzierten und nicht infarzierten Myokards auf molekularer und zellulärer Ebene. Die verbesserte Überlebensrate von Patienten mit akutem MI und das Fehlen effizienter Therapien, die die Entwicklung und das Fortschreiten des ventrikulären Remodelings verhindern, führen zu einer hohen Prävalenz der Herzinsuffizienz.

Die kardiale Magnetresonanztomographie (MRT) ist eine wichtige Methode zur Diagnose und Beurteilung des Myokardinfarktes. Mit dem technologischen

Fortschritt wurden die Grenzen der MRT erweitert, so dass es heute möglich ist, auch molekulare und zelluläre Ereignisse *in vivo* und nicht-invasiv zu untersuchen. In Kombination mit kardialer Morphologie und Funktion könnte die Visualisierung essentieller molekularer und zellulärer Marker *in vivo* weitreichende Einblicke in den Heilungsprozess infarzierter Herzen liefern, was zu neuen Erkenntnissen für ein besseres Verständnis und bessere Therapien des akuten MI führen könnte.

In dieser Arbeit wurden Methoden für die molekulare und zelluläre kardiale MRT-Bildgebung der Inflammation und des Kalziumstroms im Heilungsprozess des akuten Myokardinfarktes *in vivo* in einem Rattenmodel mit klinischer Relevanz etabliert.

Die Heilung des MI ist ein feinabgestimmter inflammatorischer Prozess, in dem Monozyten zentrale Effektoren und Regulatoren sind.

In Kapitel 3 dieser Arbeit verwendeten wir Fluor-19 (^{19}F)-MRT für die eindeutige Visualisierung der räumlichen und zeitlichen Verteilung von Monozyten und den aus ihnen hervorgehenden Makrophagen im reperfundierten MI, die durch mikrovaskuläre Obstruktion (MVO) und intramyokardiale Hämorrhagie (IMH), zwei starke Indikatoren für eine schlechte Prognose, gekennzeichnet sind. Es zeigte sich, dass IMH und MVO eng assoziiert sind, sich aber hinsichtlich der Antwort des angeborenen Immunsystems unterscheiden: in Regionen in denen keine MVO vorlag, war die Rekrutierung von Monozyten proportional zur Schwere des Reperfusionsschadens. In Regionen mit MVO zeigte sich jedoch eine eindeutige Diskrepanz zwischen der Schwere des Reperfusionsschadens und der hochgradigen Einschränkung der Monozyten-Rekrutierung. Vier Wochen nach einem MI ähnlicher anfänglicher Größe zeigten MVO-Herzen im Vergleich zu solchen mit nur intramyokardialer Hämorrhagie eine signifikant reduzierte Erholung der Ejektionsfraktion. Verglichen mit IMH-Herzen, hatten die MVO-Herzen deutlich mehr narbige Fibrose, welche aus signifikant weniger dicke Kollagenfasern besteht. Diese Ergebnisse unterstützen die These, dass die MVO nach einem akuten MI ein stärkerer Prädiktor einer schlechteren funktionellen Prognose ist.

Der Zusammenhang zwischen der erhöhten Postinfarkt-Fibrose und dem Monozyten-Infiltrationsmuster von MVO-Herzen bedarf jedoch weiterer Untersuchungen. Die

Monozyten-Rekrutierung könnte ein potentielles diagnostisches und therapeutisches Ziel darstellen, das über einen längeren Zeitraum mittels kombiniertem ^{19}F- und Protonen-MRT überwacht werden könnte.

Während des Heilungsprozesses nach einem MI findet auch ein Remodeling der Struktur und Funktion von nicht infarziertem Myokard statt. In akuten und chronischen MI-Herzen zeigen sich Veränderungen im Kalzium-Signalweg, dem wahrscheinlich wichtigsten Ionen-Signalsystem des Herzen. Wir optimierten eine Methode zur manganverstärkten MRT und nutzten sie in subakuten und chronischen MI-Ratten, um den Ein- und Ausstrom des Kalziums im infarzierten und nicht infarzierten Myokard *in vivo* zu untersuchen.

Im Weiteren befasst sich die Arbeit mit fundamentalen Fragen bezüglich des Zusammenspiels zwischen der Infusionsrate der Manganionen, deren kumulativer Dosis sowie der Erhöhung der Spin-Gitter Relaxationskonstante (R1) im Blut, Myokard und anderen Geweben. Wir konnten die R1-Dynamik des infarzierten und nicht infarzierten Myokards *in vivo* mit einer hohen räumlichen und zeitlichen Auflösung darstellen. Interessanterweise konnte, in sub-akuten MI-Ratten, im Vergleich zu Kontroll- und chronischen MI-Ratten, eine signifikant reduzierte R1-Erhöhung in verschiedenen Geweben beobachtet werden. Diesem Phänomen scheint zum größten Teil, wenn nicht gänzlich, eine signifikant reduzierte Manganionenkonzentration im arteriellen Blut von sub-akuten MI-Ratten zugrunde zu liegen. Darüber hinaus haben wir gesehen, dass bei gleicher Infusionsdosis, die intravenöse Infusionsrate von Mangan einen signifikanten Einfluss auf die Veränderung des R1 des Blutes und somit auch des R1 im Myokard hat. Diese Ergebnisse unterstreichen, dass es wichtig ist, die R1-Anreicherung im Myokard auf die R1-Veränderungen im Blut und auf die arterielle Myokardperfusion zu beziehen, wenn man die quantitative manganverstärkte MRT als Surrogat der Kalziumaktivität im Myokard interpretiert.

Chapter 1

Basics of Myocardial Ischemic Injury and Heart Failure

Myocardial infarction (MI) is a leading cause of death worldwide. Timely restoration of coronary blood flow to ischemic myocardium significantly reduces acute infarct mortality and attenuates ventricular remodeling. However, surviving MI patients frequently develop heart failure, which is associated with reduced quality of life, high mortality rate (10% annually), as well as high healthcare expenditures. The main processes involved in the evolution of post-MI heart failure are the great loss of contractile cardiomyocytes during ischemia-reperfusion and the subsequent complex structural and functional alterations, which are rooted in modifications at molecular and cellular levels in both the infarcted and non-infarcted myocardium. Unfortunately, we still lack efficient treatments to prevent the development and progression of left ventricular remodeling. The improved survival rate of acute MI patients combined with the lack of effective therapy for post-MI remodeling contributes to the high prevalence of heart failure[1]. In this chapter, the physiology, pathophysiology and clinical aspects of myocardial infarction and heart failure are briefly reviewed.

1.1 Myocardium

The heart functions as a pump to supply blood to both pulmonary and systematic circulation. It is comprised of three types of cardiac muscles: atrial muscle, ventricular muscle and specialized excitatory and conductive muscle fibers. The former two are the force sources of the pump function and the later one is featured by its automatic rhythmical electrical discharge capabilities, which can form or conduct action potentials. These muscle cells are connected by intercalated discs in parallel bundles and further arranged in helical sheets to compose two functional syncytiums: the atrial syncytium and the ventricular syncytium. The normal rhythmical impulse is generated in sinus node locating in right atrial wall and is delayed in atrioventricular (A-V) node before propagating to ventricles along A-V bundle, left and right bundles and finally to all parts of the ventricles via Purkinje fibers. The conduction delay in A-V node permits the atria to contract shortly ahead of ventricles, which is critical for pumping blood efficiently[2].

The primary function of cardiomyocytes is to contract. The excitation-contraction coupling is the fundamental physiological process to convert electrical stimulus to mechanical response in cardiac myocytes. The depolarization of the resting membrane potential of myocayte initiates this process by allowing a small amount of calcium ions (Ca^{2+}) entering the cell via long-lasting (L-type) calcium channels. This small amount of Ca^{2+} triggers the terminal cisternae to open the calcium-release channels and release a large amount of Ca^{2+}, which eventually results in 100-times increase of intracellular Ca^{2+} in concentration. The free calcium ions bind to Troponin-C (TN-C), induce the conformational change of troponin-tropomyosin complex that exposes a myosin binding site on actin, and result in adenosine triphosphate (ATP) hydrolysis and movement of actin relative to myosin. The actin and myosin filaments sliced past each other, so that the sarcomere length shortens, thereby myocardium contracts. As to the end of action potential, the calcium influx diminishes and the intracellular Ca^{2+} is pumped into sarcoplasmic reticulum (SR) actively by sarco-endoplasmic reticulum calcium ATPase (SERCA). The decreasing intracellular calcium concentration result in the removal of Ca^{2+} from TN-C, so that the change in conformation of troponin-tropomyosin complex and inhibition of actin-myosin binding, which allows the sarcomere to relax and restore its initial length[2-5].

The alterations of myocyte contractility by modulating calcium handling and myosin ATPase activity are classified as inotropy. The major mechanisms to alter inotropy are to regulate calcium entry into myocyte cytoplasm through L-type calcium channels and sarcoplasmic reticulum, the affinity of TN-C for calcium, myosin ATPase activity, and the re-sequester of calcium from cytoplasm by sarcoplasmic reticulum uptake and the efflux of calcium from myocyte. The rate of myocyte relaxation is termed lusitropy, which results from the rate of calcium removal from cytoplasm after its release by the sarcoplasmic reticulum[2, 4].

To organize the force generating muscle cells structurally and functionally in the heart, a complex extracellular matrix (ECM) consisting of a complex mixture of collagen fibrils, elastin, cells, large molecules, growth factors, cytokines, and extracellular proteases *etc*. is interspersed between cardiomyocytes. Besides connecting myocytes and aligning contractile elements, EMC prevents overextending and disruption of myocytes. In addition, it transmits force and generates tensile strength to avoid rupture. It is a dynamic entity that evolves and remodels in response to pathophysiology. For instance, myocardial hypertrophy, ischemic cardiomyopathy and chronic myocarditis are accompanied by excessive collagen deposition in EMC, which contributes to impaired heart function. EMC is also critical in mediating angiogenesis by the rich soluble and insoluble angiogenic molecules, as well as the essential receptor signaling pathways in regulating endothelial cells migration, infiltration, proliferation, survival and architectural organization to finally establish vascular morphogenesis[6-10].

1.2 Ischemia-reperfusion Injury

1.2.1 Ischemic Injury of Myocardium

The heart demands large amount of oxygen and metabolites to generate adequate ATP aerobically for the repetitive contraction and relaxation. At rest, the coronary arteries and its branches supply 5% of cardiac output to this organ, which counts for 0.4% of body weight. Under normal aerobic conditions, fatty acids supplies 60-90% metabolism for cardiomyotyes to produce ATP; and pyruvate from glycolysis and lactate oxidation constitutes to the rest needs. However, it has also been revealed that cardiac myocytes are very versatile in using substrates for aerobic metabolism. The weighting of carbohydrates, lactate, amino acids and ketones, rather than fatty acids, to supply energy for generating ATP could be dramatically increased when they are abundantly available in blood. Because cardiac myocytes extract 70-80% oxygen from hemoglobin, the oxygen extraction reserve is very limited. Therefore, an increased demand of oxygen and metabolic substrates due to increased contraction or heart rate is mostly delivered by increased coronary blood supply[11]. When coronary blood flow is interrupted completely (acute myocardial infarction), hypoxia swiftly shifts aerobic metabolism to anaerobic glycolysis, spontaneously with the decline and eventually the loss of myocyte contraction. Because the very limited substrate supplies for anaerobic glycolysis in ischemic myocardium and poor reserve of high-energy phosphate (HEP) in cardiac myocytes, ATP is quickly exhausted in ischemic zone. The lack of ATP results in sodium ions (Na^+) and chloride ions (Cl^-) retention and cell swelling by inhibiting sodium ion/potassium ion (K^+)-ATPase (Na^+/K^+-ATPase). The accumulation of acidic anaerobic metabolic products rapidly leads to the decline of intracellular pH. In addition, the intracellular osmotic load increases due to the boost of lactate and inorganic phosphate *etc*., and myocytes become edematous. The intracellular Ca^{2+} is believed to increase slightly in the late reversible phase[12]. In humans and large animals, an episode of 20 minutes (min) ischemia followed by reperfusion does not induce necrosis in myocardium. The prolonged ischemia before restoration of coronary circulation can cause partly (20minutes - 3 hours) to completely (3-6 hours) transmural necrosis in the involved ventricular walls[13-17].

1.2.2 Reperfusion Injury

In the past two decades, a series of systematic data from both experimental models and clinics convincingly showed that the timely restoration of blood supply to MI regions reduces MI size and improves the healing process, so that the improved clinical out-comes[18]. However, to reperfuse the infarcted myocardium seems unavoidably induce injuries[16]. The cardiac dysfunctions caused by reperfusion injuries are classified into four types: 1) myocardial stunning, which refers to the “mechanical dysfunction that persists after reperfusion despite the absence of irreversible damage and despite the restoration of normal or near-normal coronary flow”[19]; 2) microvascular obstruction (MVO), referring to the hypoperfused myocardial tissue despite the patent epicardial coronary vessel, due to functional or anatomical changes of coronary microcirculation[20]; 3) reperfusion arrhythmias; and 4) lethal reperfusion injury, referring to “myocardial injury caused by the restoration of coronary blood flow after an ischemic episode”[16].

The mechanisms of reperfusion injury have been investigated intensively in the past three decades. The following mediators have been found critical in the induction of reperfusion injury: 1) Reactive oxygen species (ROS). They are molecules with unpaired electrons in their outer orbit and are able to neutralize nitric oxide, damage myocytes and endotheliums directly and trigger inflammation. Stunned myocardium is thought to be injured mainly by oxidative stress. 2) Intracellular calcium overloading. Sarcolemmal membrane loses normal function of regulating calcium gradient crossing membrane due to ischemic injury. Moreover, sarcoplasmic reticulum is damaged by oxidative free radicals during reperfusion. Consequently, the Ca^{2+} concentration increased dramatically in cytoplasm and mitochondria, which in turn results in cell death. 3) Inflammation. The most recent evidence demonstrated that inflammasomes, the crucial signal to initiate inflammatory reaction after ischemia-reperfusion, was formed in cardiac fibroblasts rather than in cardiomyocytes. Their activation resulted in interleukin-1 production, which triggered the downstream inflammatory reactions in the heart[21]. These inflammatory signals in MI activate and facilitate neutrophils to attach to and transmigrate damaged microvasculature.

They produce large amount of free radicals and degradative enzymes that induce cell death and amplify inflammation. Neutrophil depletion in animal models of reperfused MI suggests that neutrophils might induce significant injuries to myocardium. The plugging of neutrophils is believed to be an important cause of MVO, a severe dysfunction of microvasculature in infarcted myocardium and a strong indicator of adverse left ventricular (LV) remodeling[22, 23]. Furthermore, pH value and metabolic modulation *etc*. were found to influence myocardial injury upon reperfusion after ischemia[16].

1.3 Inflammatory Response in Myocardial Infarction

Both reperfused and non-reperfused acute myocardial infarctions are associated with inflammatory response, which starts on-site shortly after the initiation of ischemia and lasts for weeks until the scar formation is finished[24]. In patients with chronic MI, systemic inflammatory markers have been found elevated, which is believed to contribute significantly to the development of heart failure[25].

The release of sub-cellular membrane components by MI activates complement system, induces the generation of ROS and triggers the activation of a series of cytokines and expressions of adhesion molecules, among which Tumor Necrosis Factor (TNF)-α, Interleukin (IL)-8 and Complement (C) 5a were found essential in regulating neutrophil recruitment after reperfusion. After activation, neutrophils marginate in blood stream, roll along capillary wall, attach to endotheliums and eventually transmigrate into injured myocardium. Cytotoxic effects can be induced by direct adherence of neutrophil to cardiac myocytes via Intercellular Adhesion Molecule (ICAM)-1 or by proteolytic enzymes and free radicals produced by neutrophils[24].

1.4 Healing of Injuries in Myocardium

Even though inflammation appears to be mostly detrimental during ischemia and shortly after reperfusion, it is necessary for the healing of myocardial injury. Mast cells and blood monocytes that are recruited to MI have been found essential in regulating and coordinating the healing process through modulating a series of cytokines, growth factors and other elements in inflammatory signaling[26, 27]. There are also data from both clinical and experimental settings suggesting that the enhanced inflammation after reperfusion therapy was beneficial for more effective healing[28, 29].

Blood monocytes are the key player in the healing of MI. They are recruited to MI by chemokines and their cognate receptors, among which Transforming Growth Factor (TGF)-β1 and Monocyte Chemoattractant Protein (MCP)-1 were found most important. The roles of monocytes and their descendent macrophages in MI healing were not elucidated until recent years, in part due to the heterogeneity and divergent functions of monocytes, as well as their unclear fate after releasing from bone marrow. Recently, researchers and clinicians become more aware that blood monocytes are a mixture of at least two but likely more than two subsets of mononuclear cells that share similar morphology but differ profoundly in functions. The two subsets of blood monocytes, inflammatory (or classical) and reparative monocytes, came into light in the past years. The corresponding cell populations have been identified in small rodents like mice, large animals like swine and in humans[30, 31]. The classical markers of the inflammatory monocytes are Ly-6C^{hi} (Gr1^{hi} CCR2^{+} CX3 CR1^{lo}) in mice and CD14^{+} CD16^{-} in humans. After effectively infiltrating sites of inflammation, they are potent in phagocytosis, proteolysis, and inflammatory functions. The reparative monocytes, counterpart of inflammatory monocytes, are identified by Ly-6C ^{lo} (Gr1^{lo} CCR2^{-} CX3CR1^{hi}) in mice and CD14^{+} CD16^{+} in humans. They are less virtuous in inflammatory functions but promoting angiogenesis, myofibroblasts proliferation and collagen deposition to heal the injured tissue with scar formation[30, 31]. Nahrendorf *et al.* revealed in a mouse MI model that these two subsets of blood monocytes were recruited to non-reperfused MI in a biphasic fashion: the Ly-6C ^{hi}

monocytes infiltrated MI mainly during the first phase (from Day 1-3 after MI) to break down necrosis and clear debris. In the second phase (from Day 4-7 after MI), the Ly-6C^{lo} monocytes prevailed, resulting in effective tissue repair[32]. These findings provide crucial mechanistic explanations in experimental MI for the seemly contradictory functions of the two subsets of monocytes but well-orchestrated recruitments and function for efficient MI healing[32]. Importantly, a similar recruitment pattern of the corresponding monocyte subsets were also found in acute MI patients with reperfusion therapy, even though the analysis was based on peripheral blood samples, rather than the direct examinations of monocytes in MI tissue[33].

Interleukin-10 (IL-10) and mast cells have been found important in modulating the inflammatory responses after MI. Known as a cytokine mainly produced by activated Th2 cells and endotoxin-stimulated monocytes, IL-10 is potent in inducing functional, morphological and phenotypical changes on monocytes and macrophages. It seems suppress inflammation by prohibiting activated monocytes to produce pro-inflammatory factors like IL-1α, IL-1β, TNF-α, IL-6, 8 and 12[34, 35]. In early stage after MI, mast cells degranulate to produce preformed histamine and TNF-α. In later phase of healing, they seem to be very important in coordinating healing by orchestrating cell-cell interaction, cytokines, growth factors and extracellular matrix proteins. Together with monocytes and macrophages, mast cells induce fibroblast proliferation and angiogenesis by providing an environment of cytokines and growth factors. However, the mechanism of mast cell accumulation in MI is still unclear[26].

In healing process, fibroblasts are critical in secreting extracellular matrix constituents to form the necessary supporting system allowing cell growth, angiogenesis and therefore nutrients delivery and cell metabolism. In MI, fibroblasts were found to develop ultrastructural and phenotypic features of smooth muscle cells. They are called myofibroblasts. They proliferate after being recruited to MI zone by a series of cytokines and growth factors secreted from monocytes and macrophages, mast cells, and lymphocytes[36]. This inflammatory environment also activates proteinases, which result in dramatic remodeling of the extracellular matrix of myocardium. The activation of proteinases such as urokinase-type plasminogen activator (uPA) and matrix metalloproteinase (MMP) have been found significant in this process[35]. The depletion of the activation of these proteinases was shown to attenuate adverse LV remodeling in mice[37].

1.5 LV Remodeling and Heart Failure

A key characteristic of myocardial tissue is the low regenerative capacity. Most myocardial cells are terminally differentiated soon after birth. Although discoveries in the past decade have demonstrated that adult cardiomyocytes can proliferate[38, 39] and there is a pool of resident cardiac progenitor cells, which can give rise to cardiomyocytes, endothelial cells and smooth muscle cells *in vitro* and *in vivo*, unfortunately they are insufficient for replacing the acute loss of a large number of myocardial cells. Rather, they seem to only participate in the continual replacement of apoptotic cardiomyocytes at a low basal level[40, 41]. As a consequence, the amount of contractile cells lost, or the infarct size, is a crucial determinant of adverse LV remodeling. The loss of 1g of myocardium represents approximately 20 million cardiomyocytes. 25% infarction of left ventricle causes heart failure[41].

Ventricular remodeling is central in the pathophysiology of heart failure development. In the early stage after MI, thinning and regional dilatation occurs in both infarcted and non-infarcted segments, resulting from slippage between muscle bundles and therefore the reduced number of cardiomyocytes distributed across the MI region[42-44]. Accompanied by a shift of cavity configuration from elliptical to more spherical, the enlarged LV chamber tends to maintain the cardiac output by increasing stroke volume. In later stage, myocardial hypertrophy becomes the predominant factor to compensate the heart performance, as LV chamber enlargement advances together with increasing cardiomyocyte apoptosis and interstitial fibrosis. Eventually comes the decompompensation phase, when the augmentation of heart function is insufficient and the cardiac output declines progressively in spite of the geometrical and histological changes of the heart[45]. The progressive LV remodeling and development of heart failure are also associated with up-regulation of numerous humoral factors, for example the rennin-angiotensin-aldosterone axis and the adrenergic nervous system and pro-inflammatory cytokines *etc*.

1.6 Clinical Needs

In the last three decades, a substantial decrease in early and late mortality in acute myocardial infarct patients has been achieved mainly due to the wide acceptance of the open-vessel theory[46]**,** emphasizing the need of early reperfusion of the infarct-related artery by means of percutaneous coronary intervention (PCI), intravenous thrombolytic therapy, or coronary artery bypass graft (CABG) surgery. Secondly, it is contributed by the availability of supportive medication adequately controlling life-threatening arrhythmias, preventing thrombo-embolic events, and reducing LV remodeling *e.g.* angiotensin-converting enzyme inhibition. Thirdly, cardiac revalidation and secondary prevention programs further reduce mortality[47]. Nevertheless, large multi-center studies have shown despite early and successful reperfusion and optimized medication, the actual hospital mortality remains approximately 7%[48]. Moreover, a sizable number of surviving MI patients develops toward ischemic dilated cardiomyopathy and heart failure, with permanently reduced quality of life. The survival and Ventricular Enlargement (SAVE) trial indicated that the long-term mortality of acute MI patients was still as high as 20% after 3.5 years, with treatment of angiotensin-converting-enzyme (ACE) inhibitor to reduce LV remodeling and progression of heart failure[49]. Therefore, on one hand more acute MI patients survived due to the effective acute treatment; on the other hand, currently available therapies are insufficient to treat those survivors chronically. This situation results in the increased number of heart failure patients. There is need to understand and treat heart failure better.

Chapter 2

Basics of Molecular and Cellular Cardiac Magnetic Resonance Imaging of Myocardial Infarction

According to the consensus of the American college of Cardiology (ACC) and European Society of Cardiology (ESC), myocardial infarction is diagnosed fundamentally by cardiac enzymes such as troponin I and T as well as creatine kinase-MB, and electrocardiography (ECG)[50]. However, cardiac enzymes are restrained by insensitivity in sub-acute MI, a lack of information on MI location and moderate association to MI size. In addition, ECG has limited sensitivity in MI absent of Q-wave and sometimes poor specificity in the setting of other cardiopulmonary abnormalities.

Medical imaging is valuable in assisting diagnosis, characterizing severity, guiding therapy, monitoring functional recovery and predicting long-term outcomes[51-54] of MI. Magnetic Resonance Imaging (MRI) has a relatively high spatiotemporal resolution and versatile tissue contrast. With increasing accessibility, cardiac MRI is becoming an important tool for diagnosis and assessment of MI in clinical routine, trials and research[52]. Cine MRI has been recognized as the golden standard to evaluate global contractile function of the heart[50]. Regional contractility can also be rendered by cine MRI or other MR techniques. Combined to MR contrast media, cardiac MRI is the preferred method to delineate MI and characterize microvascular function after ischemic insults[50, 52]. With the advancement of this technology, the frontier of MRI has been extended to probing molecular and cellular events *in vivo* and non-invasively[55]. In combination with the assessment of morphology and function, the visualization of essential molecular and cellular markers *in vivo* could provide comprehensive, multifaceted views of the healing process in infarcted hearts, which might provide new insights for the treatment of acute MI. Even though molecular and cellular MRI is mostly demonstrated in experimental animals, tremendous potential impact might be brought to clinical practice when molecular and cellular MRI is integrated to conventional cardiac MRI[56, 57].

In this thesis, molecular and cellular cardiac MRI methods were established to visualize and investigate inflammation and calcium flux in the healing process of acute MI *in vivo*, in a clinically relevant rat model.

2.1 Basics of Magnetic Resonance Physics

MRI is based on recording and analyzing radio signals emitted from nuclei in response to external magnetic fields[58]. The phenomenon of Nuclear Magnetic Resonance (NMR) was discovered by Bloch[59] and Purcell[60] independently in 1946. The rotation of a nucleus around its own axis is regarded as a spin, whose magnetic moment is of vectorial quantity. Quantum mechanics predicts that only a certain limited number of projections of a spin on a given axis are allowed. A resonance is induced when spins reach coherent frequency and phase, resulting in enhanced amplitude of magnetism. Conventionally, MRI exploit proton (^1H) to image anatomical and functional features of living bodies, due to the high natural abundance and large magnetic moment of proton.

At the absence of a static external magnetic field (B_0), the orientations of nuclear magnetic moments are random, which results in zero magnetization in the bulk tissue. However, in exposure to an external magnetic field, spins of nuclei allineate to B_0 gradually by circular movements, which is termed ‘Larmor precession’. The magnetic moment of the precessing nucleus (M) is expressed by a vector, which can be decomposed into the transverse (M_{xy}) and longitudinal (M_z) magnetization vectors. The Larmor frequency ω_L describes the frequency of precession of M around B_0. It is determined by the strength of the static external magnetic field B_0 in unit of teslar (T) and the gyromagnetic ratio γ in unit of megahertz per teslar (MHz/T).

$$\omega_L = \gamma B_0$$

For proton hydrogen, $\gamma = 42.576$ MHz/T.

In response to a static external magnetic field, the nucleus spins are either parallel or anti-parallel to B_0, presenting the discrete low or high energy level respectively. Spins favor the low energy state over the high energy state; therefore, the parallel magnetic moments are slightly more numerous over the anti-parallel ones in bulk matter, resulting in a parallel net magnetization. In the transverse plane, the magnetization vectors are canceled out due to the random distribution in phase. However, only transverse magnetic vectors can be measured by MRI scanners. Therefore, a strategy is needed to manipulate the net magnetization to produce a transverse vector detectable by MRI machine. For this, pulse radiofrequency (RF) waves with the Larmor frequency is applied by an RF magnetic field perpendicular to B_0. When a 90° RF pulse are applied, the longitudinal vector is flipped to the transverse plane and process coherently in phase, which emits a robust radiosignal of the Larmor frequency. When the RF pulse is interrupted, the spins start to lose phase coherence and return to equilibrium state. This is termed relaxation, which consists of two distinct and independent processes: the spin-lattice relaxation and the spin-spin relaxation. The former describes spins returning from the high to low energy state. The spin-lattice relaxation time constant (T1) is the time for 63% recovery of the longitudinal magnetization (M_z). The spin-spin relaxation reflects the decay of transverse magnetization (M_{xy}) due to the dephasing of the spins. The spin-spin relaxation time constant (T2) is the time for the longitudinal magnetization (M_z) decreases to 37% of its maximum strength.

The contrast of MRI is fundamentally based on the variation of T1, T2 and proton density (PD) in different tissues. By adapting parameters of the RF excitation and echo signal collection, MR images with different weightings of T1, T2 and PD components are produced. Repetition time (TR) is the time interval between excitation pulses. When TR is long, more of the energy from the excitation pulse is to vanish due to spin-lattice relaxation; therefore, the image is less T1 weighted. Echo time (TE) is the time between the excitation pulse and the maximum of the echo signal. A long TE allows spins to lose phase coherence more sufficiently and thereby generates stronger signal from tissue with long T_2. In addition, the inhomogeneity of magnetic field in approximate to spins can accelerate the dephasing of spins after turning off the excitation pulse, which is termed magnetic susceptibility or T2* effect. Relatively long TE permits apparent signal loss caused by inhomogeneity of local magnetic field on T2* weighted image (T2*WI). Worthy noted, T2* effect also shortens T2 of the local tissue. According to practical needs, different weighted images can be achieved by adjusting TR and TE, as well as modulating the schemes of MR sequences[61].

To image the heart with MRI, electrocardiography (ECG) and breath-hold are often needed to prevent image artifacts due to cardiac and respiratory motions. In small animals, breath control is often achieved by incubating the animal and ventilating by respiratory machines. Otherwise, a combination of respiratory and cardiac triggering system is needed instead. With the advance in acquisition and post-processing technologies, cardiac and respiratory motion artifacts can also be avoided by continuous signal acquisition but selective post-construction[62].

2.2 Conventional Cardiac MRI of Myocardial Infarction

In known or suspected MI patients, cardiac MRI can provide comprehensive morphological and functional evaluations of the heart by the determination of MI location, size and transmurality, as well as critical information associated with microvascular pathophysiology, for instance edema, intramyocardial hemorrhage (IMH) and microvascular obstruction (MVO). Besides being a powerful imaging modality in diagnosis and assessment of MI, cardiac MR (CMR) has also been increasingly applied in clinical trials to measure surrogate end points for instance CMR derived infarct size and pump function[52].

2.2.1 Global and Regional Ventricular Function

Coronary artery occlusion initiates an immediate loss of contractility in the ischemic myocardium. The global ventricular function post MI is decided by the extent of myocardial necrosis, amount of stunned myocardium and impact on contractility in the remote, non-infarcted myocardium. Ventricular remodeling takes place over time after infarction, in which functional, morphological and geometrical changes of the heart are determined by numerous parameters including size, location and transmurality of infarct, MVO and area at risk *etc*. The magnitude of potential functional recovery needs to be measured in the order of a few percentages[63, 64]. Presently, Cine MRI is the favorable technique to evaluate ventricular volume and function fully quantitatively. With that, Significantly smaller samples could provide the same statistical power to assess ventricular remodeling[65, 66].

Systolic contraction of myocardium induces ventricular wall thickening, circumferential and longitudinal shortening, resulting in a complex three dimensional deformation of myocardial wall[23, 67]. The above contraction parameters are attenuated or abrogated by reversible or non-reversible local injuries of myocardium. Therefore, they can serve to describe or monitor regional contractile function. Alternatively, regional ventricular function can be evaluated by regional EF parameter, which describes the contribution of the infarct myocardium to the ejection of blood. All the above data on regional function can be extracted from the same Cine MRI data used for quantification of global volumes and function.

2.2.2 Characteristics Determining Infarct Severity

Infarct severity is mainly determined by infarct volume and infarct transmurality. In addition, infarct location and microvascular obstruction are also determinants of worse adverse LV remodeling and clinical outcomes: anterior MI was found associated with more LV remodeling and worse outcome, in comparison to non-anterior MIs; the presence of MVO was correlated to early post-MI compilations, LV remodeling and poor recovery of heart function independent on MI size[23, 68]. Other parameters that might influence outcome are post-reperfusion intramyocardial hemorrhage and the ratio of infarct size to area-at-risk. IMH is found correlated to extensive adverse remodeling of LV, even though it is still a debate whether its prognostic value is independent of MI size and MVO[69-72]. The amount of viable myocardium (stunned myocardium) in the initial ischemic region can be estimated by the infarct to area-at-risk ratio[73].

Contrast enhanced (CE) MRI based on gadolinium contrast agent and inversion-recovery (IR) gradient-echo MR sequence is the preferred technique to delineate, characterize and monitor myocardial infarcts in both acute and chronic settings[74-77]. Infarct volume, transmurality, circumferential and longitudinal extents, and their changes over time can be excellently assessed. MVO is visible as a dark zone in the infarct core on the early CE MRI. Contrast agents could slowly fill in over time[78] or MVO could persist even in late enhancement phase. Recent clinical data suggested that MVO on late enhancement phase had stronger prognostic value on worse clinical outcomes[79, 80]. An additional T2-weighted MRI provides estimation of the extent of edematous myocardium after ischemic insult. Edema appears hyperintense signal. The presence of intramyocardial hemorrhage in concomitant to edema appears as a central hypointense core surrounded by hyperintense rim[73, 81, 82] on T2WI or signal voids on T2*WI.

2.2.3 Infarct Expansion, Shrinkage and Remodeling

As early as the first hours after ischemia, myocardial infarction, especially the large and transmural ones, undergoes infarct expansion due to the slippage between muscle bundles and therefore the reduced number of cardiac myocytes across the infarcted LV wall. Necrosis is phagocytized by macrophages and the preexisting extracellular matrix is digested by proteases. Progressively, wounded myocardium is replaced by granulation tissue, which contains a large number of fibroblasts and myofibroblasts producing new collagen fibers. In the weeks and months thereafter, the infarct remodels and matures into an anisotropic scar consisting of high density of type I collagen bundles. During this process, infarct shrinkage occurs due to the absorption of necrosis and the dramatic change of tissue composition in MI, which often lead to a volume loss of 30 to 60%[83]. Valuable information concerning MI expansion, shrinkage and remodeling, rendered by infarct volume, infarct transmurality, infarct surface, circumferential and longitudinal infarct length, infarct radii of curvature in longitudinal/circumferential direction, can be obtained by CE-IR MRI in combination with cine MRI in follow-up studies.

2.3 Molecular and Cellular Cardiac MRI

Molecular imaging is to visualize, characterize and non-invasively measure biological processes at the molecular and cellular levels in humans and other living systems[56]. The past two decades have witnessed a dramatic development of this domain, with the ever advance of imaging hardware and software, contrast agent synthesis and new knowledge of specific biomarkers of pathophysiological processes. The conventional medical imaging modalities are nuclear imaging, ultrasound imaging, X-ray computer tomography (CT), MRI/magnetic resonance spectroscopy (MRS). In addition, the integrated multi-modality imaging systems like CT-PET, CT-SPECT and PET-MRI provide more convenient image registration, facilitate interpretation of multi-modality images, and improve in-depth understanding of pathophysiological processes in a systematic manner. They have potential to significantly impact early and sensitive diagnosis, as well as individualized therapy. In addition, *in vivo* optical imaging approaches, including fluorescence and bioluminescence imaging, have demonstrated unique advantages of good molecular sensitivity and favorable chemistry for the development of molecular imaging agents[56, 57].

Molecular and cellular MRI detects molecular and cellular events with the advantages of being non-invasive, tomographic, non-ionizing and excellent soft tissue contrast, as well as high spatial and temporal resolutions. With contrast agents that can modulate MR signal by magnetically modifying the interaction of tissue water and the surrounding environment, either positive or negative enhancement could be achieved for visualization of molecular and cellular activities. In cardiovascular system, preclinical applications of molecular and cellular MRI have been demonstrated in calcium channel activity of cardiac myocytes, stem cell and immune cell tracking, detection of cardiac myocyte apoptosis, myeloperoxidase activity as well as imaging and monitoring of atherosclerosis. These molecular and cellular MRI methods have been applied to acute and chronic myocardial infarction, myocardial stunning, acute and chronic rejection of allograph heart transplantations, auto-immune myocarditis, as well as ApoE$^{-/-}$ mice *etc*.

Of the above mentioned molecular and cellular MRI methods and their applications in various disease models, the fundamental techniques can be classified into the following three categories:

1. MRI cell tracking.
2. MR imaging of pathophysiological processes with targeted contrast agents.
3. Calcium influx and efflux measurements by manganese enhanced MR imaging and R1 mapping.

2.3.1 MRI Cell Tracking

Medical imaging is largely based on tissue differences in contrast, enabling to identify anatomical structure, to differentiate healthy tissue from pathological ones, and visualize disease processes. In ^{1}H-MRI, a significant difference of relaxation (T1, T2 or T2*) between the target cells and the hosting tissue is needed to create enough contrast between the two, in order to visualize the target cells. A variety of approaches have been proposed to generate MR contrast for cell tracking**.** Both paramagnetic (*e.g.* gadolinium chelates[84-88], manganese chloride[89]) and superparamagnetic agents e.g. iron oxide agents have been linked or incorporated to target cells, in order to change T1 or T2/T2* values. Besides the above direct labeling methods by using external paramagnetic or superparamagnetic agents, reporter genes have been developed for MR cell tracking in preclinical setups. Typically, they were engineered into cells to produce markers for MR cell tracking[90-93]. At present, iron oxide particles varied in diameters are the predominant agents for MRI cell tracking, due to the bio-compatibility, high sensitivity and readily available setups in clinical MRI scanners. However, this method suffers from non-specificity, difficulty in absolute quantification of cells and incapability of differentiating multiple cell populations.

Instead, fluorine-19 (^{19}F) labeling for MR cell tracking is an attractive alternative, which overcomes some of the limitations of iron oxide particle labeling and has potential for clinical translation[94].

2.3.1.1 Cell labeling with iron oxide nano-particles

Although there are a few papers reporting the utility of paramagnetic MR contrast agents, such as gadolinium (Gd) chelates[84-88] and manganese chloride ($MnCl_2$)[89], for intracellular labeling, their use is hampered by the low sensitivity on T1 weighted images, the requisite of a very high intracellular concentration to shorten T1 times of surrounding water molecules, and the concern of toxicity in free ion status. Iron oxide nanoparticles, a superparamagnetic agent, are dominant in MR cell tracing, because of its robust effect on MR relaxivity, biocompatibility and easy accessibility. Besides shortening T1 and T2 values at high concentration, these iron contents have remarkable T2* effects. The strong superparamagnetic nature of these iron oxide nanoparticles generates local field gradients, which enhance dephasing of surrounding spins and produce significant signal loss (signal voids) on T2* weighted images. By incorporating with iron oxide agents, cells of interest are visible as hypointense areas on T2/T2* weighted MRI[95]. After being transplanted, cells labeled by iron oxide nano-particles could be isolated from homing tissue by tissue digestion and magnetic cell sorting, which gives a means to quantify and future characterize labeled cells[96].

Iron oxide nano-particles are a family of superparamagnetic contrast agents, consisting of a ferrite (maghemite or magnetite) core and a polymeric coating. Based on their size, they are categorized as monocrystalline iron oxide nanoparticles (MION, 10-30 nm in diameter)[97], ultra-small superparamagnetic iron oxide (USPIO, 10-40 nm in diameter)[97, 98], superparamagnetic iron oxide (SPIO, 60-150 nm in diameter)[99, 100] and mircometer-sized iron oxide particles (MPIO, around 1 to few micrometers in diameter)[101]. Among them Ferucarbotran (Resovist®) and Ferumoxides (Endorem® and Feridex®) were FDA approved clinical grade reagents for enhancing MRI detection of liver tumors[102] and metastatic lymph nodes[103]. Unfortunately, they have been withdrawn from the market. Recent attempts have demonstrated the novel applications of USPIO in inflammatory diseases[104], microcirculation permeability[105], blood volume[106] and MR angiography[98].

Direct labeling with (U)SPIO particles remains the most commonly used strategy for MRI cell trafficking in cardiovascular system. It is a relatively simple method, allowing for fast and sensitive detection. However, it bears some limitations and shortcomings. As mentioned above, any signal loss arising from other origins (*e.g.* noise, hemorrhagic myocardial infarcts, the heart-lung interface) may interfere with the detection of (U)SPIO labeled cells[107]. In particular, IMH is a frequent finding in MI patients after reperfusion therapies[78, 108-110]. It could interfere with the visualization of iron oxide labeled cells[111]. The paramagnetic and superparamagnetic properties of hemoglobin breakdown products (*e.g.* methemoglobin, ferritin, hemosiderin) can induce local field heterogeneity and create signal voids on T2*-weighted images. Such signal voids appear similarly to the signal loss caused by iron oxide nanoparticle labeled cells. Although seldom mentioned in previous studies[112-114], caution should be taken when interpreting MRI cell tracking using iron oxide particle labeling, in experimental reperfused MI models. The presence of T2* effect in reperfused MI zone could be caused by IMH. This is a concern for clinical translation of iron oxide particle labeling, because the majority of acute MI patients receive reperfusion therapy in Europe and North America. Moreover, it should be emphasized that iron oxide particles do not provide direct information concerning cell survival, proliferation, differentiation and quantification. It is also impossible to differentiate two or more groups of cells which are all labeled by iron oxide agents. In addition, every subsequent cell division will halve the intracellular iron content and result in gradual reduction of the cell detection. Therefore, direct cellular labeling with iron oxide is probably suitable for short-term cell tracking *e.g.* to locate labeled cells within the heart. Since the labeling is non-specific, iron contents could be passed on to surrounding cells *e.g.* macrophages or simply distributed extra-cellularly, which could produce false positive signals. False negative results may occur, as a result of partial volume effects or when the amount of labeled cells is too low in one imaging voxel.

2.3.1.2 MR reporter genes

Direct cell labeling has several advantages, such as ease of manipulation and potential for use in the clinical setting. However, it does not fulfill the demands of providing in-depth insight in cell survival, proliferation and differentiation. As mentioned above, iron contents or other labeling materials are diluted as cells divide. Moreover, the intracellular incorporated contrast agents may be removed by a variety of pathways and eventually unable to create enough contrast. Therefore, the direct approach may not be ideal for long-term cell labeling. Reporter gene imaging in combination with MRI or MRS seems more suitable for long-term cell labeling in the preclinical setting. Using a transgene approach *e.g.* replication-defective adenovirus, genes are incorporated into the cellular DNA. The products of the reporter genes (*e.g.* enzymes, surface markers, membrane receptors) are expressed only in viable labeled cells. They may potentially reflect the function and differentiation status in a quantitative fashion. Moreover, offspring cells can be traced, as long as the engineered reporter gene incorporated into chromosomes is not silent or blunt. The above advantages make transgenic labeling strategies highly valuable for answering questions concerning the long-term fate of labeled cells. At present, MR reporter genes are still limited to pre-clinical research, because of the restrictions of sufficient bio-safety profile.

Earlier attempts to transfect enzyme (creatine kinase – arginine kinase) genes to host tissues showed that products of incorporated genes were detectable by ^{31}P-MRS *in vivo*. Unfortunately, the interference of background tissue signal restricted their application. In addition, MRS does not provide spatial distribution of the marker, which makes enzyme reporter gene MRS less favorable for cell trafficking. In hunting reporter genes for MRI, a breakthrough was the ferritin gene[91, 92]. Ferritin is a metalloprotein consisting of 24 subunits, both light and heavy chains, and can coat up to 4500 Fe^{3+} ions. Unlike SPIOs, ferritin is predominately anti-ferromagnetic, resulting in a T2/T2* shortening several orders smaller than that of SPIOs. Cohen *et al.* were able to create a construct of TET-EGFP-HA-ferritin, in which tetracycline (TET) regulated tightly the expression of enhanced green fluorescent protein (EGFP) and influenza (HA) hemaglutinin-tagged ferritin heavy chain. When TET was retrieved, dramatic increases of both spin-lattice (R1) and spin-spin (R2) relaxation rates were detected in transfected rat glioma cells[91]. Over-expression of ferritin heavy chain could result in redistribution of intracellular iron and increase of intracellular iron contents, probably by up-regulating the transferrin receptor expression[91]. Almost at the same time, Genove *et al*. reported their success of delivering ferritin transgenes with a replication-defective adenovirus vector. After stereotactical injection of the adenovirus containing the ferritin reporter gene in the striatum of mice, robust contrast was seen on T2 and T2* weighted images, from 5 days to at least 39 days after injection[92]. This technique has also been applied to label stem cells for MRI cell tracking in animal models of ischemic cardiomyopathy. Tannous *et al*. generated a novel reporter gene expressing a cell surface receptor allowing monitoring gene expression and cell targeting[90]. Metabolic biotinylation of cell surface receptors can be used for *in vivo* imaging. Linking multi-modality contrast agents to avidin, which has an affinity 10^3-10^6 higher than the antigen-antibody interaction, provides signal enhancement in fluorescent imaging, MRI, PET and SPECT[90]. Although initially designed for monitoring gene expression in gene therapy, reporter genes are potentially translatable for cell labeling. They are promising for long-term observations of cell distribution, proliferation and differentiation.

2.3.1.3 ^{19}F-MRI for cell tracking: an attractive alternative

^{19}F-MRI may be highly attractive for cell trafficking. Owing to a high gyromagnetic ratio of 40.05MHz/T and a spin ½ nucleus, ^{19}F has 0.83 NMR sensitivity relative to proton and is naturally abundant. The advantage of using ^{19}F-MRI over ^{1}H-MRI is the lack of NMR signal of endogenous fluorine, with other words there is no background signal and ^{19}F-labeled cells are shown as 'hot spots' against a dark background[115, 116]. Moreover, it has the potential to quantify the labeled cells *in vivo*, based on ^{19}F-MR spectroscopy or calibrated MRI data[115, 117]. Anatomical localization of labeled cells can be achieved by superposing ^{19}F-MRI on ^{1}H-MRI. Because various perfluorocarbon (PFC) compounds with distinct profiles of MR spectrum are available for cell labeling, multiple cell populations could be detected and quantified by simultaneous or separated MR measurements[115, 117]. ^{19}F-MRI might bring interesting biological insights beyond the location and quantification of target cells, due to the versatile contrast rendered by the reaction of PFC to surrounding biological and chemical environments. For instance, ^{19}F-MRI using perfluorocarbon has been applied to report the pO_2 in tumor micro-environment[118]. This could be extended to provide information about the reaction and behavior of engrafted cells in homing tissue. PFC emulsions, originally developed for red blood cell substitute, should be well tolerated (a maximal safe dose of 3ml/kg administrated intravenously in human beings)[119].

The first report on *in vivo* ^{19}F-MRI cell tracking was as early as in 1997 by Noth *et al*[120]. In this serial *in vivo* study, macrophage tracking by ^{19}F-MRI was demonstrated in a rat model of adoptive transfer experimental allergic encephalomyelitis (AT-EAE). Macrophages were labeled *in situ* by intravenous injection of PFC emulsion (perfluoro-15-crown-5-ether). However, this novel method has not drawn much attention until Ahrens *et al*. applied *in vitro* PFC labeling on dendritic cells and demonstrated the capability of ^{19}F-MRI and ^{19}F-MRS in monitoring the distribution and migration of labeled cells *in vivo* in mice in 2005. Shortly thereafter, *in vivo* ^{19}F-MRI and MRS for cell tracking have gained much renewed interests. Both the *in situ* and *in vitro* labeling approaches of PFC emulsion have been applied in various animal models in both high magnetic field (11.7 T) and clinical (1.5 T) field strength. Similarly to the method demonstrated by Noth *et al*., Flogel *et al*. have shown the feasibility of imaging inflammation in cerebral stroke and non-reperfused MI in mouse models by ^{19}F-MRI at 9.4 T, after *in situ* labeling of phagocytes in peripheral blood by using PFC emulsion[121]. They also applied this method on early detection of inflammation in lungs[122], allograft heart rejection[123] and rheumatoid arthritis in mouse models. The *in situ* labeling method is simple, avoiding potential risks of altering delicate functions of cells by *in vitro* manipulation. However, it has limited applications mainly on labeling phagocytes in circulating blood. Therefore, the *in vitro* PFC labeling strategy is often needed for cells without strong phagocytotic capability (*e.g.* T lymphocytes, progenitor cells, tumor cells). After *in vitro* labeling by PFC, Srinivas *et al*. demonstrated *in vivo* imaging and absolute quantification of diabetogenic T cells homing to the pancreas in the nonobese diabetic mouse, an established model of type 1 diabetes[124]. This approach has been further extended to trace transplantation of progenitor cells. Ruiz-Cabello showed that neural stem cells could be visualized by ^{19}F-MRI till

Day 14 after transplantation in mouse brain[125]. In addition, Partlow and colleagues demonstrated that cells labeled by PFC could be detected by ^{19}F-MRI at a clinical 1.5T MRI scanner. They also showed the capability of ^{19}F-MRI to distinguish two populations of stem cells labeled with two different PFCs by using spectral discrimination at 11.7 T[117]. Being highly specific due to the lack of background signal, ^{19}F-MRI for cell tracking shares the advantage of nuclear labeling, but is superior in providing precise anatomical localization and tissue characterization by seamless and straight forward registration with ^{1}H-MRI.

Currently, no apparent bio-effects were observed on viability and function of dendritic cells and mononuclear cells after PFC incorporation, either *in vitro* or *in vivo* [115, 117].

As a non-specific labeling, ^{19}F agents and iron oxide nanoparticles share some similar shortcomings such as dilution of intracellular labeling following cell division and passing of contrast agents to surrounding cells. Besides the availability of ^{19}F coils, software modifications are needed to adapt conventional ^{1}H-MRI systems working for ^{19}F imaging. Moreover, ^{19}F labeling is not as sensitive as iron oxide labeling in general. Despite the above, the application and development of ^{19}F-MRI and MRS for cell trafficking have been carried out in a variety of institutes and manufactures. To increase sensitivity of ^{19}F labeled cell detection, some of the iron oxide labeling strategies may be adopted. For example, transfection agents (TA) have been shown to achieve 26-fold-increase of intracellular ^{19}F loading[115]. Moreover, the addition of Gd-DTPA administered intravenously shortens ^{19}F-T1, which may enhance ^{19}F signal intensity and reduce imaging time. The increasing magnetic field strength of clinical MR scanners should allow a faster and more sensitive cell tracing with ^{19}F-MR imaging and spectroscopy.

2.3.1.4 Strategies to increase intracellular loading of tracer/contrast agents

For cellular MRI, the minimal number of cells to be detectable relies in part on the average intracellular loading of MR tracer/contrast agents. Given the same coating material, it has been shown that the efficiency of iron labeling increases with the increasing size of iron oxide nanoparticles[126], probably due to the increase of phagocytosis and endocytosis. However, it is unclear if a similar relationship applies to PFC emulsion labeling. Moreover, the coating materials may influence the cellular internalization of tracer/contrast agents[127]. Higher iron loading may be achieved by increasing the dose of SPIO and prolonging incubation time. However, impaired cell viability and proliferation were observed in some of these settings, probably resulting from elevated levels of free radical. In addition, the majority of cell types used for stem cell research are non-phagocytes, which are not ready to uptake SPIOs or only internalize these nano-particles at a very low rate through pinocytosis. Therefore, efficient methods to facilitate cellular uptake of MRI tracer/contrast agents are needed.

In the current stage, a combination of SPIO particles and polycationic transfection agents (TAs) is the most widely applied strategy to enhance the efficiency of iron oxide labeling[128]. Coated by negative charged polymeric, most SPIO particles do not spontaneously attach to the negatively charged cellular membrane. Being developed for facilitating macromolecule uptake into cells, transfection agents are highly positive charged macromolecules. They form complex with SPIO upon proper preparation. This positive charged complex of SPIO and TA spontaneously attaches to cellular membranes through electrostatic interaction and effectively shuttles SPIO particles into cells by endocytosis[128].

Unfortunately, the production of the two US Food and Drug Administration (FDA) approved SPIOs, Feridex I.V.® (also known as Endorem® and ferumoxides) and Resovist® (also known as Cliavist®), have been discontinued in 2008 and 2009, respectively. After that, Thu *et al*. proposed a new means that combines three FDA-approved drugs—ferumoxytol, heparin and protamine—in serum-free medium to form self-assembling nanocomplexes that effectively label cells for MRI cell tracking[129].

2.3.1.5 Bio-effects of Cell labeling with TA

Cell labeling with iron oxide holds promise for rapid translation from bench to bedside. However, extensive toxicity tests and pre-clinical examinations are required for every protocol and cell type before clinical application. The FDA-approved SPIO agents (Feridex®, Resovist® and Endorem®) are cleared mainly by the reticuloendothelial system, which is capable of metabolizing excess iron. However, non-phagocytic cells may not tolerate intracellular iron overloading. Additionally, the SPIO and TA complex is considered as a combination of two FDA-approved agents; therefore, further regulatory approval is required. A variety of cell types did not exhibit significant changes in viability, proliferation, differentiation and other vital functions after magnetic labeling with SPIO-TA combinations. However, Kostura *et al.* observed a dose-dependent inhibition of chondrogenetic differentiation in human mesenchymal stem cells (MSC) using a Feridex-Poly-L-lysine (PLL) complex labeling but not with solo treatment of PLL[130]. Arbab *et al.* on the other hand reported that MSC chondrogenetic differentiation was affected only when Feridex-PLL complexes were not completely washed away before differentiation[131]. Most likely, residual Feridex-PLL complexes sticking on cellular membranes may be responsible for the impaired differentiation[132]. Although this controversy has not been fully elucidated, it underscores the necessity of careful evaluation on labeling methods of the cell type intended to be used before clinical trials. Caution must be taken to draw preliminary conclusions from pre-clinical studies when cell labeling procedures are applied.

Besides combining TAs, other approaches have been explored to improve SPIO internalization. Most of them rely on modification of the surface coating of particles. For instance, iron oxide loading was significantly increased when monoclonal antibodies were conjugated to SPIO to target specific receptors on cellular membrane surface. The intracellular uptake of SPIOs was increased by endocytosis mediated by receptor binding[133]. In addition, magnetoelectroporation devices were used to enhance the internalization loading of SPIO. Originally, these devices were developed to increase the penetration of DNA and chemotherapeutic drugs through cellular membranes. Walczak *et al.* demonstrated that magnetoelectroporation devices could quickly create intracellular endosmosis containing SPIO particles without the aid of TAs in various non-phagocyte populations[134, 135]. However, a recent report suggested that the *in vitro* differentiation of embryonic stem cells may be affected by the combination of magnetoelectroporation and ferumoxide, although cellular viability, proliferation and apoptosis were not affected[136]. Therefore, further investigation is warranted to assess the bio-effects of these cellular label methods *in vitro* and *in vivo*.

2.3.1.6 Detection sensitivity of MRI cell tracking

The sensitivity of MRI cell tracking is determined by various factors: the type of cellular tracer/contrast agent, the intracellular loading of tracer/contrast agent, the MRI sequence, the spatial resolution, the magnetic field strength and the heterogeneity of tissue background *etc*.

Among the several available cellular tracer/contrast agents, iron oxide particles deliver the highest sensitivity for MRI cell tracking when Gradient Echo (GE) sequence is applied, especially with high spatial resolution at higher magnetic field. However, its sensitivity is significantly reduced when background tissue has low proton density *e.g.* in lungs or original susceptibility effects *e.g.* hemorrhagic MI. It has been demonstrated that as few as 100 transplanted cells in the rat brain could be clearly seen by USPIO labeling, using a 3D GE sequence, a 98µm isotropic resolution and an intracellular iron load of approximately 7.1pg Fe/cell at 17.6-T[137]. The feasibility of single cell detection *in vivo* has also been demonstrated by MPIO labeling. At 4.7-T, single macrophages labeled by MPIO could be detected *in vivo* in an allograft heart rejection model in rats with an in-plane resolution of 156µm[138]. A few studies reported that single cells labeled by iron oxide particles could be visualized *in vivo* in small animal models at 1.5-T. But these were done in static organs, such as the brain[107]. It is very challenging to achieve such goal in the beating heart at clinical MRI scanners, because motion artifacts, relative low signal to noise ratios and a large voxel size may all seriously hamper the detection sensitivity. In a pig model of acute MI, Hill *et al.* found that a minimum of 1×10^5 intramyocardially injected mesenchymal stem cells could be detected by a 1.5-T clinical MR, when the average iron loading was about 200pg/cell[107]. The feasibility of visualizing SPIO labeled cells has also been explored after intra-vessel delivery. Baklanov *et al.* identified comparable hypointense signals in the infarct zone after intracoronary infusion of mononuclear bone marrow cells (BMCs) labeled by Feridex[139]. However, it seems that MRI is unable to detect cells labeled by iron oxide particles, when they are administrated intravenously[140]. Efforts have been made to increase the specificity of MRI cell tracking with iron oxide particles against heterogeneous tissue background. The group of Fayad proposed an appealing MR sequence, named 'Gradient echo Acquisition for Superparamagnetic particles with Positive contrast' (GRASP), which creates positive rather than negative contrast of SPIO[141]. This method may overcome the interference of other sources of T2* effects. The hyperintense signal may increase the specificity of cell tracking. Alternatively, positive contrast of SPIO could be generated by applying spectral selective radiofrequency pulses to excite and refocus the off-resonance water surrounding the labeled cells[142].

Superior to iron oxide labeling, ^{19}F-MRI is highly specific to detect PFC labeled cells due to a lack of detectable ^{19}F signal background in living tissue. But generally it has a lower sensitivity in detecting a small amount of labeled cells, compared to iron oxide nanoparticle labeling detected by ^{1}H-T2*WI. Theoretically, a minimum of 10^{18} ^{19}F atoms in each voxel is needed to reach sufficient signal to noise ratio on ^{19}F-MRI. However, this number seems possible to be reduced by the integrated benefits of high magnetic field, efficient coils and extensive image averaging. Partlow *et al.* demonstrated that 2000 and 6100 cells could be detected by MRS and MRI at 11.7T, respectively, when intracellular loading of ^{19}F atoms was 6×10^{12} /cell[117]. Moreover, the increased intracellular loadings of PFC could be achieved by addition of transfection agents. In comparison to *in vitro* incubation with PFC alone, Ahrens *et al.* observed 26 folds increase of intracellular PFC loading with addition of a transfection agent lipofectamine[94]. With such higher intracellular loading of PFC, significantly smaller amount of labeled cells could be detected by ^{19}F-MRI.

2.3.2 MR imaging of Pathophysiological Processes with Targeted Contrast agents

The past two decades have witnessed tremendous progress in targeting MR contrast agents, which aim at highly specific and sensitive visualization of critical pathophysiological courses. Some of them also have therapeutic functions. Almost all categories of MR tracers/contrast agents (T1, T2/T2* and X-Nucleus *etc.*) have been used to link targeting/functional molecules for such goals. These targeting molecules have a larger share in monoclonal antibodies and peptides. In cardiovascular diseases, inflammation (oxidative enzyme myeloperoxidase-targeted)[143], thrombosis (fibrin-targeted)[144, 145], apoptosis (phosphatidylserine-targeted)[146], fibrosis/scarring[147], vascular remodeling (oxidative enzyme myeloperoxidase-targeted)[148] and angiogenesis (CD13-targeted)[149] *etc*. important pathophysiological processes have been visualized by specific MR tracers/contrast agents. They involved atherosclerosis, ischemic injury, post infarction remodeling, heart failure and transplant rejection *etc*. models of diseases.

2.3.3 Manganese Enhanced Cardiac MRI

Calcium ions are regarded as the most important among the ions involved in the excitation-contraction coupling, a process from electrical excitation of the cardiomyocyte to contraction of the heart. Calcium ions in cardiomyocyte are in a dynamic yet delicate balance, created by multiple interacting cellular systems that can be tuned by physiological modulators. During ischemia and after ischemia-reperfusion, this balance is disturbed. Mishandling of calcium ions in cardiomyocyte is a central cause of contractile dysfunction in ischemic and non-ischemic remote myocardium[3, 14, 15, 150]. In spite of the importance of *in vivo* relevance, our knowledge of cardiomyocyte calcium signaling is mostly from *in vitro* experimental setups, due to the difficulty of doing so *in vivo*.

By using contrast agents based on manganese ions (Mn^{2+}), CMR can detect the activity of calcium channels in cardiac myocytes *in vivo*. Mn^{2+} is a competitive inhibitor of Ca^{2+} influx. Extracellular free Mn^{2+} enters cardiac myocytes predominantly via the L-type channel on cellular membrane. It is also similarly regulated by agents that influence Ca^{2+} influx[151]. Once inside cardiac myocytes, manganese ions can be retained intracellularly at least for several hours. They are predominantly taken up by mitochondria[152]. The rest are believed to bind to macromolecules inside cells. The intracellular Mn^{2+} shortens T1 and induce enhancement on T1WI. Fully quantitative examination of Mn^{2+} uptake in myocardium has also been demonstrated by applying R1 mapping on the heart[153]. Unfortunately, Mn^{2+} enhanced CMR has limited application in clinics, mainly due to the concern of its toxicity to the heart and neurological system. Nevertheless, this approach gives us a means to investigate calcium handling in cardiac myocytes *in vivo* by MRI. The visualizations of myocardial stunning[154], myocardial infarction[155, 156] and alteration of inotropy[157] *etc*. have been demonstrated by manganese enhanced MRI. In recent years, there has been growing interests in developing and applying R1 mapping on manganese enhanced cardiac MRI, aiming at obtaining insights of quantitative calcium signaling *in vivo*. Waghorn *et al.* were the first to apply this technique to investigate alterations in calcium homeostasis in myocardial infarct mouse model[153]. Further, they used the same method to assess calcium efflux of myocardium in mice[158].

In order to interpret manganese enhanced MR image and R1 mapping as a surrogate of calcium handling in cardiac myocytes, many fundamental questions need to be answered. For example, how R1 change in myocardium is related to infusion dose and infusion rate? Is the kinetics of manganese agents related to heart function, which in turn affect R1 enhancement in myocardium?

2.4 Aims of the Thesis

This thesis was aiming to explore the potential of cardiac MRI in investigating ischemia-reperfusion injury and MI healing in molecular and cellular level *in vivo* and non-invasively in small animal models.

Dominated by innate immune responses, infarcted myocardium undergoes dramatic changes in tissue structure and composition during acute and sub-acute phases. Ideally, the healing process constructs a compact scar to sustain the heart function. In recent years, increasing amount of data from both animal models and patients suggested the critical role of blood monocytes in MI healing[32, 33, 159]. It is known that the tissue of reperfused MI is often highly heterogeneous, due to numerous factors (*e.g.* susceptibility to ischemia, ischemia-reperfusion injuries, inflammatory responses). There is still a lack of the knowledge concerning the spatial distribution of monocyte recruitment in heterogeneous tissue of reperfused

MI, in addition to its association to various indicators of poor clinical outcomes, for example MVO and IMH. In this thesis, Chapter 3 describes the successful application of fluorine-19 MRI cell tracking in unambiguous visualization of the spatiotemporal distribution of monocytes and their descendant macrophages in reperfused MI with microvascular obstruction and intramyocardial hemorrhage. Besides the patterns of monocyte infiltration, long-term functional outcomes were monitored by MRI and correlated to the collagen deposition in both infarcted and non-infarcted myocardium. Additionally, ^{19}F cellular MRI was applied to monitor the therapeutic effects of atorvastatin against ischemia-reperfusion injury *in vivo*, in combination to MI tissue characterization by ^{1}H-MRI.

During the healing process of MI, remodeling also takes place in structure and function of non-infarcted myocardium. As one of the most important ions in the ion signal system of the heart, calcium signaling has been found altered in acute and chronic MI hearts. Due to technical challenges, calcium signaling of cardiomyocyte is primarily studied in single cardiomyocyte setting *in vitro*, which poses difficulty in tissue preparation and sometimes relevance to *in vivo* pathophysiology. We improved and applied a quantitative manganese enhanced MRI (MEMRI) method in both sub-acute and chronic MI rats, to probe the influx and efflux of calcium in infarcted and non-infarcted myocardium *in vivo*. In addition, fundamental questions concerning the relationship between the manganese ion infusion rate, its cumulative dose and the enhancement of the spin-lattice relaxation rate constants in blood, myocardium and other tissues were addressed.

The findings of the above experiments provide multifaceted views of the healing process in infarcted hearts, which could be valuable for improving the understanding of mechanisms that determine optimal outcomes of acute MI.

Chapter 3

Inflammation of Healing Myocardial Infarction Monitored by Cellular Fluorine-19 Magnetic Resonance Imaging

3.1 Introduction

The healing of myocardial infarction (MI) is a delicately orchestrated inflammatory process, in which monocytes are central effectors and regulators[27]. Recent studies from both animals and patients revealed that two subsets of monocytes, the inflammatory and reparative monocytes, of distinct but complementary function were recruited sequentially into MI zone and significantly influenced long-term outcomes[32, 33, 159]. Therefore, monocytes are thought to hold a promise as a diagnostic marker and treatment target in individualized therapy to achieve optimal MI healing and reduce the risk of heart failure[27].

However, the spatiotemporal distribution of monocytes in reperfused MI has not yet been well described[32, 33, 159]. The tissue of reperfused MI is known being heterogeneous; therefore, the repair of myocardium with varied severity of ischemia-reperfusion injuries might involve different patterns of monocyte infiltration. In particular, microvascular obstruction (MVO) and intramyocardial hemorrhage (IMH) are distinct features of reperfused MI. They occur in a sizable number of acute MI patients after reperfusion therapy and are markers of severe ischemia-reperfusion injury. Both associating with large MI size and prolonged ischemia before reperfusion, they were found highly correlated[20, 111, 160, 161] and have been proven to strongly indicate worse prognosis[23, 70-72, 162]. Because microvascular damage lags behind cardiomyocyte death, MVO and IMH are always confined in necrosis[69]. However, the distinction between IMH across a spectrum of MVO is not yet elucidated, neither have the clear mechanisms that underlie their important prognostic values been well understood.

In vivo imaging of monocyte recruitment could help to gain deeper knowledge of the inflammatory process of reperfused MI healing, estimate outcomes and guide individualized therapy. Magnetic resonance imaging has superior spatial resolution and versatile contrast to allow for tissue characterization. It is an ideal imaging modality to detect MVO and IMH. In addition, it has been demonstrated that MRI was capable of monitoring cell migration in experimental models *in vivo* and non-invasively[163]. Recently, fluorine-19 MRI for cell tracking has attracted much interest, due to its unambiguous detection and quantitative nature[94]. It overcomes several limitations of iron oxide nanoparticle labeling, avoiding for instance the non-specific magnetic susceptibility effect in tissue background *e.g.* hemorrhage and has potential for future clinical use[163]. In the heart, Flogel *et al.* demonstrated that ^{19}F-MRI could image inflammatory cells infiltrating occluded MI zones in mice[121]. We established the combined ^{19}F cellular MRI and ^{1}H-MRI to visualize the dynamic recruitment of monocytes to reperfused MI with IMH and MVO, which provides a unique window to observe the cellular innate immunity in response to ischemia-reperfusion injuries.

In this study, the spatiotemporal recruitment of monocytes in reperfused MI tissue was unambiguously and non-invasively visualized by *in vivo* ^{19}F-MRI cell tracking in rats. MI areas and the presence of IMH and MVO were characterized by ^{1}H-MRI. The integration of these two observations allowed for investigations of the monocyte infiltration in various regions of reperfused MI during healing. The functional and morphological outcomes under conditions of MVO and IMH were also investigated. In addition, $^{19}F/^{1}H$-MRI was applied to monitor the therapy of reperfused MI by atorvastatin, a medication with primary function of lipid lowering but recently found beneficially limiting MI size and improving outcomes, when given acutely at high dose.

3.2 Methods and Materials

^{19}F-PFC emulsion formulation and its systematic kinetics

Adapted from a previously described protocol[121], the PFC emulsion of 20% v./v. concentration was formulated by emulsifying perfluoro-15-crown-5 ether (CE) (Exfluor Research Corp., Round Rock, TX, U.S.A.) in 3% 3-sn-phosphatidylcholine (Sigma-Aldrich, GmbH, Seelze, Germany) dispersed in phosphate-buffered saline (PBS). The emulsion was further homogenized by SLM Aminco French press with SA-073 minicell at 20,000 psi. (SLM Instrument, Rochester, U.S.A.). The lipid coatings of emulsion particles were stained by fluorescent dye Vybrant® DiD cell-labeling solution (Invitrogen, Damstadt, Germany). The particle size was measured by dynamic light scattering (DLS) (Particle Analyzer FPAR-1000, Otsuka Electronics Co., Japan) and expressed as a mean of 5 measurements ± standard deviation (SD).

The mean life time (t-mean) of PFC emulsion in circulating blood was determined by measuring residual CE contents in blood samples with nuclear magnetic resonance spectrometer (Bruker Avance 400, Bruker BioSpin, Rheinstetten, Germany) at 376.5 MHz. Samples of 100µL blood were taken from 3 female Wistar rats (250g, Charles River, Germany) via tail vein at 1, 2, 3.5, 5, 7, 9.5, 12, 26, 48 and 72 hours after *i.v.* injection of 650µl PFC emulsion/100g body weight. Trifluoroacetic acid (TFA) (Sigma-Aldrich GmbH, Seelze, Germany) served as a reference in ^{19}F-NMR measurements. The t-mean of the PFC emulsion in circulating blood was derived by fitting the exponential equation:

$$S(t) = Ae^{-\frac{t}{t-mean}} \qquad (1)$$

to the measured ^{19}F signal in blood (S(t)) and was expressed as a mean of 3 measurements ± SD.

Quantification of intracellular loading of ^{19}F spins

The pilot studies of flow cytometry on blood samples showed that PFC emulsion primarily labeled CD11b^{+} cells in circulating blood (mainly monocytes and neutrophils). Therefore, we quantified the intracellular loading of ^{19}F spins in

$CD11b^+$ cells by NMR spectrometer on leukocytes separated from full blood of 3 rats (female, Wistar, 250±30g, Charles River, Germany), 2 days after *i.v.* injection of PFC emulsion (650µl/100g body weight). Trifluoroacetic acid (TFA) (Sigma-Aldrich GmbH, Seelze, Germany) served as a reference in ^{19}F-NMR measurements. The total number of the pooled leukocytes was calculated by counting the leukocytes in 20µl sample volume with a hemocytometer. The number of $CD11b^+$ cells was determined by the proportion of $CD11b^+$ cells with flow cytometry. The mean intracellular loading of ^{19}F spins in $CD11b^+$ cells was calculated by averaging the absolute number of ^{19}F spins in the sample by the absolute number of $CD11b^+$ cells.

Reperfused MI model

In accordance with the guidelines for research animal care of our institute and approved by the local ethic committee, reperfused MI was induced in 24 rats (Wistar, female, 200±30g, Charles River, Germany) by ligation of the left anterior coronary artery for 120min and subsequent removal of the knot, via anterior sternotomy under isoflurane (Abbott GmbH, Wiesbaden, Germany) anesthesia. Three sham-operated rats underwent the same procedure, except for arterial occlusion.

Flow Cytometry

On Day 3, 7 and 14 after MI, 400µl fresh peripheral blood from 6 MI rats was taken for flow cytometric analyses. To analyze which cell populations were preferably labeled by PFC emulsion (tagged by DiD), the following monoclonal mouse anti-rat antibodies (mAbs) were used: anti-CD11b RPE (mainly labeling monocyte, neutrophil, macrophage and dentritic cells) (AbD Serotec, Oxford, UK), anti-CD3 FITC (labeling T lymphocytes) (BD Pharmingen, San Diego, CA) and anti-CD45RA FITC (OX-33, only labeling B lymphocytes) (BD Pharmingen). Briefly, single-color staining was done in 50µl PBS/0.1% bovine serum albumin (BSA)/0.02% NaN_3. Cells were incubated with the mAbs for 15 minutes at 4°C, washed twice in 200µl PBS/0.1% BSA/0.02% NaN_3 and finally subjected to erythrolysis in 100µl PBS/0.1% BSA/0.25% saponine for 15 seconds. Following a final wash with 200µl PBS/0.1% BSA/0.02% NaN_3, the cells were subjected to analysis. Data were acquired by a LSRII flow cytometer (BD

Biosciences) using the FACSDiva Software (BD Biosciences). The software FlowJo (TreeStar Inc) was used to further analyze the acquired data.

In vivo ^{19}F/^{1}H-MRI monocyte and macrophage tracking

PFC emulsion was injected via tail vein on Day 1 after operation at a dose of 650µL/100g body weight in 16 of the 24 MI rats. *In vivo* ^{19}F/^{1}H-MRI was performed longitudinally on Days 3, 7 and 14 at a 7-Tesla small animal scanner (Bruker BioSpin GmbH, Rheinstetten, Germany) using a double resonant birdcage coil (Bruker BioSpin GmbH).

For ^{19}F-MRI, turbo spin echo (TSE) MR sequence was applied with TR 750ms, TE 6.4ms, Turbo factor 2, number of averages 16 and spatial resolution (SR) 1×1×2mm. The image acquisition time was 20-30min, depending on the cardiac and respiratory frequencies. For ^{1}H-MRI, MVO was identified by early (1-10min) and late Gd-DTPA (0.3mmol/kg) enhancement (after 10min) using segmented inversion recovery fast low angle shot (FLASH) sequence (TR 1000ms, TE 1.69ms, inversion time 450ms, in-plane resolution 0.312×0.312mm and slice thickness 1mm); IMH regions were detected by ^{1}H-T2*WI with multi-echo Gradient Echo (GE) sequence (TR 150ms, TE ~3/6/9/12ms, in-plane resolution 0.156×0.156mm or 0.156×0.312mm, and slice thickness 1mm); MI regions were determined by late Gd-DTPA enhancement using the same MR sequence and parameters as that for MVO; regional and global contractile functions were appreciated on multi-slice Cine MRI (12 or 24 frames per RR interval, flip angle 30°, in-plane resolution 0.312×0.312mm and slice thickness 1mm). Normalized by an external PFC reference, the ^{19}F signal intensities in MI zone on Days 3, 7 and 14 were compared. In addition, the normalized ^{19}F signal intensity in MVO region was compared to that in MI area with IMH but absent of MVO on Day 14.

Morphological and functional outcomes of MI with MVO and IMH

In order to examine if MI hearts with MVO would have differential long-term outcomes, in comparison to those involving IMH but absent of MVO, MI rats under these two conditions (MI involving MVO: n=3; MI with IMH but absent of MVO: n=5) were followed by ^{1}H-MRI on Days 3 and 28 post-MI. The initial MI size was assessed by late Gd-DTPA enhancement on Day 3. Heart function was determined by multi-slice Cine covering the entire LV. LV end diastolic volume (LVEDV), LV end systolic volume (LVESV), stroke volume (SV), ejection fraction (EF), cardiac output (CO) and cardiac mass (CM) were derived from Cine MRI acquired on Day 3 and Day 28 post-MI. The recovery of heart function was examined by the change of those parameters over time (Day 3 to Day 28). Hearts were excised for histology and immunohistochemistry after MRI on Day 28.

Monitoring therapy of atorvastatin on acute reperfused MI with combined ^{19}F/^{1}H-MRI

Additional 5 MI rats were treated with atorvastatin (I.G., 100mg/Kg) 24h and 1h before MI operation. MI operation procedures were the same as previously described. The *in vivo* and *ex vivo* ^{19}F/^{1}H-MRI protocol was identical to the monocyte tracking experiments. IMH served as a marker of severe microvascular injury of ischemia-reperfusion. The signal intensity of ^{19}F-MRI was a surrogate of the intensity of inflammation.

Ex vivo ^{19}F/^{1}H-MRI

After the last *in vivo* MRI, hearts were excised and underwent *ex vivo* ^{19}F/^{1}H-MRI before freezing (-80°C) or formalin (4%) fixation. For ^{19}F-MRI, TSE sequence was applied with the following MR parameters: TR 4000ms, TE 5.4ms, Turbo factor 20, number of averages 13, and SR 0.375×0.375×0.5mm or 0.375×0.375×1mm. For better visualization of the anatomy and IMH severity, ^{1}H-T2WI was acquired by ^{1}H-TSE sequence with the following MR parameters: TR 2500ms, TE 18ms, Turbo factor 4, in-plane resolution 0.117×0.117mm, and slice thickness 1mm and 0.5mm.

MRI data post-processing

MR image post-processing was performed by using MATLAB (The MathWorks Inc., Natick, USA) and Paravision 4.0 (Bruker BioSpin GmbH, Rheinstetten, Germany).

Histological examination

Sections of myocardium underwent hematoxylin and eosin (H&E) staining for determination of myocardial destruction and inflammatory cell infiltration. By a three-step staining procedure in combination with biotinylated secondary antibody anti-mouse IgG (Vector Laboratories, Inc., Burlingame, CA, USA), immunohistochemical staining with mouse anti-rat ED1 monoclonal antibody (AbD Serotec) was applied on cryo-sections to detect monocytes and macrophages in MI zone. ED1 mAbs specifically recognize the antigen that is expressed predominantly on the lysosomal membrane of monocytes and macrophages in rats. The brown color was developed by the 3,3'-Diaminobenzidine (DAB) substrate KIT for peroxidase (Vector Laboratories), after ED1 monoclonal antibody binding. The nuclei were counter-stained with haemalaun. The same treatments were performed on Paraffin fixed heart tissue to detect monocytes and macrophages in MI zone, in addition to antigen retrieval by heat before antibody incubation. For quantification of monocytes and macrophages in MI area, the antigen was visualized by FITC via avidin and streptavidin conjugates. With ImageJ (NIH, U.S.A.), the density of monocyte/macrophage infiltration was calculated and expressed as the relative area of FITC signal on 3-6 fluorescent pictures/tissue slide of immunohistochemistry (IHC) staining at 200 folds magnification. Intramyocardial hemorrhage was identified by Perl’s Prussian blue (PB) staining to detect the presence of excessive iron contents. PB was performed on tissue section of 30µm thickness; all other histology and immunohistochemistry were done on tissue sections of 8µm thickness.

For the 28 days follow-up hearts, H&E, Picrosirius Red (PSR) and ED1 IHC were performed on cryo-sections to examine tissue destruction, collagen formation and distribution of macrophages, respectively. Quantification of collagen deposition was performed on PSR staining with bright field microscopy. The Red, Green and Blue (RGB) stack and thresholding functions of ImageJ were applied to segment the red-stained regions (collagen fibers on PSR staining) on microscopic photos. In both infarcted (replacement fibrosis) and non-infarcted (interstitial fibrosis) segments, the collagen volume fraction was expressed as the red-stained region divided by the area of myocardial tissue on the photo in percentage. The collagen fiber hue in MI zones was analyzed on photos of PSR staining illuminated by circularly polarized light, according to the method described by Rich and Whittakar[164]. As the collagen fiber thickness increases, the color of fibers evolves from green to yellow, orange and red. The proportion of the four colored fibers were calculated based on the following hue definitions: red 2-9 and 230-256, orange 10-38, yellow 39-51 and green 52-128.

Confocal microscopy

Confocal microscopy was applied to examine the distribution of PFC emulsion in MI zone, 14 days post-MI. After fixation with acetone and blockage with PBS containing 10% horse serum, cryo-sections of MI hearts (20μm) were incubated with the mouse anti-rat ED1 monoclonal antibody (AbD Serotec) overnight at 4°C. Then a biotinylated secondary antibody was added for 1 hour incubation, before incubating with streptavidin FITC and staining the nuclei with DAPI. Control sections were processed identically, with the exception of omitting the incubation with the primary antibody. After ED1 immunohistochemical staining, cryo-sections of myocardium underwent serial scans with a thickness of 0.5μm, by a Leica TCS SP5 confocal laser-scanning microscope (Leica Microsystems, Mannheim, Germany). A 40× HCX PL Apo objective was applied. Monocytes and macrophages were identified by the green fluorescent FITC (intracellular) and the PFC emulsion was tagged by the near infrared fluorescent DiD.

Detection sensitivity and quantification of ^{19}F-MRI

To determine the detection limit of ^{19}F-MRI and the correlation between the concentration of ^{19}F atoms and its ^{19}F signal to noise ratio (SNR), a phantom study was performed on Eppendorf tubes containing the following concentrations of PFC emulsion suspended in 1.5% agarose: 0.35, 0.7, 1.4, 2.1, 2.8, 3.5, 7.0 and 10.4 ($\times 10^{16}$) ^{19}F atoms / voxel. Parameters of ^{19}F- and ^{1}H-MRI were identical to those of *in vivo* MRI, except for the higher spatial resolution of $0.11\times0.11\times1$mm, in order to reduce the number of ^{19}F atoms/voxel. The SNR of each concentration was calculated and expressed as mean±SD of 6 MRI scans. The concentration of ^{19}F atoms versus its SNR value was plotted and the Pearson correlation coefficient was derived from the linear fit. $\text{SNR}\geqslant 3$ was considered as detectable. The limit of detection on PFC labeled blood monocytes was determined by converting the minimal detectable number of ^{19}F atoms to the equivalent number of PFC labeled blood monocytes 2 days after *i.v.* injection of PFC emulsion.

^{19}F signal impairment by susceptibility effects

When in proximity to PFC, degraded hemoglobin contents may shorten ^{19}F-T2 and attenuate ^{19}F signal intensity on T2-weighted ^{19}F-TSE images. To quantitatively study the influence of magnetic susceptibility effects on ^{19}F-T2 and the signal intensity on ^{19}F-T2WI, we created a scenario in which iron oxide micro-particles and PFC emulsion coincided within the same Kupffer cells in liver. Micrometer-sized iron particles (MPIOs, 4mg Fe/kg) (Bangs Laboratories, Inc.) were injected *i.v.* in 3 rats (Wistar, female, 250±25g, Charles River, Germany), which have previously received *i.v.* injections of 650µl PFC emulson/100g body weight. MPIOs are known to induce strong susceptibility effects and allow for single particle detection with ^{1}H-T2*WI MRI[165]. ^{19}F-T2WI (TSE) and ^{1}H-T2*WI were acquired *in vivo* on the same image plane of the liver in the same animal before and after MPIO injection. After *in vivo* MRI, livers were excised and fixed in 4% paraformaldehyde for quantification of the influence of local magnetic susceptibility on ^{19}F-T2, compared to another 3 livers from rats with only PFC emulsion injection (0.65ml/100g body weight) but not MPIO. For ^{19}F-T2 maps, we applied multiple spin echo (MSE) sequence with TR 2100ms, TE 5ms and 150 echo images.

The T2* effects of MPIO in liver and that of IMH in MI were compared by their reduction on SNR in the homing tissue. In liver, the decrease of SNR was determined by $(SNR_{post} - SNR_{pre}) / SNR_{pre}$, where SNR_{pre} and SNR_{post} stand for the SNRs in liver before and after MPIO injection on 1H-T2*WI (TE 6ms), respectively. In MI hearts (n=6), the decrease of SNR was determined by $(SNR_{IMH} - SNR_{remote}) / SNR_{remote}$, where SNR_{IMH} and SNR_{remote} stand for the SNRs in IMH area and remote non-infarcted myocardium (septum) on ^{1}H-T2*WI (TE 6ms), respectively. Normalized by the ^{19}F signal intensity of an external PFC reference, the ^{19}F signal intensities in liver before and after MPIO injection were compared.

Statistics

Results were expressed as mean±SD. Student t-test or repeated measures ANOVA was applied to examine the significance of difference in variables, when appropriate. $P<0.05$ was considered significantly different in statistics.

3.3 Results

PFC emulsion, its kinetics and intracellular loading of ^{19}F

The average diameter of PFC emulsion was 228.1±5.8nm. In circulating blood, the average t-mean of PFC was 12.05±2.15 hours. 48 hours after injection, most PFC was cleared out from circulating blood. 72 hours after injection, no ^{19}F could be detected in blood by NMR spectrometer (Figure 3.1a). Two days after PFC emulsion injection, the mean intracellular loading of ^{19}F spins was 3.8×10^{12} in blood monocytes (Figure 3.1b).

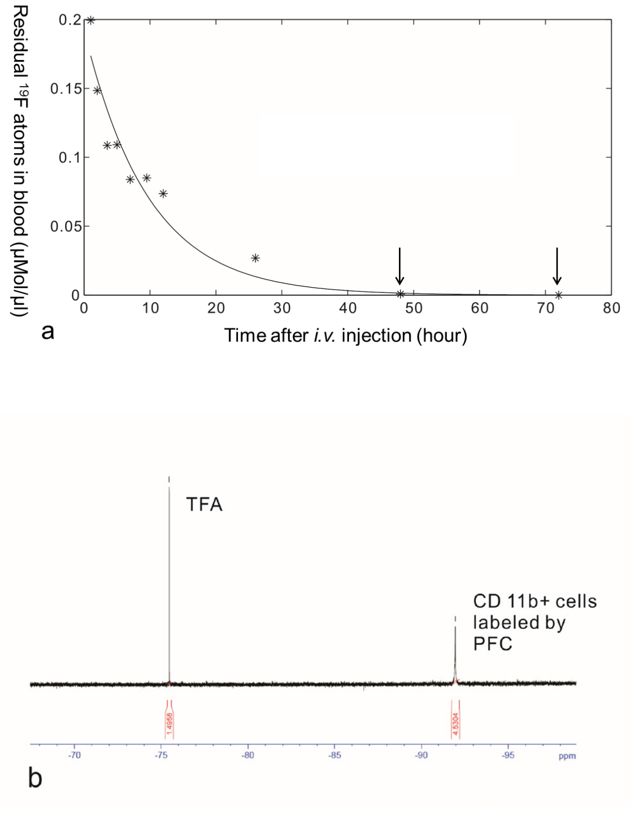

Figure 3.1 *In vivo* kinetics and intracellular loading of PFC emulsion. (a): A representative clearance curve of PFC in circulating blood. Black arrows indicate that PFC was almost cleared out from blood 48 and 72 hours after injection (b): NMR spectroscopy of leukocytes separated from full blood of rats, 2 days after *i.v.* injection of PFC emulsion. The peak at -92ppm was contributed by CD11b$^+$ cells labeled by PFC. The peak at -75.5ppm was the signal from the reference TFA.

Reperfused MI model and sham-operated animals

In the 16 MI rats that were injected with PFC emulsion 1 day after MI, 15 of them developed IMH, among which 5 animals had MVO accompanied by IMH. None of the 3 sham-operated rats had MI. In the 8 MI rats assigned to the 28 days follow-up studies (without PFC emulsion injection), three of them developed MVO accompanied by IMH and the rest 5 of them had IMH absent of MVO.

Flow cytometry

On Day 3, 32±8.1% circulating leukocytes were labeled by PFC emulsion, as indicated by their fluorescent label DiD (Figure 3.2a). In addition, almost all the DiD$^+$ cells were CD11b$^+$ (Figure 3.2b), whereas CD3$^+$ (T cells) and CD45RA$^+$ cells (B cells) were negative for DiD. The proportion of PFC labeled CD11b$^+$ cells in blood remained 100% on Day 7, although the amount of the internalized PFC decreased, as indicated by the shift of DiD fluorescent histogram (Figure 3.2c). On Day 14, no DiD could be detected in CD11b$^+$ cells from blood.

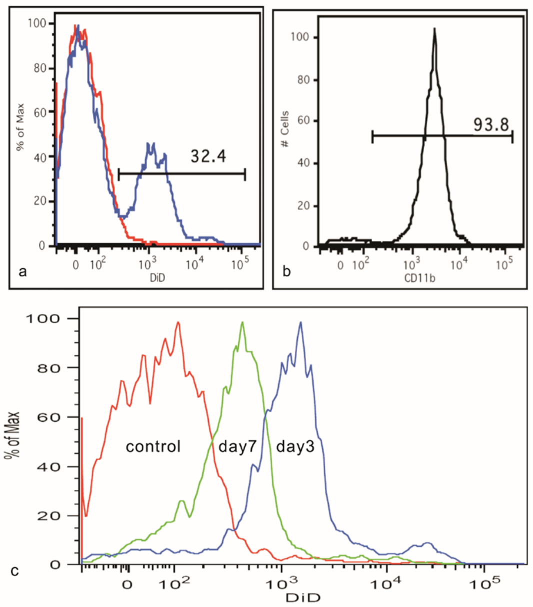

Figure 3.2 Flow cytometry of blood CD11b$^+$ cells labeled by PFC in a representative animal. (a): 3 days after MI, PFC (DiD$^+$) was detected in 32.4% of blood leukocytes. (b): Almost all PFC-labeled leukocytes were CD11b$^+$. (c): When gating on CD11b$^+$ cells, the fluorescent histogram of DiD showed that all CD11b$^+$ cells were labeled by PFC (DiD$^+$) on Day 3 (blue) and Day 7 (green). The control histogram in red represents DiD signal from blood CD11b$^+$ cells of rats without PFC emulsion injection. The shift of DiD fluorescent histogram suggests a decrease of PFC intracellular loading from Day 3 to Day 7.

In vivo ^{19}F/^{1}H-MRI

By overlaying ^{19}F images on corresponding ^{1}H-MR images, the origin of ^{19}F signal could be precisely determined. ^{19}F signal emerged from MI zones but sometimes appeared smaller than the hyperintense areas on late Gd-DTPA enhancement. IMH was always confined in MI zone (Figure 3.3). MVO was found in the core of MI and accompanied by IMH (Figure 3.4).

Importantly, ^{19}F distributed inhomogenously in MI zone. When MVO was absent (Figure 3.3), the intensity of ^{19}F signal appeared in response to the severity of ischemia-reperfusion injury: the more intense ^{19}F signal distributed in MI core with severe IMH, where serious microvascular injury and myocardial necrosis occurred; the less intense ^{19}F signal was found in MI regions without or with less severe IMH as well as in peripheral MI regions. However, ^{19}F signal was attenuated in MVO areas, where severe necrosis was accompanied by IMH. Normalized by the ^{19}F signal of an external PFC reference, the ^{19}F signal was significantly lower in MVO regions than in IMH areas not involving MVO ($p=0.001$) (Figure 3.4).

The spatial distribution of ^{19}F signal in MI zone was similar on Days 3, 7 and 14, with the tendency of shrinkage in volume. Normalized by the ^{19}F signal of an external PFC reference, the signal intensity of ^{19}F was highest on Day 3, and decreased significantly ($p=0.048$) by 24% on Day 7. Day 14 saw a further reduction of 14% in ^{19}F signal intensity, which was significantly lower than that of Day 3 ($p<0.001$) but insignificant to that of Day 7 ($p=0.112$) (Figure 3.3f).

The contrast pattern of IMH could be highly dynamic. In 3 MI rats (19%), signal voids on ^{1}H-T2*WI expanded in area and presented stronger susceptibility effects from Day 3 to Day 7, while the ^{19}F signal decreased but consistently and unambiguously represented the distribution of labeled monocyte and macrophages (Figure 3.5).

No abnormality of contractile function or hyperintensity on Gd-DTPA late enhancement was found in sham-operated hearts, nor was ^{19}F signal.

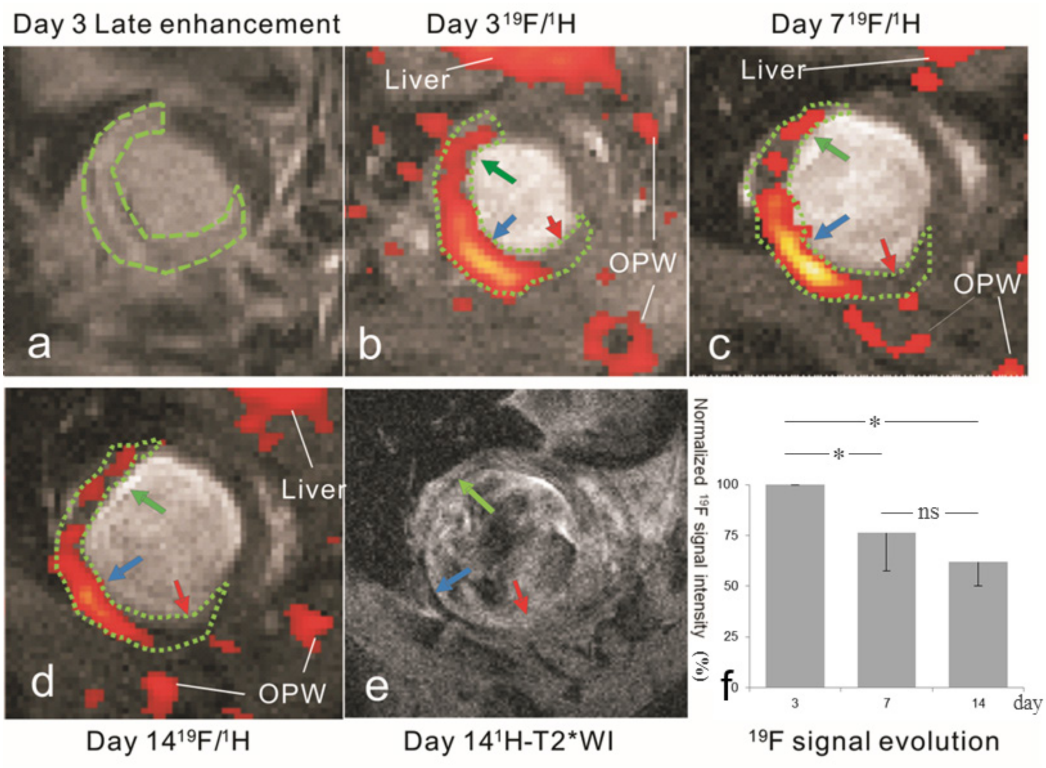

Figure 3.3 Longitudinal observations on the spatiotemporal distribution of ^{19}F signal in reperfused MI with IMH. (a): On Day 3 after MI, Gd-DTPA late enhancement delineated MI in anterior, lateral and inferiorlateral walls (green dash line). (b, c & d): The origins of ^{19}F signal (hot color) were determined by overlaying ^{19}F-MRI on Cine images. From Day 3 to 14, the ^{19}F signal in MI zone distributed similarly, alongside the thinning and elongation of MI segments; but the overall intensity and volume of ^{19}F in MI zone decreased over time. ^{19}F signal was also seen in liver and operation wounds (OPW). (e): IMH appeared as signal voids (blue and green arrows) on ^{1}H-T2*WI. The more intense ^{19}F signal emerged in MI core with severe IMH (blue arrow) and the less intense ^{19}F signal distributed in peripheral MI region with less severe IMH (green arrow). Note that ^{19}F signal was not seen in part of the peripheral MI area without IMH in anterior wall (red arrow). (f): the column charter shows the evolution of the mean ^{19}F signal intensity (normalized by an external PFC reference and adjusted to the baseline value on Day 3) in MI zone with time. (*$p<0.05$, ns: statistically not significant.)

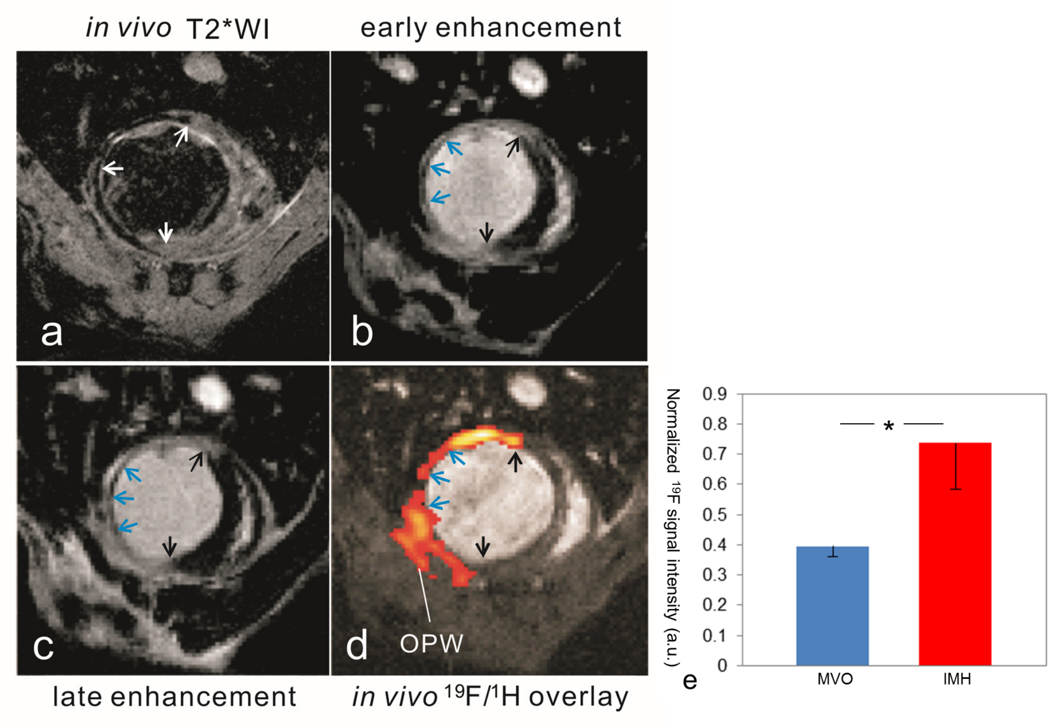

Figure 3.4 *In vivo* ^{19}F/^{1}H-MRI of MI with MVO and IMH. (a): On Day 14 after infarction, a large IMH (white arrows) appeared as signal voids involving anteriorlateral, lateral and inferiorlateral walls on ^{1}H-T2*WI. (b&c): early and late Gd-DTPA enhancement delineated a large infarct (black arrows). MVO (blue arrows) located in the MI core in the lateral wall, presenting a sub-endocardial dark rim surrounded by brightly enhanced necrosis. (d): When superimposed on Cine-MRI, the corresponding ^{19}F image showed that the ^{19}F signal (hot color) intensity in MVO area (blue arrows) was absent or lower than in IMH areas without MVO. (e): Normalized by the signal intensity of an external PFC reference, the ^{19}F signal intensity of MVO regions was significantly lower than that of IMH areas absent of MVO (*$p<0.05$).

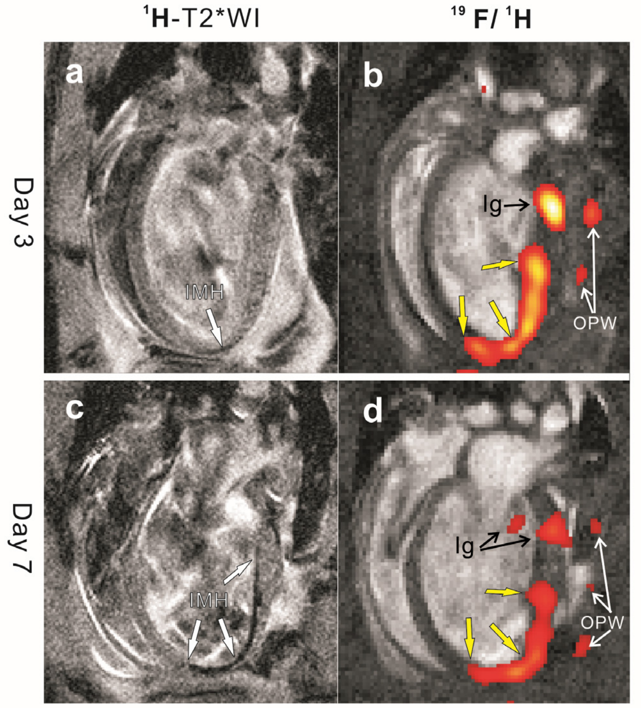

Figure 3.5 The contrast evolution of IMH on ^{1}H-T2*WI with time. (a&c): On long axis views of an infarcted heart on ^{1}H-T2*WI, the signal voids of IMH appeared only at the apex on Day 3 (white arrow), but expanded along endocardium layer from apex to the entire inferior wall on Day 7 (white arrows). (b&d): In contrast, the ^{19}F signal (hot color) attenuated but showed similar spatial distribution in apical and inferior segments (yellow arrows) from Day 3 to Day 7. ^{19}F signal also appeared in ligation sites of MI (lg) and operation wounds (OPW).

Ex vivo ^{19}F/^{1}H-MRI

The distributions of ^{19}F signal and IMH on *ex vivo* MRI correlated well with that on *in vivo* MRI. In hearts without MVO, the most intense ^{19}F signal emerged in the MI core with severe IMH, the median and the least intense ^{19}F signal appeared in MI zone with less severe IMH and in peripheral MI area without IMH, respectively (Figure 3.6, panel-A). Similarly to *in vivo* MRI, *ex vivo* MRI of hearts with MVO showed much attenuated ^{19}F signal in MI regions corresponding to the MVO areas delineated by Gd-DTPA enhancement *in vivo*, but the reduction of ^{19}F signal was more apparent in these regions. In addition, the areas with highly reduced or absent ^{19}F signal appeared larger on MRI with higher spatial resolution (0.5mm slice thickness) (Figure 3.7, panel-A). In sham-operated hearts, neither wall thinning, nor IMH, nor ^{19}F signal were observed on *ex vivo* MRI.

Panel-A

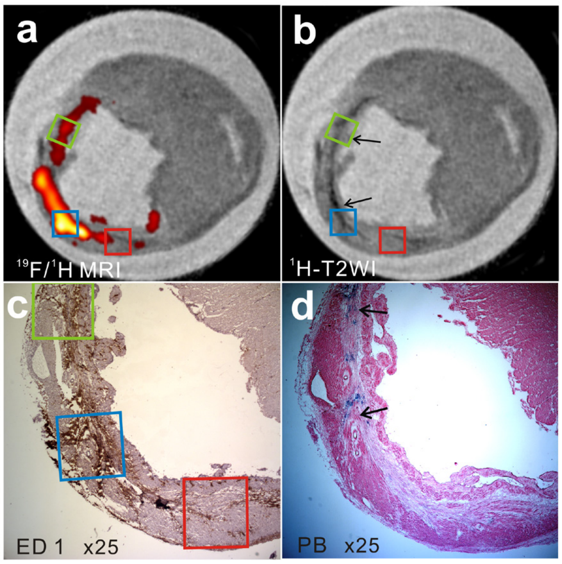

Figure 3.6 *Ex vivo* MRI and histology of MI heart with IMH absent of MVO (the same heart of Figure 3.3). **Panel-A**: Corresponding to the arrows of the same colors on *in vivo* MRI (Figure 3.3), the green, blue and red boxes indicate the peripheral MI area with IMH, the MI core with severe IMH and the peripheral MI region without IMH, respectively. (a&b): The distributions of ^{19}F signal and IMH matched well with *in vivo* MRI (Figure 3.3d&e). (c&d) show the corresponding ED1 immunohistochemistry and PB staining of (a&b). Black arrows indicate the match of excessive iron detected by PB (d) and IMH defined by *ex vivo* ^{1}H-T2WI MRI (b).

Panel-B

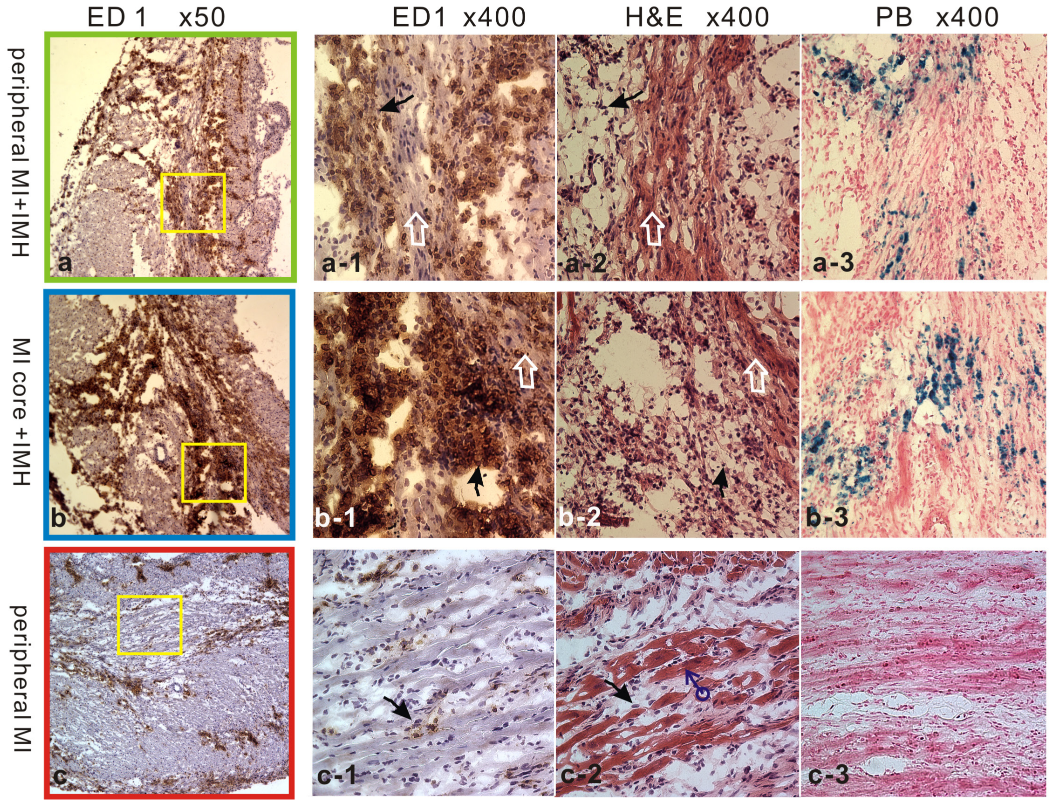

Panel-B: (a, b & c) are ED1 immunohistochemistry from the box regions with the same frame color in Panel A. The yellow boxes indicate the location of the ×400 pictures in the same row (column-1/2/3). The density of macrophages (brown stained cells) on ED1 IHC correlated well with the ^{19}F signal intensity on *ex vivo* ^{19}F/^{1}H-MRI (Panel A-a). PB staining presented the severity of IMH. (b-1): The most abundant monocytes and macrophages were found in MI core with severe IMH (b-3). (a-1): Less abundant monocytes and macrophages were found in peripheral MI area with less severe IMH (a-3). (c-1): Only sparse infiltrates of monocytes and macrophages appeared in peripheral MI region without IMH (c-3). (a-2&b-2): H&E staining shows the necrotic myocardium was mostly replaced by granulation tissue in MI zone with IMH. (c-2): In peripheral MI area without IMH, few inflammatory cells were found in myocardium with interlaced necrosis and viable cardiomyocytes. The *ex vivo* ^{19}F/^{1}H-MRI (Panel A-a) as well as IHC and histology in the red box region (Panel-B c-1&2) revealed that the peripheral MI region without ^{19}F signal on *in vivo* MRI (indicated by the red arrows on Figure 3.3) contained only few scattered monocyte and macrophage that couldn't be detected by ^{19}F-MRI. (black arrows: monocytes and macrophages, white arrows: necrotic myocardium, and blue arrow: viable cardiomyocytes)

Histological examination on hearts 14 days after infarction

In hearts with IMH but absent of MVO 14 days after infarction, the densest monocyte/macrophage infiltration was found in the MI core accompanied by excessive iron contents (from severe IMH) as evidenced by PB staining in the same region on the neighboring tissue slice; the median dense infiltration of monocytes and macrophages was seen in peripheral MI area with less iron on PB staining; and few monocytes and macrophages appeared in peripheral MI region without PB^+ staining. H&E staining of those hearts revealed that infarct necrosis was mostly absorbed and replaced by granulation tissue (Figure 3.6, panel-B).

In hearts with MVO 14 days after infarction, very few monocytes and macrophages were found by ED1 staining in the MVO corresponding region that showed attenuated ^{19}F signal in MI core by *ex vivo* ^{19}F/^{1}H-MRI. This area resembles an “island” lacking monocyte/macrophage infiltration in hemorrhagic MI zones. The “island” contained necrosis with presence of (myo)fibroblasts and was accompanied by abundance of excessive iron contents, as was evident from H&E and PB staining of the neighboring tissue specimens. The approximate border dividing the “island” and the surrounding MI area could be seen on ED1 IHC and H&E staining (Figure 3.7, panel-B).

The above distribution patterns of macrophages and excessive iron contents in histology agreed well with those of the ^{19}F signal intensity on ^{19}F-TSE images and the hypointensity on ^{1}H-T2WI of *ex vivo* MRI, respectively. Destruction of myocardium and infiltrates of inflammatory cells were not observed in sham-operated hearts.

Panel-A

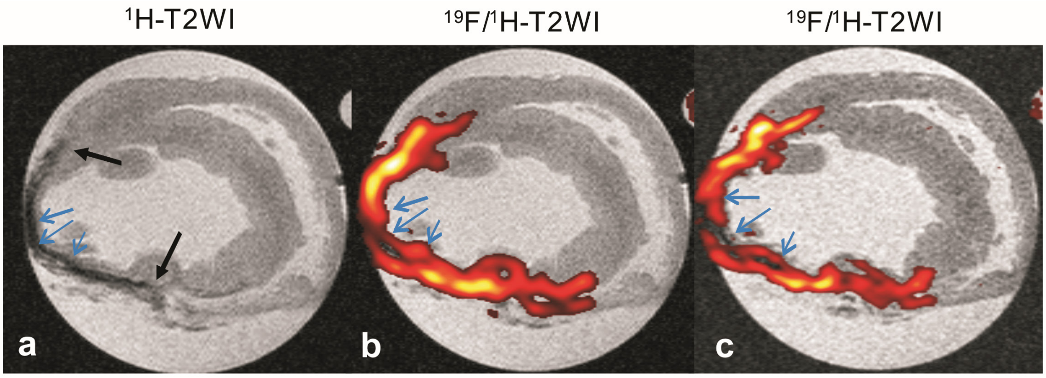

Panel-B

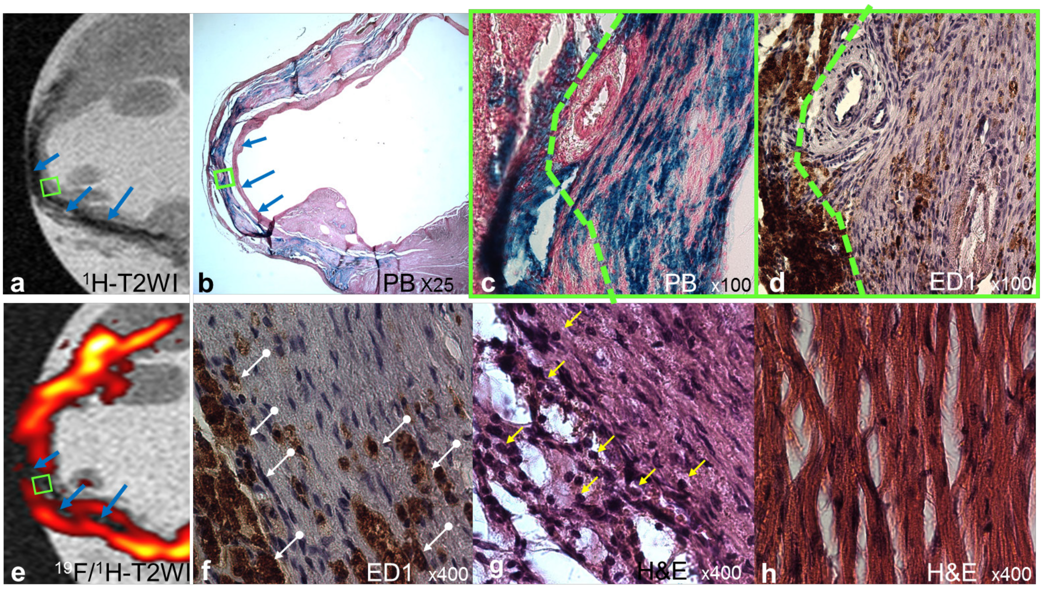

Figure 3.7 *Ex vivo* MRI and histology of MI heart with MVO accompanied by IMH (the same heart of Figure 3.4). **Panel-A** (a&b): *Ex vivo* MRI (slice thickness 1mm) correlates well with *in vivo* MRI on the morphology of IMH (between the black arrows) and the distribution of ^{19}F signal (Figure 3.4 a&d). (b): Very weak or absent ^{19}F signal (blue arrows) appeared in the area corresponding to the MVO region (in IM core) identified by Gd-DPTA enhancement on *in vivo* MRI (Figure 3.4 b&c). (c): With a higher spatial resolution of 0.5mm slice thickness, *ex vivo* MRI revealed that the area with attenuated ^{19}F signal (blue arrows) in the MVO corresponding area was larger than it appeared on the slice with 1mm slice thickness (b).

Panel-B shows the histology and immunohistochemistry of this heart. The green boxes are placed in the MVO corresponding area (blue arrows) detected by *in vivo* MRI. (a&e): cropped and enlarged images of Panel A-a&c. (b): PB staining revealed that the regions with shorter T2 on ^{1}H-T2WI (a) had excessive iron contents. (c&d): The green dash lines indicate the approximate MVO border, where monocytes and macrophages started to infiltrate. In the MVO corresponding region (to the right of the green dash line), severe IMH (blue stained) was accompanied by few monocytes and macrophage (brown). (f) shows the higher magnification view of the approximate infiltration front of monocytes and macrophages (white arrows). (g): In the same region on the neighboring tissue section of (f), H&E staining shows the necrotic myocardium inside MVO area and the leukocytes with large round nuclei (some marked with yellow arrows) on the invasion front. In necrosis, numerous (myo)fibroblasts appeared. They are characterized by the spindle shaped nuclei. (h): In contrast to the necrotic myocardium, the morphology of viable myocardium stained by H&E in remote non-infarcted myocardium is demonstrated.

Confocal Microscopy

On confocal microscopy, DiD-tagged PFC emulsion nanoparticles distributed intracellularly in monocytes and macrophages (ED1$^+$) in MI (Figure 3.8).

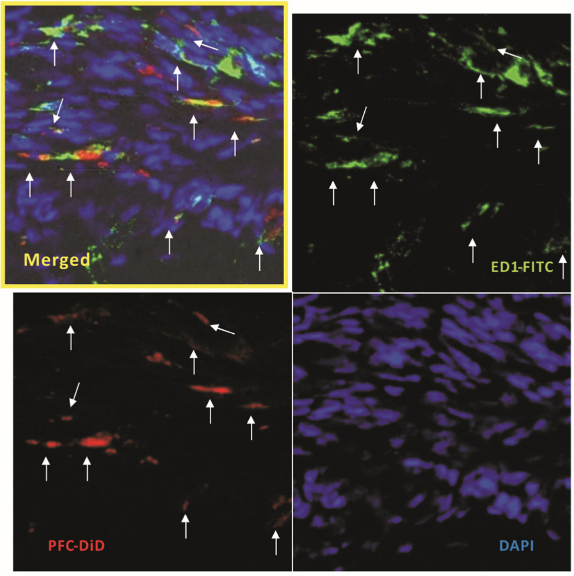

Figure 3.8 Confocal microscopy of infarct tissue with ED1-FITC IHC staining. ED1 recognized a specific antigen that is expressed predominantly on the lysosomal membrane (intracellular) of monocytes and macrophages in rats. PFC emulsion (red, labeled by DiD) distributed in monocytes and macrophages (ED1$^+$, green) in MI zone. DAPI was used to identify the nuclei.

^{19}F signal was not impaired by strong susceptibility effects

No significant reduction of ^{19}F signal intensity has been observed when excessive iron oxide was present in liver Kupffer cells on *in vivo* MRI (p=0.52) (Figure 3.9), even though the susceptibility effect was significantly stronger than that of IMH in MI zone (p=0.004). Because the susceptibility effect depends on the micro-distribution of iron and PFC, ^{19}F-T2 is likely maximally shortened when MPIO and PFC were in the same Kupffer cells. In hemorrhagic infarction only a portion of paramagnetic hemoglobin-degraded products was internalized in monocytes and macrophages containing PFC. The rest stayed farther out (in extracellular space). On *ex vivo* MRI of the liver, ^{19}F-T2 mapping revealed around 60% shortening of ^{19}F-T2 time when MPIO was co-injected. Besides the moderate shortening of ^{19}F-T2, the unaffected ^{19}F signal intensity on ^{19}F-TSE images was probably also a result of the short effective echo time applied during both *in vivo* (effective TE=6.4ms, Turbo factor=2) and *ex vivo* (effective TE=5.4ms, Turbo factor=20) MRI in our experiments. Therefore, the possibility of ^{19}F signal reduction caused by the ^{1}H-T2* effects in IMH areas could be excluded. In agreement with previous studies by other researchers, the ^{19}F phantom experiment showed that the ^{19}F signal intensity on TSE MRI was linearly correlated to the ^{19}F spin concentration[121, 124, 166]. Accordingly, the ^{19}F signal intensity allows for approximate comparison of the infiltration density of labeled monocytes and macrophages, independent of tissue background.

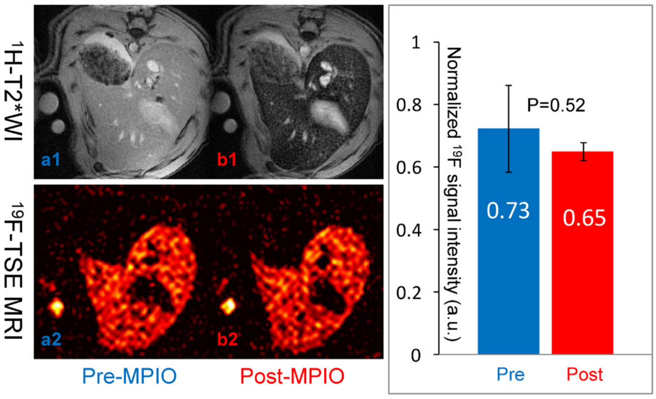

Figure 3.9 ^{19}F signal intensity on ^{19}F-TSE image was not affected by strong local susceptibility effects. (a1): ^{1}H-T2*WI of the liver before MPIO injection. (a2): ^{19}F-TSE image of the liver before MPIO injection. (b1): ^{1}H-T2*WI of the liver, 1 hour after MPIO injection. There was dramatic signal loss in the liver. (b2): ^{19}F-TSE image of the liver, 1 hour after MPIO injection. The ^{19}F signal intensity in liver was similar to that before MPIO injection. The column chart shows the mean±SD of the normalized ^{19}F signal intensity in liver before (blue) and after (red) MPIO injection.

Detection sensitivity and quantification of ^{19}F-MRI

The minimal detectable concentration of ^{19}F atoms was 1.4-2.1×10^{16} ^{19}F atoms/voxel, reaching SNR of 2.8-4.3 (Figure 3.10 a&b). This detection limit is equivalent to 3684-5526 labeled blood monocytes (two days after ^{19}F-emulsion injection) per voxel. The ^{19}F signal was linearly correlated to the concentration of ^{19}F atoms with the Pearson correlation coefficient of 0.99 (Figure 3.10c).

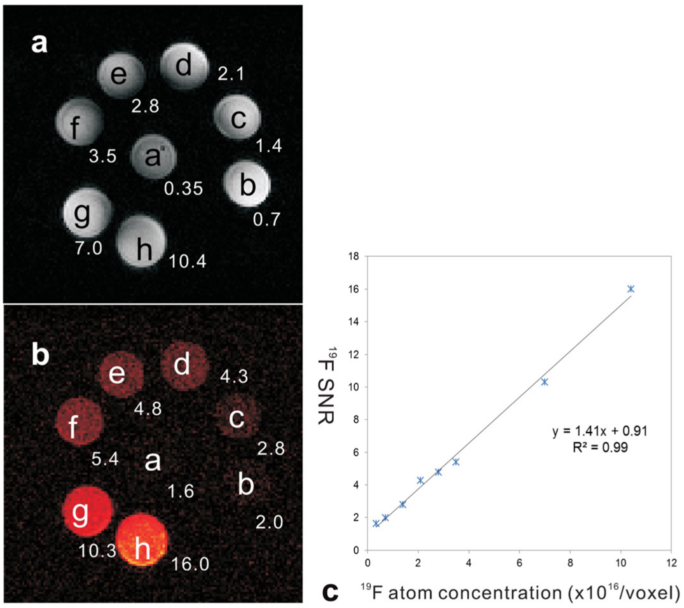

Figure 3.10 Phantom studies determining the detection limit of ^{19}F-MRI and the correlation between the concentration of ^{19}F spins and the ^{19}F SNR. (a): ^{1}H-MRI of a phantom containing Eppendorf tubes filled with different concentrations of PFC emulsion suspended in 1.5% agarose, where a = 0.35, b = 0.7, c = 1.4, d = 2.1, e= 2.8, f = 3.5, g = 7.0 and h = 10.4 (×10^{16}) ^{19}F spins/voxel. (b): color scaled ^{19}F-MRI shows the corresponding signal intensity of the PFC suspensions. Their SNR values are marked alongside. (c): The concentrations of ^{19}F spins versus their mean SNR values are plotted. The values of standard deviation were not shown on the plots because they are smaller than could be visible on the plotting.

MI with MVO and IMH: differential long-term morphological and functional outcomes

The initial MI size was similar in both MVO and IMH groups (MVO vs. IMH = 107.45±60.95µl vs. 85.14±34.84µl, p=0.52), as measured by multi-slice late Gd-DTPA enhancement MRI on Day 3 after MI (Figure 3.11 Panel-A). On the same day, EF, LVEDV, LVESV, CO and LVM *etc*. functional index were similar between the two groups (Table 3.1). 28 days later, The MVO group had lower mean EF (33.3±8.2% vs. 45.5±11.8%, p=0.076) and higher mean LVM (0.68±0.17g vs. 0.53±0.12g, p=0.090) than the IMH group, with borderline p values (Table 3.2). However, the MVO group has significantly worsened pump function conversely to the improved EF of the IMH group, as evidenced by the change of EF (ΔEF) between Day 28 and Day 3 (Figure 3.11 Panel-A, ΔEF_{MVO} vs. ΔEF_{IMH} = -7.2 ±3.7% vs. 4.13±4.6%, p=0.006). In addition, the MVO group demonstrated greater mean values of ΔLVESV ($\Delta LVESV_{MVO}$ vs. $\Delta LVESV_{IMH}$ = 0.216 ±0.215ml vs. 0.059±0.089ml, p=0.093), ΔLVM (ΔLVM_{MVO} vs. ΔLVM_{IMH} = 0.18±0.13g vs. 0.056±0.123g, p=0.109), as well as Δheart rate (Δheart $rate_{MVO}$ vs. Δheart $rate_{IMH}$ = 30±30/min vs. -19±47/min, p=0.082), compared to the IMH group (Table 3.3).

Table 3.1 LV volumes and function on Day 3

Day3	**IMH** (n=3)	**MVO** (n=5)	**p**
EF (%)	41.4±8	40.5±7.7	0.439
LVESV (ml)	0.21±0.07	0.24±0.11	0.311
LVEDV (ml)	0.35±0.08	0.40±0.12	0.27
SV (ml)	0.14±0.02	0.15±0.02	0.178
CO (l/min)	0.056±0.01	0.058±0.01	0.369
LVM (g)	0.48±0.06	0.5±0.05	0.288
Heart Rate (/min)	399±21	380±17	0.109
R-R Period (ms)	150±7.8	158±6.9	0.107

Table 3.2 LV volumes and function 28 days post-MI

Day 28	**IMH** (n=3)	**MVO** (n=5)	**p**
EF (%)	45.5±11.8	33.3±8.2	**0.076**
LVESV (ml)	0.27±0.16	0.46±0.32	0.114
LVEDV (ml)	0.47±0.18	0.66±0.37	0.179
SV (ml)	0.2±0.04	0.2±0.06	0.498
CO (l/min)	0.076±0.017	0.082±0.024	0.345
LVM (g)	0.53±0.12	0.68±0.17	**0.09**
Heart Rate (/min)	380±39	409±17	0.142
R-R Period (ms)	159±18	147±5.8	0.155

Table 3.3 Changes of LV volumes and function 28 days after infarction

Day 28	**IMH** (n=3)	**MVO** (n=5)	**p**
ΔEF (%)	4.13±4.6	-7.2±3.7	**0.006***
ΔLVESV (ml)	0.059±0.089	0.216±0.215	**0.093**
ΔLVEDV (ml)	0.12±0.12	0.26±0.26	0.159
ΔSV (ml)	0.059±0.05	0.046±0.045	0.36
ΔCO (l/min)	0.02±0.021	0.024±0.02	0.403
ΔLVM (g)	0.056±0.123	0.18±0.13	0.109
ΔHeart Rate (/min)	-19±47	30±30	**0.082**
ΔR-R Period (ms)	8.6±21	-11±11	**0.091**

Panel-A

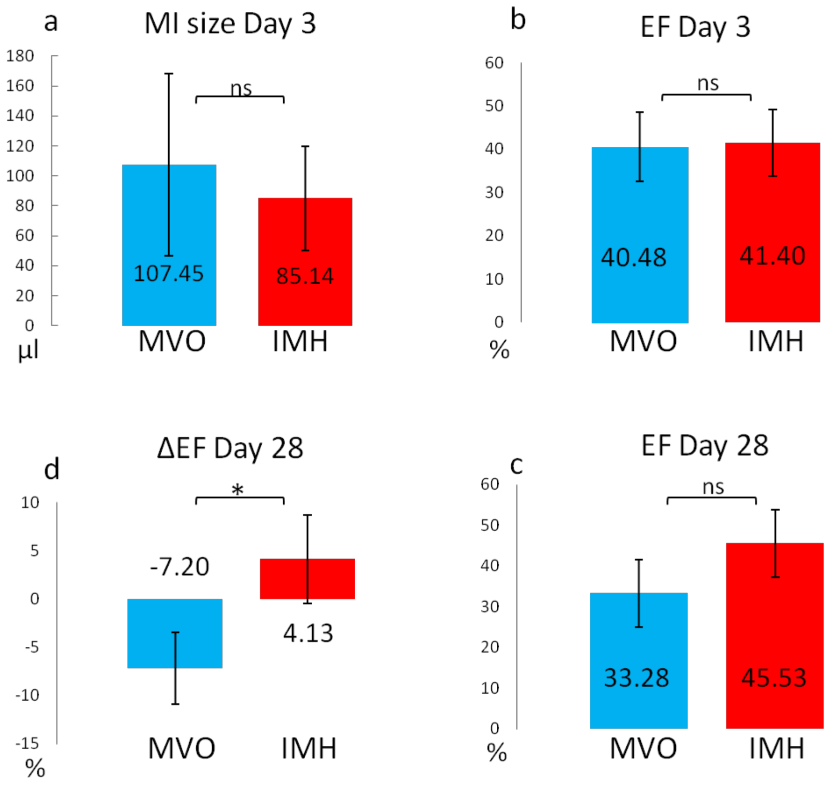

Figure 3.11 Panel-A MI size and functional outcomes of hearts with IMH and MVO. (a): MI size on Day 3. (b): ejection fraction (EF) on Day 3. (c): EF on Day 28. (d): the change of EF (ΔEF) between Day 28 and Day 3. (*p<0.05, ns: statistically not significant.)

Panel-B

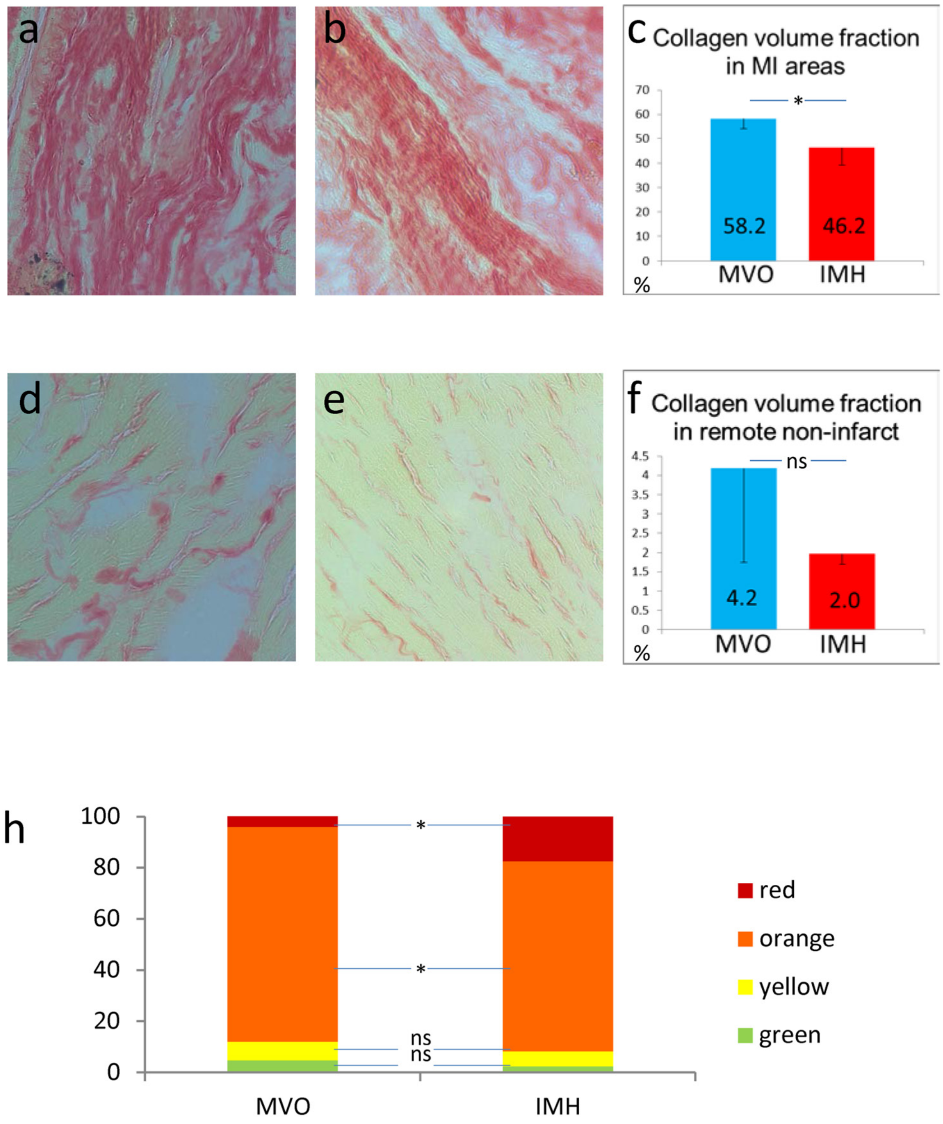

Figure 3.11 Panel-B 28 days after MI, collagen volume fraction and collagen fiber hue analysis of MI hearts with IMH (n=4, one heart tissue was damaged before histological examination) and MVO (n=3). Bright field microscopic photography of picrosirius red (PSR) staining: (a) infarcted region of an MI heart with MVO, (b) infarcted area of an MI heart with IMH but absent of MVO, (d) remote non-infarcted myocardium (septum) of an MI heart with MVO and (e) remote non-infarcted myocardium (septum) of an MI heart with IMH but absent of MVO. Column charts show quantification of collagen volume fraction on bright field microscopy of PSR staining: (c) in infarcted regions and (f) in remote non-infarcted myocardium (septum). (h) Hue analysis of collagen fibers of MI zone in the MVO group and the group with IMH but absent of MVO. (*$p<0.05$, ns: statistically not significant.)

In addition, the collagen contents in both MI zones (replacement fibrosis) and remote non-infarcted myocardium (interstitial fibrosis) were quantitatively examined in the MVO and IMH groups by PSR staining, 28 days after infarction. Derived from the bright field microscopic pictures of PSR staining, the collagen volume fraction in MI segments was significantly higher in the MVO group (MVO vs. IMH = 58.18±3.97% vs. 46.19±6.79%, p=0.043). Further analysis on the collagen fiber hues by circularly polarized light microscopy on PSR staining revealed that the replacement fibrosis of the MVO hearts contained significantly lower proportion of red collagen fibers (the thickest collagen fibers), in comparison to that of the IMH hearts (MVO vs. IMH = 4.10±2.94% vs. 17.48±6.98%, p=0.028). The orange fibers were significantly higher in the MVO group (MVO vs. IMH = 83.86±3.0% vs. 74.27±3.5%, p=0.013). The proportions of the green and yellow collagen fibers (thin fibers) were similar in the two groups (Green fibers: MVO vs. IMH = 4.74±2.99% vs. 2.40±1.94%, p=0.26; yellow fibers: MVO vs. IMH = 7.31±2.98% vs. 5.85±2.89%, p=0.452). The mean value of the collagen volume fraction in remote non-infarcted myocardium (interstitial fibrosis) was greater in the MVO group than in the IMH group, without statistical significance (MVO vs. IMH = 4.18±2.43% vs. 1.97±0.27%, p=0.26). (Figure 3.11 Panel-B)

Monitoring therapy of atorvastatin in experimental reperfused MI

^{19}F-MRI visualized blood monocytes infiltrating infarcted myocardium i*n vivo* in both atorvastatin treated and untreated MI rats (Figure 3.12, a1&b1). The ^{19}F signal intensity correlated well with the density of monocyte/macrophage infiltrates quantified by ED1 IHC (Figure 3.12, c1&c2). Indicated by significantly attenuated ^{19}F signal and proven by ED1 IHC quantification, the recruitment of monocytes and macrophages was significantly attenuated in the treated MI rats (Figure 3.11, b1,2&3), compared to the untreated (Figure 3.12, a1,2&3). Better preserved microvasculature in the treated rats was evident from significantly reduced volume of IMH, an indicator of severe microvascular injury (Figure 3.12, a4&b4).

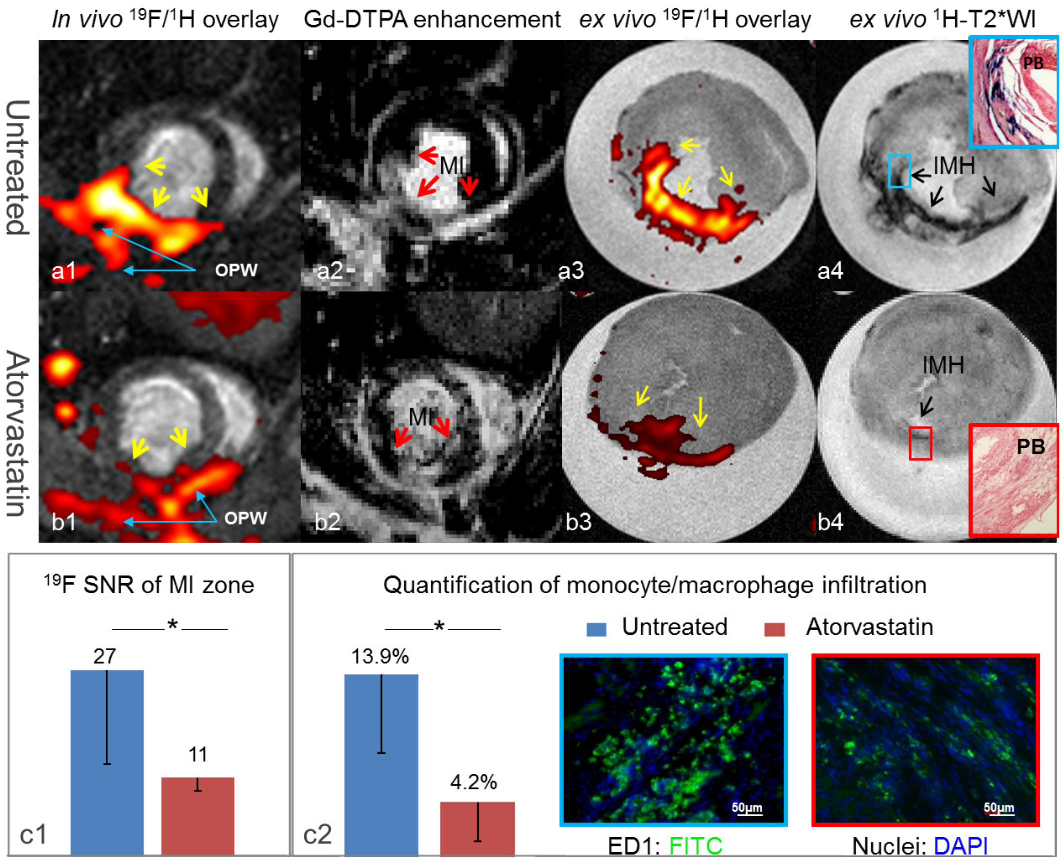

Figure 3.12 ^{19}F/^{1}H-MRI monitoring atorvastatin therapy in reperfused MI in rats.
A representative untreated MI rat: (a1): *in vivo* ^{19}F/^{1}H superposition; (a2): late Gd-DTPA enhancement; (a3): *ex vivo* ^{19}F/^{1}H superposition; (a4): *ex vivo* ^{1}H-T2*WI and Prussian blue (PB) staining of the boxed MI region. A representative atorvastatin treated MI rat: (b1): *in vivo* ^{19}F/^{1}H superposition; (b2): late Gd-DTPA enhancement; (b3): *ex vivo* ^{19}F/^{1}H superposition; (b4): *ex vivo* ^{1}H-T2*WI and Prussian blue (PB) staining of the boxed MI region. (c1): column chart shows signal to noise ratio (SNR) of ^{19}F-MRI in MI zones of the atorvastatin treated and untreated animals. (c2): quantification of monocyte/macrophage infiltrates in atorvastatin treated and untreated MI rats. (yellow arrows: ^{19}F signal in MI zone; red arrows: MI regions; black arrows: IMH areas. OPW: operation wounds. *$p<0.05$.)

3.4 Discussion

In this study, we present the first report of visualizing the dynamic recruitment of monocytes *in vivo* in reperfused MI with MVO and IMH by $^{19}F/^{1}H$-MRI in rats. Monocytes were recruited inhomogeneously in reperfused MI tissue: their infiltration was highly attenuated in MVO regions; in absence of MVO, more intense monocyte infiltration was observed in areas with severe IMH. Compared to the group with isolated IMH, the MVO group exhibited worse long-term functional outcomes.

Tissue heterogeneity of reperfused MI: emphasis on MVO and IMH

Reperfused MI tissue is heterogeneous due to unequal ischemia-reperfuison injuries, susceptibility to ischemia and inflammation *etc*[16]. MVO and IMH occur in a sizable number of acute MI patients after primary percutaneous coronary intervention (PPCI)[111, 160, 161]. They are markers of ischemia-reperfusion injury. MVO refers to hypoperfused myocardial tissue despite the patent epicardial coronary vessel, due to functional or anatomical changes of coronary microcirculation[20]. A large amount of clinical data has convincingly shown that MVO negates the benefit of PPCI. It strongly predicts early adverse left ventricular remodeling and worse recovery of heart function in the long term, independent of MI size[23]. It is also correlated to higher risks of early post-MI complications, heart failure and mortality[162]. IMH is a phenomenon that red blood cells leak into the interstitium during reperfusion after necrosis and loss of capillary integrity during myocardial ischemia[167]. It indicates severe microvascular destruction and cardiomyocyte death[69], associating with poor recovery of LV function and long-term clinical outcomes[71, 72]. However, conflicting results were reported on the independent prognostic value of IMH[71, 72]. It is still a debate whether IMH represents a marker of adverse ventricular remodeling beyond MI size, LV ejection fraction and MVO. MVO and IMH are highly correlated. It is believed that they are secondary phenomena that occur in necrotic myocardium rather than the cause of cardiomyocyte death[69, 168]. Both of them associate with large MI size and prolonged ischemia before reperfusion[111, [160, 161]. However, the distinction between IMH across a spectrum of MVO is not yet elucidated.

Previous studies on MVO and IMH mostly focused on molecular and cellular mechanisms during the first several hours of ischemia-reperfusion and their associations to long-term clinical outcomes. However, questions concerning how the healing process is affected in MVO and IMH, as well as the clear mechanisms that underlie their important prognostic values have not been answered. Partly determined by infarct size, the adverse LV remodeling is also a consequence of the rate of MI healing and the material properties of MI segments[27, 45], which has been evident from the delayed healing and dramatically higher risks of ventricular aneurysm in steroid therapy during acute MI in dogs and patients[169]. MVO and IMH are both confined in necrotic myocardium. Their initial tissue components are presumably similar (mainly necrosis). Therefore, it is important to investigate how monocyte infiltration responses to various severity of ischemia-reperfuison injuries, in particular whether and how necrosis absorption and tissue reparation by monocytes are altered in MVO and IMH.

Monocytes and macrophages were labeled by PFC and unambiguously detected by ^{19}F-MRI

With only one injection on Day 1, CD11b$^+$ cells in blood were efficiently labeled by PFC emulsion at least till Day 7, a time window during which monocytes are recruited actively from blood to MI[32, 170]. CD11b is expressed in monocytes, macrophages, dendritic cells and granulocytes in blood. Macrophages and dendritic cells are rare in blood, and eosinophils and basophils are non-phagocytes; therefore monocytes and neutrophils constituted the majority of the PFC labeled CD11b$^+$ cells in blood to be recruited to MI. Considering that most neutrophils infiltrate MI during the first 24 hours after MI[32] and that we injected PFC emulsion 24 hours after operation, the PFC labeled CD11b$^+$ cells being recruited to MI tissue should mostly be blood monocytes. In addition, PFC emulsion only appeared in cytoplasm of monocytes and macrophages in MI areas on the fluorescent confocal microscopy (Figure 3.8). Therefore, the ^{19}F signal emerging from MI regions was contributed primarily by PFC labeled monocytes and macrophages. Because ^{19}F signal intensity was linearly correlated with the density of ^{19}F spins (Figure 3.10) and was not influenced by strong susceptibility effects with our imaging protocol (Figure 3.9), it indicated the relative amount of monocytes/macrophages in different MI regions, which was further proven by the good correlation of ^{19}F signal intensity on *ex vivo* MRI and the density of monocyte/macrophage infiltration on ED1 staining (Figure 3.6).

Dynamic distribution patterns of monocyte and macrophage in reperfused MI revealed by ^{19}F cellular MRI

^{19}F-MRI revealed that the distribution of monocytes and macrophages was spatially similar on Days 3, 7 and 14 in reperfused MI, while the LV was undergoing dramatic wall thinning and chamber enlargement (Figure 3.3). In contrast, Flogel *et al*. found that the ^{19}F signal positive regions increased in area over time during the first 6 days in occluded MI in mice[121]. This might be due to the different infiltration patterns of inflammatory cells in reperfused and occluded MI: in non-reperfused MI the front of immune cell infiltration starts from the borders of MI and progresses to the center, while in reperfused MI the invasion of neutrophils starts immediately upon reperfusion of the injured myocardium and lasts for around 24 hours. Shortly thereafter, lymphocytes and monocytes are recruited[32, 171].

In addition, we found that the ^{19}F signal intensity was highest on Day 3, suggeting that the density of monocytes was the highest in MI tissue around 3 days after MI. This observation is in agreement with Nahrendorf *et al*.'s findings by flow cytometry to quantify immune cells in acute occluded MI in mice, that the total monocytes number was highest around Day 3[32]. After monocytes differentiated into macrophages, PFC was still retained intracellularly. Then ^{19}F signal represented the density of the sum of monocytes, macrophages and possibly a very small number of dendritic cells in MI. We found that the ^{19}F signal intensities significantly reduced from Day 3 to Day 7 by 24% on, which is in line with Nahrendorf *et al*.'s results[32] but in contrast to Flogel *et al*.'s observations that the ^{19}F signal intensity gradually increased during the first 6 days in non-reperfused MI in mice[121]. On Day 14, the mean ^{19}F signal intensity further decreased from Day7 by about 14%. But the difference was insignificant. However, Nahrendorf *et al*. found a much more dramatic reduction (almost 90%)

of the density of the sum of monocytes, macrophages and dendritic cells from Day 3 to Day 16 in non-reperfused MI in mice by flow cytometry[32]. Further investigations are needed to determine whether the above discrepancies are contributed by different methods applied (^{19}F-MRI rather than flow cytometry) to estimate cell number or/and the different MI models (reperfused and non-reperfused MI) used. As a limit of the *in situ* labeling of blood monocytes by *i.v.* injection of PFC emulsion, the intracellular loading of PFC gradually decreased in circulating monocytes, as indicated by the flow cytometry results. This might complicate the interpretation of ^{19}F signal changes.

Spatial distribution of monocytes and macrophages in heterogeneous tissue of reperfused MI: highly impaired monocyte recruitment in MVO

^{19}F-MRI revealed that the density of monocyte and macrophage in MI zones was in response to the severity of ischemia-reperfusion injury when MVO was absent: the more intense ^{19}F signal distributed in MI regions with severe IMH, an indicator of severe microvascular injury and therefore more tissue necrosis[69]; the less intense ^{19}F signal intensity was found in MI area with less IMH; and the lower ^{19}F signal in the non-hemorrhagic peripheral MI region, where necrosis interlaces with the viable myocardial tissue. Under the above circumstances, the number of the recruited monocytes and their decedent macrophages seems to match the amount of injured tissue to be removed and repaired (Figure 3.3&3.6).

However, even 14 days after MI, highly impaired monocyte and macrophage infiltration was found in MVO regions, which was accompanied by severe IMH. Monocytes and macrophages are indispensable in MI wound healing. It has been shown in mice, when monocytes and macrophages were depleted in the first week after myocardial cryo-injury, the cell debris absorption in myocardium was delayed, furthermore the secretion of transforming growth factor-beta and vascular endothelial growth factor-A was reduced. As a result, neovascularization, myofibroblast infiltration, and collagen deposition were all decreased. Moreover, macrophage depletion resulted in a high mortality rate accompanied by increased left ventricular dilatation and wall thinning[172]. Delayed necrosis absorption and wound healing were also observed in patients when steroid therapies were applied during acute MI, resulting in significantly higher occurrence of aneurism[169]. In our experiments, the MVO regions resembled 'islands' lacking monocytes and macrophages. Such a structure could be fragile and tend to develop profound wall thinning, LV enlargement and rupture. In addition, life threatening arrhythmia might be more likely to occur in such heterogeneous tissue with variable electroconductivities.

In contrast, MI regions with IMH but not involving MVO seem to have "reasonable" monocyte and macrophage infiltrates. The differential innate immune responses to MVO and IMH without MVO suggest that even though being highly correlated and presumably similar in initial tissue composition (mainly necrosis), the subsequent healing processes in these two MI regions appeared differential at least in respect of monocyte recruitment.

In the 28 days follow-up studies, the MVO group demonstrated significantly worse ΔEF in comparison to the IMH group, despite that the initial MI size and function were similar in the two groups. Advancing in parallel with healing, post-MI LV remodeling is a complex, dynamic and time-dependent process, which involves differential alterations between the infarcted and non-infarcted myocardium. The early regional remodeling of the infarcted segments contributes significantly to global LV structural remodeling post-MI. The prolonged exposure of extensive unhealed MI tissue to mechanical deformation forces could lead to greater infarct expansion and promote LV dilatation in the MVO group. In the non-infarcted myocardium, the chronic LV pressure overloading could stimulate interstitial fibrosis, which increases the ventricular stiffness and impairs contractile function, resulting in progressively declined EF. Therefore, the lack of monocytes and macrophages in MVO areas could be responsible for the worse remodeling and function of the MVO group in the long term.

Interestingly, the collagen volume fraction in the MI zones (replacement fibrosis) was significantly higher in the MVO group than in the group of IMH absent of MVO. It was sampled randomly in the entire MI regions, indicating the collective quality of scar formation. The higher collagen volume fraction in the scar seems to more strongly support ventricular morphology. However, the hue analysis of collagen fiber composition showed that the proportion of red fiber (the thickest fiber) was significantly lower in the MVO group. This result might suggest that the collagen fibers were less mature in the scar of MVO hearts on Day 28. Collagen is mainly synthesized and secreted by myofibroblasts. The synthesis and secretion of collagen by myofibroblasts are regulated mainly by mechanical stretching and various chemotactic factors produced by cardiac fibroblasts, proinflammatory cytokines secreted by monocytes, macrophages, T cells and mast cells. They are commonly found in granulation tissues, which typically grow inward from peripheral MI. We observed the presence of (myo)fibroblasts in the MVO corresponding area 14 days after MI. Further investigation is needed to explore the behavior of fibroblasts and (myo)fibroblasts in MVO regions during healing. In addition, it is to be determined how the highly impaired monocyte and macrophage infiltration in MVO regions during acute and sub-acute MI contributes to the patterns of collagen deposition in MVO hearts in the long term.

The highly impaired monocyte and macrophage recruitment in MVO regions, which was associated with the subsequent different patterns of post-MI fibrosis and the worsened long-term outcome of MVO than IMH alone, suggests that MVO and IMH could be differential in the wound healing process. These findings might explain, at least partly, why MVO is associated with adverse LV remodeling and worse clinical outcomes, independent of MI size.

Monocyte recruitmet in MVO: a potential diagnostic marker and therapeutic target

Since MVO independently indicates worse outcomes of reperfused MI, to prevent and reverse MVO are thought to improve prognosis. Efforts have been made to reverse MVO in clinical trials, but the efficacy of achieving tissue perfusion in MVO is not clear[173]. Furthermore, since MVO areas primarily constitute of necrotic tissue, the reversal of MVO is not thought to rescue viable myocardium. Therefore, whether and how the improved tissue perfusion in necrotic myocardium of MVO indeed contributes to improvements of cardiac function and clinical outcomes is to be examined. From our findings, it seems reasonable to promote monocyte recruitment in the treatment of MVO, in order to accelerate the delayed wound healing and improve the compromised tissue property. The difference between MVO area and IMH region in monocyte recruitment perhaps does not merely due to the insufficiency of tissue perfusion, because the infiltration of monocytes and macrophages peaked around Day 3-7 in non-reperfused MI in rats[170] and mice[32, 121]. Further investigations are needed to explore the signaling of inflammation in MVO and IMH regions. This might contribute to potential solutions for accelerating healing process of MI with MVO, by modulating monocyte recruitments in MVO areas.

Monitoring of atorvastatin's therapy on reperfused MI

The ^{1}H-MRI findings support the hypothesis that the atorvastatin-associated beneficial effect of less cardiac muscle loss and adverse LV remodeling might result, at least in part, from the better preserved microcirculation in the area at risk after ischemia-reperfusion. Whether less monocyte and macrophage infiltration in MI was a result of a better salvaged area at risk due to the effect of atorvastatin on microcirculation, and/or it led to less endothelial and cardiomyocyte injury early after reperfusion still needs to be examined. In addition, the long-term benefit of such treatment on cardiac remodeling needs to be investigated.

Advantages of ^{19}F MR cell tracking

Because ^{19}F in living body is too rare to be detected by MRI, the labeled cells are the only source of signal. The unambiguity of ^{19}F signal showed its advantage over iron oxide labeling in MR cell tracking in tissues with strong backgrounds of local T2* effects, for instance in reperfused MI with IMH. According to our results and other studies on large animal or humans, MRI defined IMH occurred in 25-100% reperfused MI, when ischemic assaults lasted for more than 2 hours before reperfusion[72, 111, 174, 175]. The MRI contrast features of IMH dynamically change, corresponding to the integrity of red blood cells, the oxygenation states of hemoglobin and the progress of hemoglobin degradation[175]. The evolution of IMH contrast further complicates the interpretation of MR cell tracking in hemorrhagic MI utilizing iron oxide particles[111]. However, the ^{19}F signal was not influenced by strong local T2* effect and linear to the concentration of PFC; therefore, ^{19}F-MRI allows for specific detection and easier quantification of labeled cells in IMH (Figure 3.5). In addition, ^{19}F-MRI preserves the full capability of ^{1}H-MRI for MI tissue characterization, while cell labeling by iron oxide particles may shorten T2 and T2* of background tissue, which cloud the measurements of edema and IMH.

Edema and IMH are important features of reperfused MI for estimating area at risk and the severity of ischemia-reperfusion injury, respectively. Moreover, ^{19}F-MRI has potential for clinical translation. CE and several other PFCs are biologically inert and their emulsions were approved for clinical use. As estimated, 4000-5500 CD11b^{+} cells could be detected by ^{19}F-MRI (SNR=3) in our setups (Figure 3.1&3.10). Human hearts allow at least 250-folds larger voxel volume (5mm×5mm×20mm) than in rats (1mm×1mm×2mm). Therefore, it should be feasible to image labeled cells in patients.

3.5 Conclusions

In reperfused MI, the monocyte recruitment was in response to the severity of ischemia-reperfusion injury, except for MVO regions, in which the distinct mismatch of the highly impaired monocyte recruitment and the severe ischemia-reperfusion injury was found. In the long-term post-MI, we found significantly increased post-MI fibrosis in MI zones and worse functional recovery in MVO hearts, in comparison to IMH hearts absent of MVO. The healing process and functional outcome indicate that MVO and IMH are closely correlated but yet differential. The impaired monocyte recruitment and the likely lower rate of healing in MVO regions could contribute to its independent prognostic value of worse outcomes in the long term. Further investigations are needed to explore the role of fibroblasts and (myo)fibroblasts in the healing of MVO regions. It is to be determined how such impaired recruitments of monocytes/macrophages during acute/sub-acute MI are related to the increased post-MI fibrosis in the long term.

The combined $^{19}F/^{1}H$-MRI allowed for monitoring the modulation of myocardial monocyte infiltration and revealed a possible mechanism of an anti-inflammatory approach by atorvastatin. This platform might provide a novel and integrated view on tissue injury and its cellular innate immune response after ischemia-reperfusion. It could contribute to gain new insights into the effects of anti-inflammatory therapy in MI and has potential for clinical translation in acute MI patients in the future.

Chapter 4

Quantitative Manganese Enhanced Magnetic Resonance Imaging in Myocardial Ischemic Injury and Heart Failure

4.1 Introduction

Intracellular calcium ion (Ca^{2+}) is a central regulator of cardiac contractility and viability[176]. To sustain intracellular homeostasis of Ca^{2+}, the quantities of Ca^{2+} processed by various routes must balance: the influx of Ca^{2+} into the cell via the surface channels have to be matched by its efflux from the cell by the sodium-calcium (Na–Ca) exchanger; additionally the quantity of Ca^{2+} released from internal sarcoplasmic reticulum stores via the Ca^{2+} release channels must be returned to the sarcoplasmic reticulum (SR) via the SR Ca-ATPase. When transient imbalance occurs, the depletion or augmentation of Ca^{2+} store might lead to inotropic adjustment. There are non-ignorable evidences showing the involvement of deranged Ca^{2+} handling in various scenarios of patholphysiology, for example myocardial stunning[177], hibernation[178], myocardial infarction[150] and heart failure *etc*[179]. Despite its importance in physiology and pathophysiology of myocardium, Ca^{2+} signaling is predominantly studied *in vitro* in single cardiac myocyte settings, due to technical difficulties in measuring this signal *in vivo*.

Manganese ions (Mn^{2+}) are analogues of Ca^{2+}. They can be taken up by cardiac myocytes[151, 152]. Extracellular free Mn^{2+} can compete with Ca^{2+}, get through the voltage operated calcium channels on myocyte membrane and accumulate intracellularly in addictive manner[152, 180]. Mn^{2+} is an excellent MR contrast agent, due to its ability to decrease both T1 and T2 of surrounding water. The MR relaxation rates ($R1=1/T1$ and $R2=1/T2$) are proportional to the effective concentration of Mn^{2+} in tissue[153, 181]. T1 weighted image (T1WI) is a favorable means for detection of Mn^{2+} accumulation in tissue, owning to its positive contrast, higher signal to noise ratio, higher contrast-to-noise ratio and the much larger tissue T1 than T2. In the heart, enhancement of myocardium on T1WI has been demonstrated in animal models by systematic administration of manganese chloride[182, 183] and chelated manganese (Manganese dipyroxyl diphosphate, Mn-DPDP)[184]. However, relatively large quantity of Mn^{2+} is needed to achieve significant enhancement on T1WI. In addition, the enhancement effect is a relative extent with non-ignorable fluctuations resulting from varied TR due to respiratory and cardiac triggering, so that it is difficult to be quantitatively compared in different individuals or in longitudinal studies. Skjold *et al*. was the first to demonstrate quantitative R1 measurements of manganese enhancement by Mn-DPDP in myocardial infarction in patients[185]. Independently, Waghorn *et al*. adapted an ECG-gated, flow-compensated Look-Locker MRI pulse sequence to perform R1 mapping of mouse hearts after intravenous infusion of $MnCl_2$ solution by applying prospectively a fixed R-R period[153]. These advances shed lights on the potential of manganese-enhanced MRI in *in vivo* quantitative investigations of cardiomyocyte calcium handling and characterization of myocardial pathology.

In 1978, manganese was the first MRI contrast agent being discovered by Lauterbur *et al*[186]. They demonstrated that the R1 of liver and the heart were the most significantly enhanced in major organs after intravenous infusion of $MnCl_2$[186]. In 2010, Hu *et al*. described a non-linear relationship between the total dose of intravenously infused Mn^{2+} and R1 changes in blood and myocardium, using T1 mapping in rats. They further highlighted the importance of investigating clearance rates of Mn^{2+} by liver and kidneys, as well as the influence of cardiac function, in order to elucidate the dynamics relating Mn^{2+} contents in blood, myocardium and infusion dose[181]. It is known that the total change of R1 ($\Delta R1$) is linearly correlated to the concentration of Mn^{2+} in blood and myocardium[153, 181]. However, it is not yet well understood how R1 enhancements of myocardium and blood are quantitatively determined by the total Mn^{2+} dose and the rate of Mn^{2+} infusion, despite increasing interests and applications of Mn^{2+} as a functional cardiac MR contrast agent.

To improve the application of quantitative manganese enhanced MRI (MEMRI) in *in vivo* setting and probe dynamic calcium signaling in the heart, several issues need to be addressed: 1) A R1 mapping technique with high temporal resolution is needed to measure the dynamic changes of Mn^{2+} influx and efflux in myocardium *in vivo*. 2) What is the inter-relation between *i.v.* infusion rate/dose and blood/myocardium R1 changes in healthy animals? 3) What are the patterns of R1 enhancement by Mn^{2+} in animal models of myocardial infarction *in vivo*?

In this study, firstly a dynamic fast R1 map technique was developed by adapting a well-established fast R1 mapping MR sequence[187] to achieve a temporal resolution of around 1 minute in rats *in vivo* without breath control. With this method, quantitative MEMRI was performed in healthy rats to reveal the interrelation between *i.v.* infusion rate, accumulative $MnCl_2$ (Mn) dose and dynamic R1 of arterial blood, liver, skeleton muscle and myocardium. Finally quantitative R1 enhancement patterns of MEMRI were characterized in sub-acute and chronic myocardial infarct model in rats.

4.2 Methods and Materials

MR R1 mapping

The MRI sequence for R1 mapping was modified from a previously described inversion recovery snapshot fast low-angle shot (FLASH) sequence[187] by setting a prospectively fixed R-R period for cardiac triggering[153]. Only the first excitation pulse was triggered by actual R wave of the heart circle and the rest was by prospectively set R-R interval value that was determined immediately before starting image acquisition by a home-built cardiac and respiratory monitor. With 2 to 3 segments, 32 to 40 frames of T1WI were acquired for R1 mapping. The imaging parameters were as followed: repetition time 2.5ms, echo time 2ms, flip angle (FA) 3°, field of view (FOV) 4cm×4cm, matrix 64×64, slice thickness 2mm and average 1. Images were obtained in a short-axis imaging plane of mid-ventricle. The acquisition time for each R1 map data set was around 1 minute.

Animal preparation

MEMRI was performed in Lewis rats (male, 200-300g, Charles River, Germany). Animals were initially anesthetized by inhalation of oxygen mixed with 4% isoflurane (Abbott GmbH, Wiesbaden, Germany) and maintained at 2% isoflurane during tail vein catheter procedures. The vein catheter was connected to an infusion line controlled by a micro-infusion pump to precisely supply Mn^{2+} contrast agents.

Manganese enhancement schemes in healthy rats

To investigate the influence of infusion rates of Mn^{2+} solution on $\Delta R1$ in blood, myocardium, liver and skeleton muscle, intravenous administration of Mn^{2+} solution was applied at a low rate of 0.86nmol/min/g (Mn0.86) for 60min in the Group Mn0.86 (n=5), and a high rate of 3.3nmol/min/g (Mn3.3) for 30min in the Group Mn3.3 (n=4). With the two constant infusion rates and relatively long infusion time, $\Delta R1$ in various tissues could be plotted to the function of accumulative dose of Mn^{2+} (converted by infusion rate×infusion time).

Induction of reperfused MI in rats

Reperfused MI was induced via anterior sternotomy under isoflurane (Abbott GmbH, Wiesbaden, Germany) anesthesia in 5 rats (Wistar, female, 200±30g, Charles River, Germany). The left anterior coronary artery was ligated for 120min, followed by removal of the knot. The animal operation was in accordance with the guidelines for research animal care of our institute and approved by the local ethic committee.

In vivo MRI acquisition

After tail vein catheter procedures, the rat was placed in a home-built delivery bed. Anesthesia was maintained by inhalation of 1-2% isoflurane mixed in oxygen. The physiological body temperature was maintained by a warming pad (Winkler GmbH, Germany). In all animals, R1 maps and Cine (FLASH, TE 1.7ms, frames 12-24) of the same image plane at short axis view of mid-ventricle were acquired before (serve as baseline values) and after finishing $MnCl_2$ enhancement. During the infusion of $MnCl_2$ solution, R1 maps were acquired continually to monitor the dynamic changes of R1 in myocardium, arterial blood in LV cavity, skeleton muscle and liver. Additionally, R1 maps were acquired after the end of $MnCl_2$ infusion: in Group Mn0.86 for 20min and in Group Mn3.3 for 15min.

To investigate the quantitative Mn^{2+} uptake in both sub-acute and chronic infarct hearts, MEMRI was performed 7 days (n=3) and 68 days (n=3) after MI operation. First, baseline R1 was measured at the mid-ventricular plane with the same imaging parameters and sequence applied in the Group Mn0.86 and Mn3.3. After that, $MnCl_2$ solution was infused via a tail vein catheter controlled by a micro-infusion pump, at an infusion rate of 3.3nmol/min/g for 30min. In this group R1 maps were acquired during the infusion and 15min after the end of infusion.

Isoflurane was adjusted during $MnCl_2$ infusion to achieve stable ratio of heart beats/respiration (5-6/1). After *in vivo* MRI, tail vein catheters were removed and animals recovered after isoflurane retrieval.

MRI data post-processing and analysis

By using a custom-written Matlab program, spatially resolved T1 maps were calculated pixel-wise based on a monoexponential three parameter least-square fit (fitted function was $A+B\exp(-TR/T1^*)$). A linear correction ($T1=T1^{**}B/A$) proposed by Deichmann *et al.*[188] was used to correct apparent relaxation time T1* from effects of magnetization saturation coming from the Look-Locker pulse train. R1 maps were calculated as the reciprocal of the corrected T1 maps.

The medians of R1 were acquired from the Region of Interest (ROI) of the blood pool in the left ventricle ($R1_{blood}$), myocardium of LV wall ($R1_{myocardium}$), skeleton muscle on the chest wall ($R1_{muscle}$) and liver ($R1_{liver}$). The medians of R1 were plotted synchronically or to the cumulative doses. The R1 value prior to Mn^{2+} infusion ($R1_{baseline}$) was calculated based on the median R1 values of each considered ROI acquired before $MnCl_2$ infusion. The change of R1 ($\Delta R1$) was defined as $\Delta R1=R1-R1_{baseline}$. On the plots, data was gridded on a time scale with 1 minute time interval by using linear interpolation after filtering and smoothing when necessary. In each group of animals, the result was expressed as mean±SD of the medians of the corresponding time point.

Statistics

Results were expressed as mean±SD. Significance of difference between variables was assessed by student t-test. When $p<0.05$, the difference was considered statistically significant.

4.3 Results

In vivo fast R1 mapping of myocardium, arterial blood, liver and skeleton muscle

The raw T1WI (for R1 mapping) sets acquired before $MnCl_2$ infusion and at the end of $MnCl_2$ enhancement at infusion rates of 0.86nmol/min/g and 3.3nmol/min/g were presented in Figure 4.1. Representative dynamic R1 maps at mid-ventricle short-axis view are shown in Figure 4.2. By using the adapted R1 mapping MR sequence, the median T1 value of LV myocardium before Mn enhancement was 1.451±0.086 second (Sec), comparable to the value acquired by ECG triggered, breath controlled and extensively averaged imaging settings in our previous studies (1.45±0.009Sec)[187] as well as to that measured by a Look-Locker sequence with prospectively set R-R period by other groups（1.456±0.173Sec）[153, 181]. Before Mn enhancement, the measured T1 values of arterial blood (in left ventricle), liver and skeleton muscle (in thorax wall) were 1.779±0.185Sec, 0.948±0.104Sec and 1.660±0.036Sec, respectively. The baseline T1 of arterial blood ($T1_{blood}$) was similar to the value of a previous study by Hu *et al*[181]. Upon completion of $MnCl_2$ infusion, significant changes in R1 were observed in myocardium, arterial blood, liver and skeleton muscle in both Groups Mn0.86 and Mn3.3, as shown in Table 4.1.

Figure 4.1 Raw T1WI of R1 mapping data

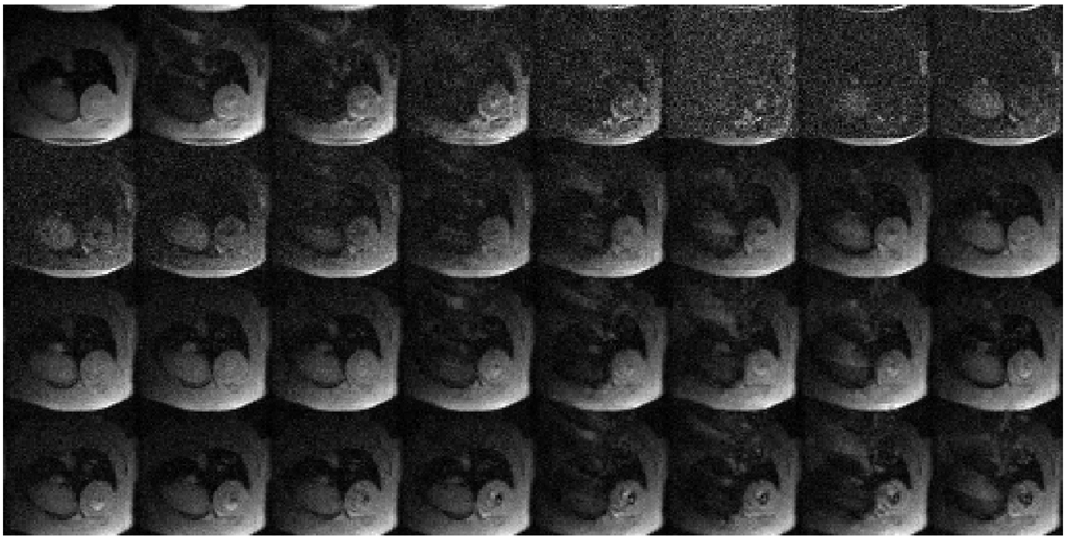

Panel-A Raw T1WI of baseline R1 mapping data

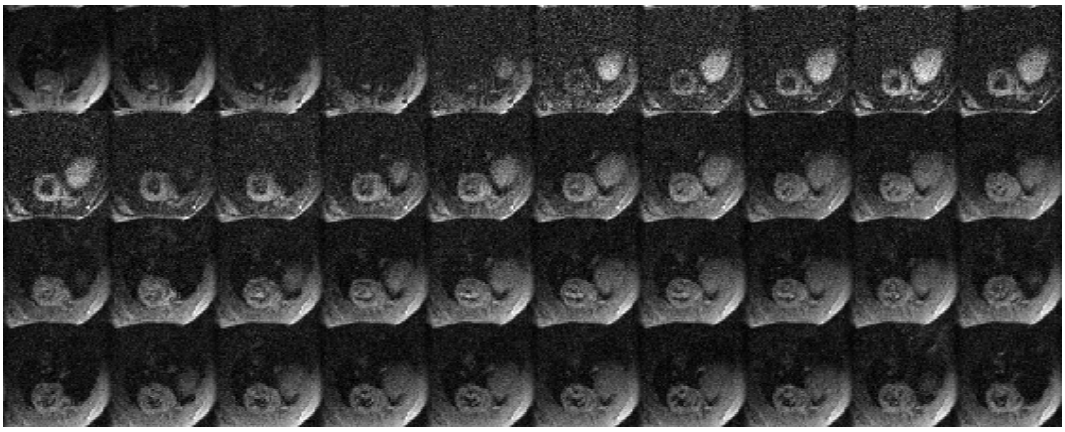

Panel-B Raw T1WI of R1 mapping data after Mn0.86 infusion for 60 minutes (dose=51.6nmol/g)

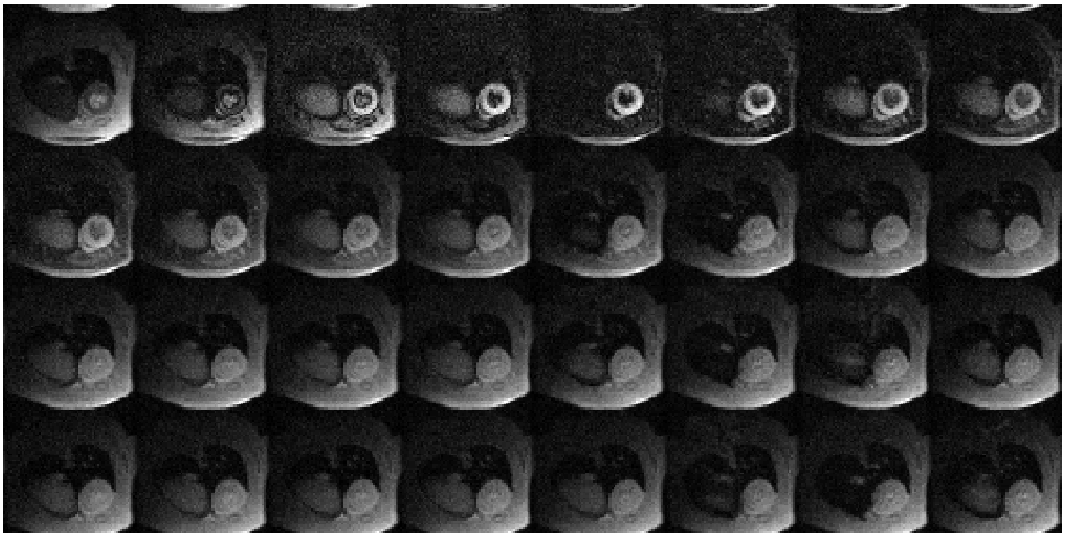

Panel-C Raw T1WI of R1 mapping data after Mn3.3 infusion for 30 minutes (dose=99nmol/g)

R1 dynamics with *i.v.* $MnCl_2$ infusion at low infusion rate of 0.86nmol/min/g

Dynamic R1 changes during Mn0.86 infusion were plotted on Figure 4.4. The infusion of Mn at the rate of 0.86nmol/min/g resulted in slightly elevated ΔR1 in blood ($\Delta R1_{blood(L)}$), reaching the maximum of 0.082±0.097Sec^{-1} at the end of $MnCl_2$ infusion. After Mn infusion finished at 60min, $\Delta R1_{blood(L)}$ dropped rapidly and followed by a modest rise. Conversely, ΔR1 in myocardium after Mn0.86 infusion ($\Delta R1_{myocardium(L)}$) increased almost linearly during Mn^{2+} infusion, reached its maximum of 0.775±0.241 Sec^{-1} at the end of infusion and remained almost constant in the following 30min. Likewise, ΔR1 in liver after Mn0.86 infusion

($\Delta R1_{liver(L)}$) rose during Mn^{2+} infusion but dramatically peaked at the end of infusion, followed by rapid decline. In contrast, $MnCl_2$ infusion only caused slight elevation of $\Delta R1$ in skeleton muscle ($\Delta R1_{muscle(L)}$) at such an infusion rate.

Table 4.1 R1 (Sec^{-1}) of various tissues before (baseline) and after $MnCl_2$ enhancement

	$R1_{blood}$	$R1_{myocardium}$	$R1_{muscle}$	$R1_{liver}$
Baseline	0.579±0.0548	0.691±0.041	0.603±0.0129	1.067±0.1182
Mn0.86	0.644±0.058	1.457±0.244	0.616±0.027	3.783±0.532
Mn3.3	2.563±1.065	4.091±1.790	1.531±1.541	6.644±2.326

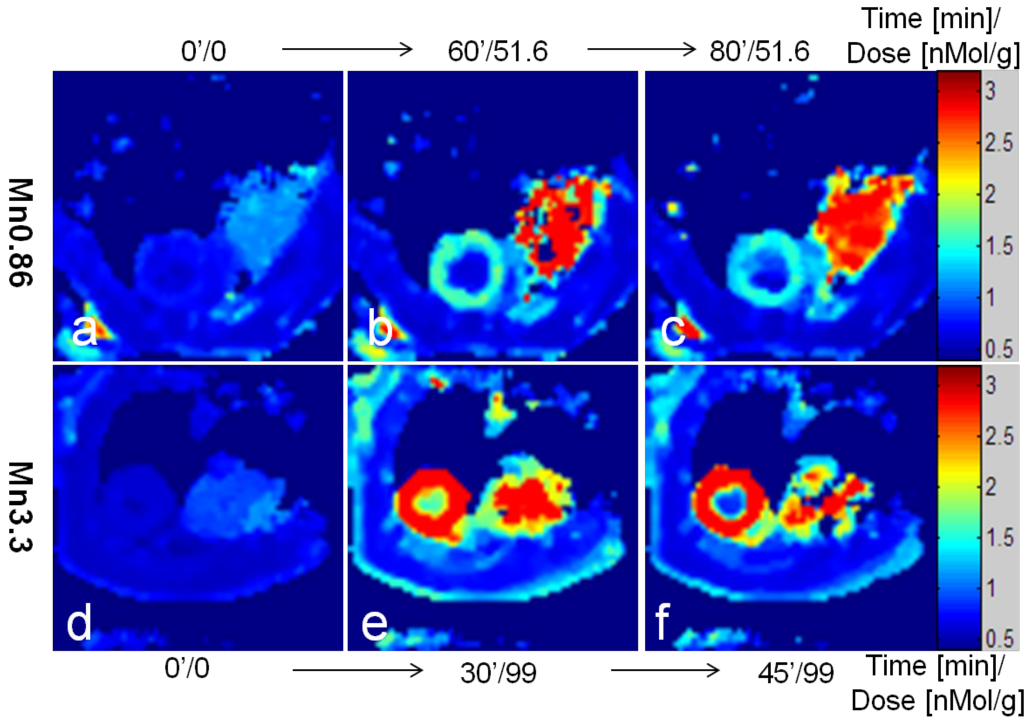

Figure 4.2 R1 maps acquired before, during and after Mn0.86 and Mn3.3 infusion. R1 maps at the infusion rate of Mn0.86: (a) prior to Mn enhancement (baseline), (b) end of 60min infusion, (c) 20min after the end of infusion. R1 maps at infusion rate of Mn3.3: (d) prior to Mn enhancement (baseline), (e) end of 30min infusion, (f) 15min after the end of infusion. Mn0.86 infusion for 60min and Mn3.3 infusion for 30min are equivalent to 51.6nmol/g and 99nmol/g cumulative infusion dose, respectively.

R1 dynamics with *i.v.* $MnCl_2$ infusion at high infusion rate of 3.3nmol/min/g

Dynamic R1 changes during Mn3.3 infusion were plotted on Figure 4.4. High infusion rate of Mn^{2+} at 3.3nmol/min/g induced significant non-linear increase of $\Delta R1_{myocardium(H)}$. In addition, the slope of the later segment (15-30min) was steeper than the early segment (0-15min). Similar to $\Delta R1_{blood(L)}$, $\Delta R1_{blood(H)}$ peaked at the end of Mn infusion and plunged considerably in the first 5min after Mn infusion stopped (30-35min). In skeleton muscle, $\Delta R1_{muscle(H)}$ was in compliance to $\Delta R1_{blood(H)}$, but with much less extent of enhancement.

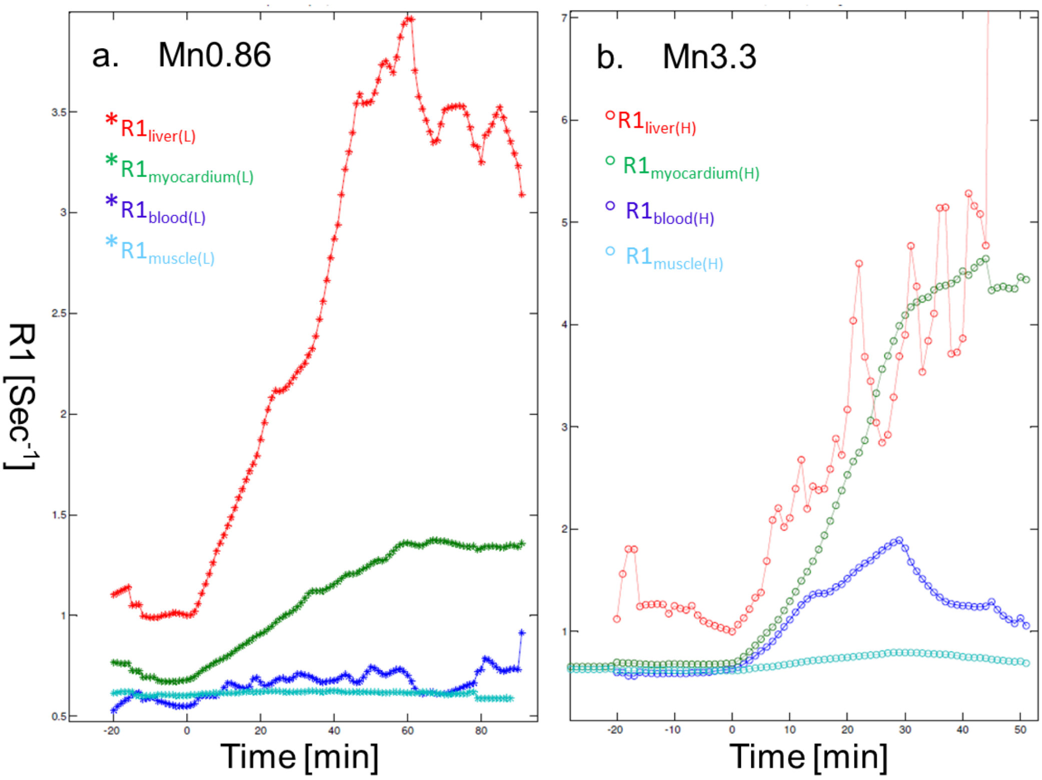

Figure 4.3 Plots of R1 dynamics during and after Mn0.86 and Mn3.3 infusion. (a): at infusion rate of Mn0.86 (***), R1 plots of blood (blue), myocardium (green), liver (red) and muscle (light blue) according to time. (b): at infusion rate of Mn3.3 (ooo), R1 plots of blood (blue), myocardium (green), liver (red) and muscle (light blue) according to time.

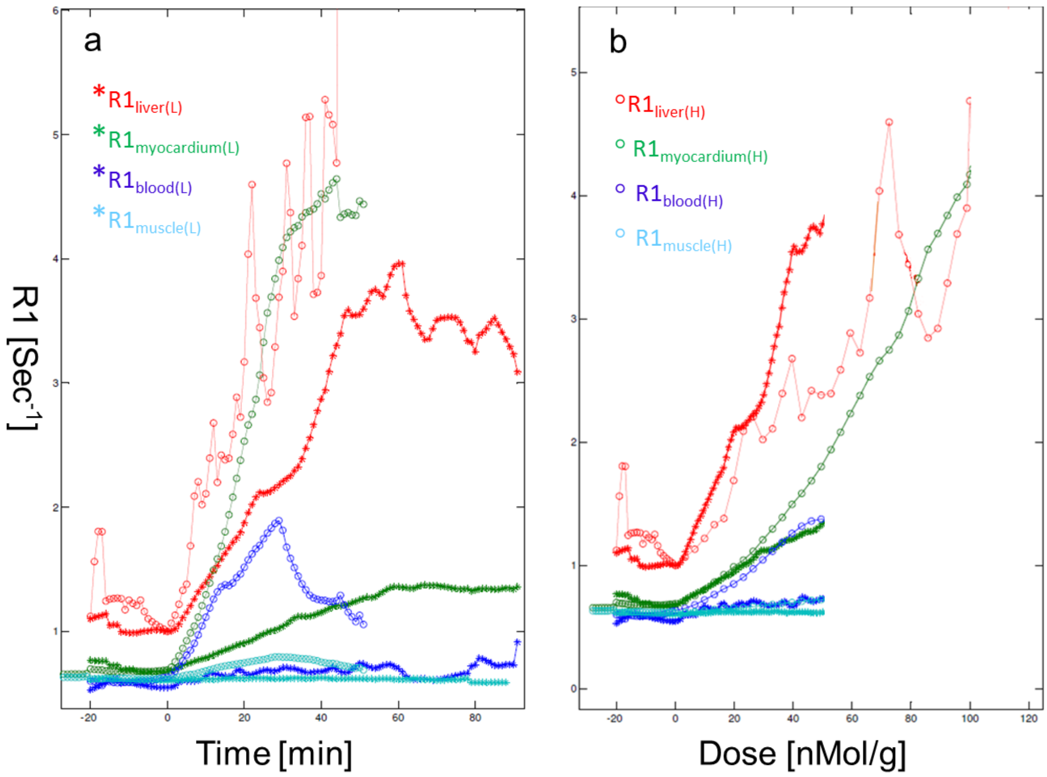

Figure 4.4 Comparison of R1 dynamics induced by Mn0.86 and Mn3.3 infusion. (a): at both infusion rates of Mn0.86 (***) and Mn3.3 (ooo), plots of R1 dynamics to infusion time in blood (blue), myocardium (green), liver (red) and muscle (light blue). (b): at both infusion rates of Mn0.86 (***) and Mn3.3 (ooo), plots of R1 dynamics to cumulative infusion dose in blood (blue), myocardium (green), liver (red) and muscle (light blue).

Influence of $MnCl_2$ infusion rate on R1 dynamics at the same dose

Dynamic R1 changes with low (Mn0.86) and high (Mn3.3) infusion rates were plotted to the dose of $MnCl_2$ on Figure 4.4. Given the same total $MnCl_2$ dose, $MnCl_2$ infusion rate significantly influenced $\Delta R1$ in various tissues. It has more direct and apparent effect on $\Delta R1_{blood}$: at the dose of 51.6nmol/g (equivalent to 60 minutes infusion of Mn0.86 and 15.6 minutes of Mn3.3), $\Delta R1_{blood}$ was about 6 folds higher (0.8047±0.2014 Sec^{-1} vs 0.1341±0.0.0458 Sec^{-1}) with the infusion rate of 3.3nmol/min/g than with that of 0.86nmol/min/g. At that dose, even though less dramatic than $\Delta R1_{blood}$, $\Delta R1_{myocardium(L)}$ was lower than $\Delta R1_{myocardium(H)}$ by 0.61 Sec^{-1}. It is demonstrated in Figure 4.5. It seems that $MnCl_2$ concentration in blood (indicated by $\Delta R1_{blood}$) directly affected enhancement patterns of $\Delta R1_{myocardium}$: when it was very low ($\Delta R1_{blood(L)}$), the rate of $\Delta R1_{myocardium}$ was almost constant, which produced an almost linearly rising curve during Mn^{2+} infusion; when it was high ($\Delta R1_{blood(H)}$), the rate of $\Delta R1_{myocardium}$ was increasing, which produced a

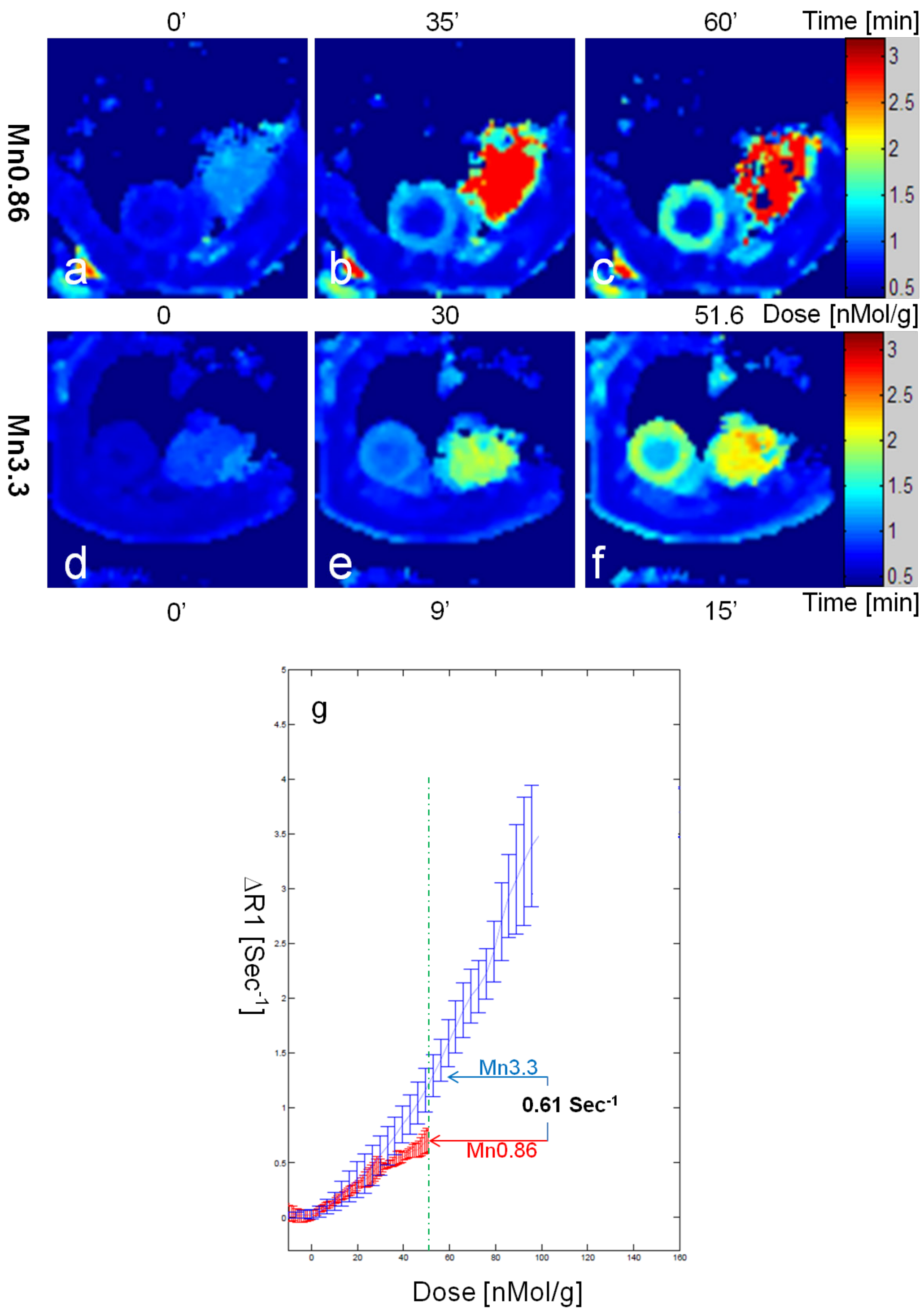

Figure 4.5 Influence of $MnCl_2$ infusion rates on ΔR1 at the same cumulative dose. R1 maps acquired at the infusion rate of Mn0.86: (a) before Mn infusion (baseline), (b) 35min after the start of infusion and (c) 60min after the start of infusion. R1 maps acquired at the infusion rate of Mn3.3: (d) before Mn infusion (baseline), (e) 9min after the start of infusion and (f) 15min after the start of infusion. (b&e) were acquired at the same cumulative dose of $MnCl_2$ at 30nmol/g. (c&f) were acquired at the same cumulative infusion dose of $MnCl_2$ at 51.6nmol/g. (g) the plots of ΔR1 in myocardium to the cumulative doses. At the same doses, the infusion rate of Mn3.3 resulted in greater $\Delta R1_{myocardium}$, in comparison to the infusion rate of Mn0.86 (0.61Sec^{-1} higher at the cumulative dose of 51.6nmol/min).

non-linear curve with increasing slope. In addition, high blood $MnCl_2$ level continued to elevate $\Delta R1_{myocardium(H)}$ even after stopping high rate $MnCl_2$ infusion. In contrast, low blood Mn level after the end of $MnCl_2$ infusion at low rate (0.86nmol/min/g) didn't continue to escalate $\Delta R1_{myocardium(L)}$. Similarly, $\Delta R1_{muscle(H)}$ was significantly higher than $\Delta R1_{muscle(L)}$ (Figure 4.4).

R1 dynamics in sub-acute and chronic MI rats

R1 maps and dynamic ΔR1 plots of sub-acute and chronic MI before and after Mn3.3 were presented in Figure 4.6 and 4.7, respectively. Blood ΔR1 of sub-acute MI on Day 7 ($\Delta R1_{blood(MI\_D7)}$) was significantly reduced to almost half of that in non-infarcted rats (control, Mn3.3). In contrast, blood ΔR1 of chronic MI rats on Day 68 ($\Delta R1_{blood(MI\_D68)}$) was similar to that of the control (Figure 4.7, Panel-A). In MI zones, ΔR1 on Day 7 ($\Delta R1_{MI(MI\_D7)}$) was significantly lower than $\Delta R1_{myocardium}$ in non-infarcted rats with Mn3.3 ($\Delta R1_{myocardium(H)}$) and ΔR1 of remote non-infarcted myocardium of infarct rats ($\Delta R1_{Remote(MI\_D7)}$). On Day 68, ΔR1 of MI segments ($\Delta R1_{MI(MI\_D68)}$) increased significantly. However, the ΔR1 enhancement of MI zone was mainly induced by the composition of blood volume with increased $\Delta R1_{blood}$ and a small fraction of Mn^{2+} that permeated to extravasculature. In contrast, the non-infarcted Group Mn3.3 showed continuous fast increase of $\Delta R1_{myocardium}$ during Mn^{2+} infusion and followed by slight rise in the subsequent 15min (Figure 4.7, Panel-B). 7 days after MI, the remote non-infarcted myocardium demonstrated almost 50% attenuated ΔR1 enhancement ($\Delta R1_{remote(MI\_D7)}$) during Mn3.3 infusion, in comparison to the control on the same day. But it differed from ΔR1 of the infarcted segments in sub-acute phase (Day 7) by much faster R1 increase beyond $\Delta R1_{blood(MI\_D7)}$ during Mn infusion (Figure 4.7, Panel-C). ΔR1 of peripheral MI areas ($\Delta R1_{periMI(MI\_D7)}$) and $\Delta R1_{remote(MI\_D7)}$ shared similar characteristics in enhancement patterns (Figure 4.7, Panel-D). Notably, both $\Delta R1_{periMI(MI\_D68)}$ and $\Delta R1_{remote(MI\_D68)}$ were much recovered, even though still slightly below that of the control. In sub-acute and chronic MI, differential patterns of ΔR1 dynamics appeared in the remote non-infarcted myocardium, 15min after the end of Mn3.3 infusion. In sub-acute MI, $\Delta R1_{remote(MI\_D7)}$ declined fast after the end of Mn infusion. In contrast, $\Delta R1_{remote(MI\_D68)}$ mostly remained constant during this period, similarly to that of non-infarcted rats.

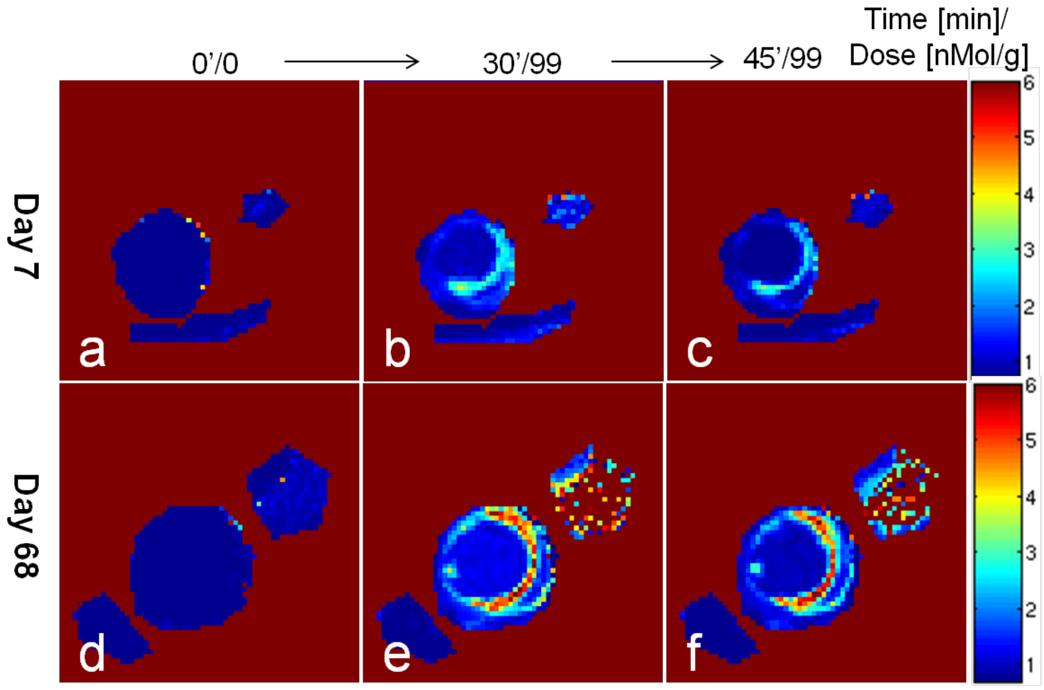

Figure 4.6 R1 maps on Day 7 and Day 68 of the same MI heart of rat with Mn3.3 infusion. On Day 7 post-MI, R1 maps were acquired: (a) before the start of Mn infusion (baseline), (b) at the end of 30min infusion and (c) 15min after the end of infusion. On Day 68 after MI, R1 maps were acquired again in the same animal: (d) before the start of Mn infusion (baseline), at the end of 30min Mn infusion and (f) 15min after the end of Mn infusion.

In addition, the ΔR1 plots of individual animal could provide specific information concerning MI characteristics. As on Figure 4.7, Panel-E shows the mean $\Delta R1_{MI}$ plot of the whole group of chronic infarct rats (Day 68 post-MI), together with the individual $\Delta R1_{MI}$ plots of each animal in this group. The $\Delta R1_{MI}$ enhancement patterns of the three individuals in the group were similar during the infusion of Mn3.3, well-presented by the group mean plots. However, one of the individual exhibited sustained $\Delta R1_{MI}$ after the end of Mn3.3 infusion, which likely indicates significant amount of viable myocardium in the MI zone. The $\Delta R1_{MI}$ plots of the other two animals showed high compliance to $\Delta R1_{blood,}$ which suggests a lack of viable myocardium. However, this difference was not well presented by the group mean $\Delta R1_{MI}$ plots.

Figure 4.7 Dynamic ΔR1 measurements of MI rats with Mn3.3 infusion.

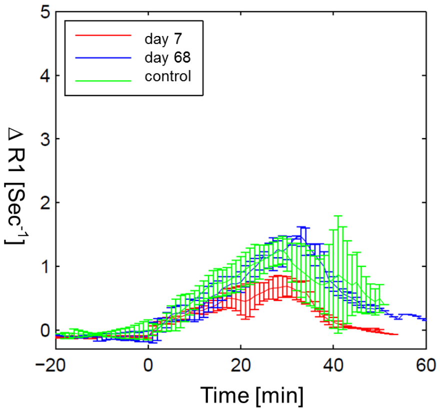

Panel-A $\Delta R1_{blood}$ (mean±SD) plots of MI and control rats on Days 7 and 68 after infarction. $\Delta R1_{blood}$ of MI rats on Day 7 (red curve) was significantly lower than $\Delta R1_{blood}$ of control rats (green curve) or MI rats on Day 68 (blue curve).

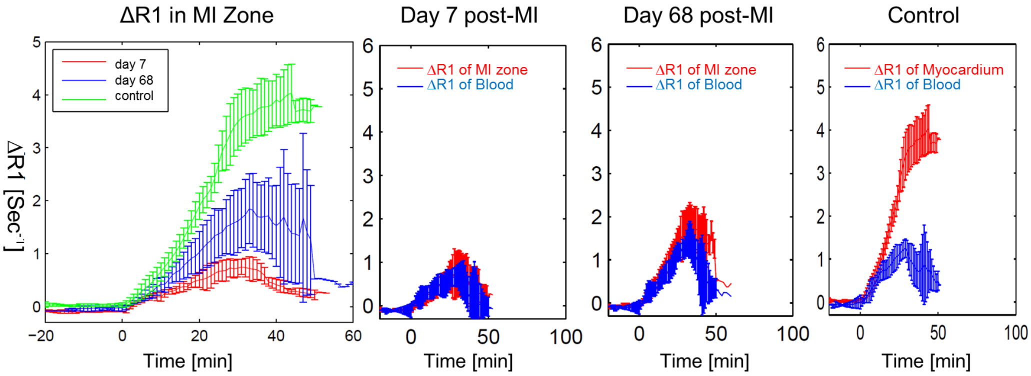

Panel-B $\Delta R1_{MI}$ (mean±SD) plots of MI rats on Days 7 and 68 after infarction, as well as the relation between $\Delta R1_{MI}$ and $\Delta R1_{blood}$. $\Delta R1_{MI}$ on Days 7 and 68 post-MI were similar to their corresponding $\Delta R1_{blood}$. $\Delta R1_{MI}$ on Day 7 was lower than that on Day 68 post-infarction.

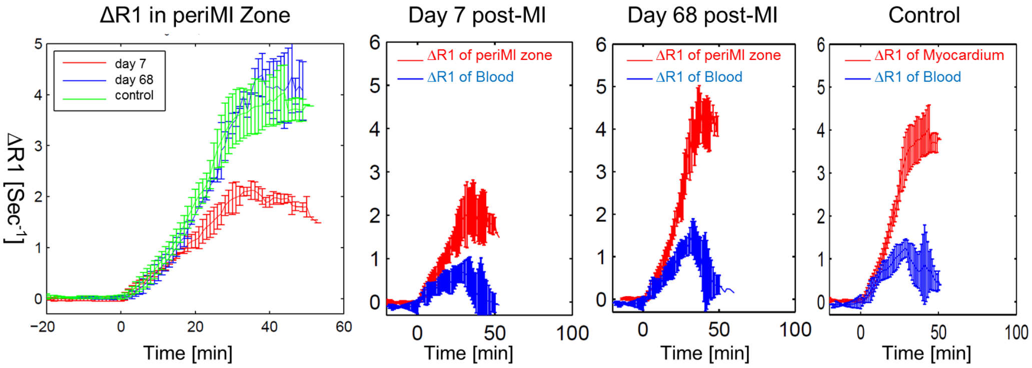

Panel-C $\Delta R1_{periMI}$ (mean±SD) plots of MI rats on Days 7 and 68 after infarction, as well as the relation between $\Delta R1_{periMI}$ and $\Delta R1_{blood}$. $\Delta R1_{periMI}$ on Day 68 appeared similar to $\Delta R1_{myocardium}$ of control rats. However, $\Delta R1_{periMI}$ on Day 7 was much lower than that on Day 68, probably due to the decreased $\Delta R1_{blood}$.

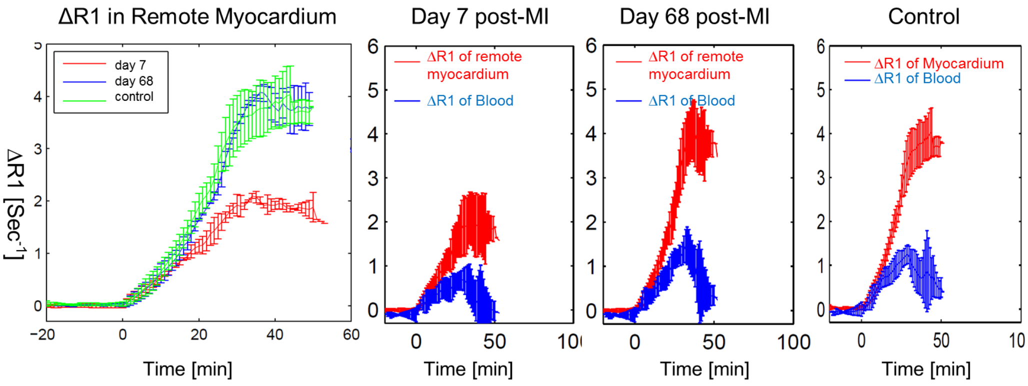

Panel-D $\Delta R1_{remote}$ (mean±SD) plots of MI rats on Days 7 and 68 after infarction, as well as the relation between $\Delta R1_{remote}$ and $\Delta R1_{blood}$. $\Delta R1_{remote}$ on Day 68 appeared similar to $\Delta R1_{myocardium}$ of control rats. However, $\Delta R1_{remote}$ on Day 7 is lower than that on Day 68, probably due to the decreased $\Delta R1_{blood}$.

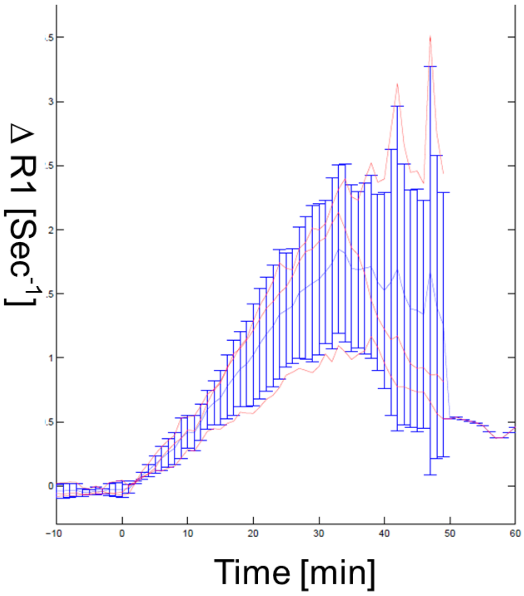

Panel-E Plots of $\Delta R1_{MI}$ on Day 68 post-MI. Red curves: $\Delta R1_{MI}$ of individual animals. Blue curve: $\Delta R1_{MI}$ of the group mean±SD. Large variations of $\Delta R1_{MI}$ were seen among the individual animals, especially after the end of Mn3.3 infusion. The two red curves with fast decline of $\Delta R1_{MI}$, after the end of Mn infusion, probably suggest transmural MI with very few viable myocardium. The red curve with sustained $\Delta R1_{MI}$ after the end of Mn infusion was probably a non-transmural MI containing significant amount of viable myocardium.

4.4 Discussion

The adapted fast R1 mapping method in this study was able to simultaneously measure dynamic R1 changes in myocardium, blood, skeleton muscle and liver *in vivo*, with a temporal resolution of around 1 minute. Waghorn *et al.* were among the first to apply R1 maps to quantitatively study Mn enhancement in myocardium *in vivo* at high field MRI[153]. They also suggested that their method has potential to quantitatively investigate calcium signaling in myocardium *in vivo*. However, the long acquisition time of 45min for one R1 map largely limited their method to achieve precise and dynamic results *in vivo*, because the concentration of intracellular Mn^{2+} gradually decreases after the cease of $MnCl_2$ infusion. They showed almost 80% reduction of R1 in myocardium 3-4 hours after infusion. Therefore, the decline of R1 in myocardium is expected to be significant during the 45-minute acquisition of R1 map. On the other hand, such a long image acquisition time does not allow monitoring of fast dynamic changes of R1 in myocardium and other tissues or organs (*e.g.* blood, liver), which are critical in understanding the *in vivo* kinetics of $MnCl_2$[180]. In addition, the observation of modulated calcium influx by inotropic agents or pathophysiology demands rapid measurements of R1. Our dynamic R1 mapping method with high temporal and spatial resolution sensitively detected a wide range of R1 changes caused by $MnCl_2$ infusion, which has gained new insights concerning the interrelations between $MnCl_2$ infusion rates/doses and $\Delta R1$ in various tissues. In addition, differences in $MnCl_2$ kinetics and R1 enhancement patterns were observed between sub-acute and chronic MI rats *in vivo*. These findings might be valuable for 1) better understanding of the complex kinetics of Mn^{2+} contrast agent *in vivo*, 2) realizing the potential of Mn^{2+} contrast agents for quantitative studies of calcium signaling *in vivo* and 3) the clinical translation of MEMRI in the future.

Infusion rates of $Mn2^+$ directly influenced concentrations of $Mn2^+$ in blood

The constant *i.v.* infusion rate resulted in increasing concentrations of blood Mn^{2+} and accumulative doses with time. It is known that the clearance of free Mn^{2+} from plasma is a fast multi-component process with half-life times shorter than 1-2 minutes[189-191]. After intravenous injection, a majority of Mn^{2+} ions quickly bind to plasma macromolecules. The rest of the free Mn^{2+} has a kinetics that is largely unknown. A higher infusion rate of Mn^{2+} resulted in higher concentrations of both the free and bound Mn^{2+} in blood, even though it is unclear what is the exact ratio between the two in blood. Our results indicated that there was more 'in' (*i.v.* infusion) than 'out' (clearance from circulation) of Mn^{2+} in blood during infusions of Mn0.86 and Mn3.3, resulting in gradual rise of Mn^{2+} concentration in blood. This accumulation of Mn^{2+} in blood impacted the R1 enhancement patterns in both myocardium and skeleton muscle. In the former, the rate of $\Delta R1_{myocardium}$ increased with time during Mn^{2+} infusion, most likely due to the increased supply of free Mn^{2+} for active uptake by cardiac myocytes. In contrast, relaxed skeleton muscle didn't take up Mn^{2+} actively due to the lack of excitement. Its ΔR1 was mostly contributed by the elevated ΔR1 of blood in tissue. Therefore, the increasing concentration of Mn^{2+} in blood during infusion needs to be considered, especially when quantitative dynamic observation is desired for measuring tissue activity *e.g.* quantitative calcium influx in myocardium, by applying a constant rate of Mn^{2+} infusion. It seems that a lower infusion rate of Mn^{2+} is more likely to deliver a close-constant supply of free Mn^{2+} in blood.

Infusion rates of Mn^{2+} significantly affected R1 enhancement patterns of myocardium

Infusion rates of Mn^{2+} significantly influenced total concentration of Mn^{2+} in arterial blood as well as the relationship between $MnCl_2$ doses and ΔR1 of various tissues. $\Delta R1_{blood(H)}$ was much higher than $\Delta R1_{blood(L)}$, given the same total dose of Mn. Moreover, a low infusion rate of Mn (0.86nmol/min/g) delivered close-linear increase of $\Delta R1_{myocardium(L)}$, in the dose range of 0-51.6nmol/g. However, in the same dose range, a high infusion rate of Mn (3.3nmol/min/g) produced greater $\Delta R1_{myocardium}$ with faster increase (steeper slop on ΔR1 plots). For example, the mean $\Delta R1_{myocardium(H)}$ was $0.61 Sec^{-1}$ greater than the mean $\Delta R1_{myocardium(L)}$ at the dose of 51.6nmol/g. It is also noted that $\Delta R_{blood(H)}$ was around $0.67\ Sec^{-1}$ higher than $\Delta R_{blood(L)}$. As estimated, the blood volume fraction (with $\Delta R_{blood(H)}$) in myocardium could only contribute around $0.2\ Sec^{-1}$ or less to the $\Delta R_{myocardium(H)}$ at such dose, when the blood volume fraction of myocardium is 10-15%. Therefore, the significantly higher $\Delta R_{myocardium(H)}$ should be a result of substantially more uptake of Mn^{2+} in cardiomyocytes. The significantly greater $\Delta R1_{myocardium(H)}$ at the

$MnCl_2$ dose of 51.6nmol/g projects an even larger difference at higher doses of $MnCl_2$ infusion. It seems that a higher infusion rate of Mn^{2+} is more efficient for R1 enhancement of myocardium, given the same cumulative dose.

Unexpected reduction of $\Delta R1_{blood}$ in sub-acute MI rats

The significantly reduced $\Delta R1_{blood}$ in sub-acute MI rats (Day 7) was surprising. Assuming the clearance of $MnCl_2$ is considerably influenced by hemodynamics and heart function, it is still difficult to explain the large difference between $\Delta R1_{blood}$ in sub-acute (Day 7) and chronic (Day 68) MI rats, since the ejection fraction is normally only a few percentage difference between sub-acute and chronic MI. In addition, $\Delta R1_{blood}$ of chronic MI rats was similar to that of non-infarcted animals. Nevertheless, this finding highlights the importance of relating $\Delta R1_{myocardium}$ to the corresponding $\Delta R1_{blood}$, in order to avoid mis-interpretation of quantitative R1 enhancement in myocardium.

In addition, it seems that the Ca^{2+} efflux was modulated in the remote non-infarcted myocardium during sub-acute MI phase, based on the observation of the rapid decrease of R1 after Mn3.3 infusion (30-45min) on Day 7. This could not be easily explained by the lower $R1_{blood}$ in MI rats on Day 7, because no obvious reduction on $R1_{myocardium(L)}$ was seem after Mn0.86 infusion (60-90min) in the Group Mn0.86. The significance of this phenomenon is to be determined.

$\Delta R1_{myocardium}$ is closely related to $\Delta R1_{blood}$ and other factors

Mn^{2+} enhancement in myocardium is mainly determined by 1) the capability of active uptake of Mn^{2+} into cardiomyocytes by L-type calcium channels, 2) the permeability of cell membrane to allow for efflux of Mn^{2+}, 3) the concentration of Mn^{2+} in perfusion blood and 4) the arterial perfusion of myocardium. To investigate 1) and 2), the concentration of Mn^{2+} in blood and arterial perfusion needs to be controlled. In sub-acute MI (Day 7) rats, the significantly reduced $R1_{blood}$ suggested a lower Mn^{2+} concentration in blood. Associating with changes in regional and global contractility, LV remodeling also occurs in microvasculature and perfusion in remote non-infarcted myocardium. Therefore, it is critical to relate $\Delta R1_{myocardium}$ to $\Delta R1_{blood}$ and myocardial arterial perfusion, when MEMRI is interpreted quantitatively to extract biological meanings.

4.5 Conclusions

We improved the quantitative manganese enhanced MRI method and applied it in both sub-acute and chronic MI rats, to probe the influx and efflux of calcium ions in infarcted and non-infarcted myocardium *in vivo*. We revealed that intravenous infusion rates of manganese significantly influenced the change of R1 in blood and therefore that of R1 in myocardium, given the same total infusion dose. Interestingly, significantly reduced R1 enhancement was observed in various tissues in sub-acute MI rats, in comparison to both control and chronic MI rats. This phenomenon seems largely, if not entirely, due to the significantly reduced manganese ion concentration in arterial blood in sub-acute MI rats. These findings highlight the importance of relating R1 enhancement in myocardium to the changes of R1 in blood and myocardial arterial perfusion, when interpreting quantitative MEMRI as a surrogate of calcium activities in myocardium.

Bibliography

1. National heart, lung, and blood institute. Nhlbi financial year 2008 fact book. http://www.nhlbi.nih.gov/about/factbook/toc.htm.
2. Klabunde RE. Cardiovascular physiology concepts 2th edition. *Lippincott Williams&Wilki*. 2012
3. Bers DM. Cardiac excitation-contraction coupling. *Nature*. 2002;415:198-205
4. Langer GA. The intrinsic control of myocardial contraction--ionic factors. *N Engl J Med*. 1971;285:1065-1071
5. Langer GA. Heart: Excitation-contraction coupling. *Annu Rev Physiol*. 1973;35:55-86
6. Ausprunk DH, Folkman J. Migration and proliferation of endothelial cells in preformed and newly formed blood vessels during tumor angiogenesis. *Microvasc Res*. 1977;14:53-65

7. Dejana E, Languino LR, Polentarutti N, Balconi G, Ryckewaert JJ, Larrieu MJ, Donati MB, Mantovani A, Marguerie G. Interaction between fibrinogen and cultured endothelial-cells - induction of migration and specific binding. *Journal of Clinical Investigation*. 1985;75:11-18

8. Senger DR, Perruzzi CA, Streit M, Koteliansky VE, de Fougerolles AR, Detmar M. The alpha(1)beta(1) and alpha(2)beta(1) integrins provide critical support for vascular endothelial growth factor signaling, endothelial cell migration, and tumor angiogenesis. *Am J Pathol*. 2002;160:195-204

9. Senger DR, Ledbetter SR, Claffey KP, Papadopoulos-Sergiou A, Peruzzi CA, Detmar M. Stimulation of endothelial cell migration by vascular permeability factor/vascular endothelial growth factor through cooperative mechanisms involving the alphavbeta3 integrin, osteopontin, and thrombin. *Am J Pathol*. 1996;149:293-305

10. Akiyama SK, Yamada SS, Chen WT, Yamada KM. Analysis of fibronectin receptor function with monoclonal antibodies: Roles in cell adhesion, migration, matrix assembly, and cytoskeletal organization. *J Cell Biol*. 1989;109:863-875

11. Duncker DJ, Bache RJ. Regulation of coronary blood flow during exercise. *Physiol Rev*. 2008;88:1009-1086

12. Steenbergen C, Murphy E, Levy L, London RE. Elevation in cytosolic free calcium concentration early in myocardial ischemia in perfused rat heart. *Circ Res*. 1987;60:700-707

13. Reimer KA, Lowe JE, Rasmussen MM, Jennings RB. The wavefront phenomenon of ischemic cell death. 1. Myocardial infarct size vs duration of coronary occlusion in dogs. *Circulation*. 1977;56:786-794

14. Kloner RA, Jennings RB. Consequences of brief ischemia: Stunning, preconditioning, and their clinical implications: Part 1. *Circulation*. 2001;104:2981-2989

15. Kloner RA, Jennings RB. Consequences of brief ischemia: Stunning, preconditioning, and their clinical implications: Part 2. *Circulation*. 2001;104:3158-3167

16. Yellon DM, Hausenloy DJ. Myocardial reperfusion injury. *N Engl J Med*. 2007;357:1121-1135

17. Jennings RB, Murry CE, Steenbergen C, Jr., Reimer KA. Development of cell injury in sustained acute ischemia. *Circulation*. 1990;82:II2-12

18. Stone GW. Angioplasty strategies in st-segment-elevation myocardial infarction: Part i: Primary percutaneous coronary intervention. *Circulation*. 2008;118:538-551

19. Braunwald E, Kloner RA. The stunned myocardium: Prolonged, postischemic ventricular dysfunction. *Circulation*. 1982;66:1146-1149

20. Bekkers SC, Yazdani SK, Virmani R, Waltenberger J. Microvascular obstruction: Underlying pathophysiology and clinical diagnosis. *J Am Coll Cardiol*. 2010;55:1649-1660

21. Kawaguchi M, Takahashi M, Hata T, Kashima Y, Usui F, Morimoto H, Izawa A, Takahashi Y, Masumoto J, Koyama J, Hongo M, Noda T, Nakayama J, Sagara J, Taniguchi S, Ikeda U. Inflammasome activation of

cardiac fibroblasts is essential for myocardial ischemia/reperfusion injury. *Circulation*. 2011;123:594-604

22. Kloner RA, Ganote CE, Jennings RB. The "no-reflow" phenomenon after temporary coronary occlusion in the dog. *J Clin Invest*. 1974;54:1496-1508
23. Wu KC, Zerhouni EA, Judd RM, Lugo-Olivieri CH, Barouch LA, Schulman SP, Blumenthal RS, Lima JA. Prognostic significance of microvascular obstruction by magnetic resonance imaging in patients with acute myocardial infarction. *Circulation*. 1998;97:765-772
24. Frangogiannis NG, Smith CW, Entman ML. The inflammatory response in myocardial infarction. *Cardiovasc Res*. 2002;53:31-47
25. Torre-Amione G. Immune activation in chronic heart failure. *Am J Cardiol*. 2005;95:3C-8C; discussion 38C-40C
26. Levick SP, Melendez GC, Plante E, McLarty JL, Brower GL, Janicki JS. Cardiac mast cells: The centrepiece in adverse myocardial remodelling. *Cardiovasc Res*. 2011;89:12-19
27. Nahrendorf M, Pittet MJ, Swirski FK. Monocytes: Protagonists of infarct inflammation and repair after myocardial infarction. *Circulation*. 2010;121:2437-2445
28. Vandervelde S, van Amerongen MJ, Tio RA, Petersen AH, van Luyn MJ, Harmsen MC. Increased inflammatory response and neovascularization in reperfused vs. Non-reperfused murine myocardial infarction. *Cardiovasc Pathol*. 2006;15:83-90
29. Minatoguchi S, Takemura G, Chen XH, Wang N, Uno Y, Koda M, Arai M, Misao Y, Lu C, Suzuki K, Goto K, Komada A, Takahashi T, Kosai K,

Fujiwara T, Fujiwara H. Acceleration of the healing process and myocardial regeneration may be important as a mechanism of improvement of cardiac function and remodeling by postinfarction granulocyte colony-stimulating factor treatment. *Circulation*. 2004;109:2572-2580

30. Shi C, Pamer EG. Monocyte recruitment during infection and inflammation. *Nat Rev Immunol*. 2011;11:762-774
31. Gordon S, Taylor PR. Monocyte and macrophage heterogeneity. *Nat Rev Immunol*. 2005;5:953-964
32. Nahrendorf M, Swirski FK, Aikawa E, Stangenberg L, Wurdinger T, Figueiredo JL, Libby P, Weissleder R, Pittet MJ. The healing myocardium sequentially mobilizes two monocyte subsets with divergent and complementary functions. *J Exp Med*. 2007;204:3037-3047
33. Tsujioka H, Imanishi T, Ikejima H, Kuroi A, Takarada S, Tanimoto T, Kitabata H, Okochi K, Arita Y, Ishibashi K, Komukai K, Kataiwa H, Nakamura N, Hirata K, Tanaka A, Akasaka T. Impact of heterogeneity of human peripheral blood monocyte subsets on myocardial salvage in patients with primary acute myocardial infarction. *J Am Coll Cardiol*. 2009;54:130-138
34. Frangogiannis NG, Mendoza LH, Lindsey ML, Ballantyne CM, Michael LH, Smith CW, Entman ML. Il-10 is induced in the reperfused myocardium and may modulate the reaction to injury. *J Immunol*. 2000;165:2798-2808
35. Frangogiannis NG. Regulation of the inflammatory response in cardiac repair. *Circ Res*. 2012;110:159-173

36. van den Borne SW, Diez J, Blankesteijn WM, Verjans J, Hofstra L, Narula J. Myocardial remodeling after infarction: The role of myofibroblasts. *Nat Rev Cardiol*. 2010;7:30-37

37. Ducharme A, Frantz S, Aikawa M, Rabkin E, Lindsey M, Rohde LE, Schoen FJ, Kelly RA, Werb Z, Libby P, Lee RT. Targeted deletion of matrix metalloproteinase-9 attenuates left ventricular enlargement and collagen accumulation after experimental myocardial infarction. *J Clin Invest*. 2000;106:55-62

38. Soonpaa MH, Field LJ. Survey of studies examining mammalian cardiomyocyte DNA synthesis. *Circ Res*. 1998;83:15-26

39. Kajstura J, Leri A, Finato N, Di Loreto C, Beltrami CA, Anversa P. Myocyte proliferation in end-stage cardiac failure in humans. *Proc Natl Acad Sci U S A*. 1998;95:8801-8805

40. Laflamme MA, Murry CE. Regenerating the heart. *Nat Biotechnol*. 2005;23:845-856

41. Murry CE, Reinecke H, Pabon LM. Regeneration gaps: Observations on stem cells and cardiac repair. *J Am Coll Cardiol*. 2006;47:1777-1785

42. Hutchins GM, Bulkley BH. Infarct expansion versus extension: Two different complications of acute myocardial infarction. *Am J Cardiol*. 1978;41:1127-1132

43. Weisman HF, Bush DE, Mannisi JA, Weisfeldt ML, Healy B. Cellular mechanisms of myocardial infarct expansion. *Circulation*. 1988;78:186-201

44. Vracko R, Thorning D, Frederickson RG. Connective tissue cells in healing rat myocardium. A study of cell reactions in rhythmically contracting environment. *Am J Pathol*. 1989;134:993-1006

45. Pfeffer MA, Braunwald E. Ventricular remodeling after myocardial infarction. Experimental observations and clinical implications. *Circulation*. 1990;81:1161-1172

46. Braunwald E. Myocardial reperfusion, limitation of infarct size, reduction of left ventricular dysfunction, and improved survival. Should the paradigm be expanded? . *Circulation*. 1989;79:441-444

47. Cohn JN, Ferrari R, Sharpe N. Cardiac remodeling-concepts and clinical implications: A consensus paper from an international forum on cardiac remodeling. Behalf of an international forum on cardiac remodeling. *J Am Coll Cardiol*. 2000;35:569-582

48. Steg PG, Lopez-Sendon J, Lopez de Sa E, Goodman SG, Gore JM, Anderson FAJ, Himbert D, Allegrone J, Van de Werf F. External validity of clinical trials in acute myocardial infarction. *Arch Intern Med* 2007;167:68-73

49. Pfeffer MA, Braunwald E, Moye LA, Basta L, Brown EJ, Jr., Cuddy TE, Davis BR, Geltman EM, Goldman S, Flaker GC, et al. Effect of captopril on mortality and morbidity in patients with left ventricular dysfunction after myocardial infarction. Results of the survival and ventricular enlargement trial. The save investigators. *N Engl J Med*. 1992;327:669-677

50. Thygesen K, Alpert JS, White HD, Jaffe AS, Apple FS, Galvani M, Katus HA, Newby LK, Ravkilde J, Chaitman B, Clemmensen PM, Dellborg M,

Hod H, Porela P, Underwood R, Bax JJ, Beller GA, Bonow R, Van der Wall EE, Bassand JP, Wijns W, Ferguson TB, Steg PG, Uretsky BF, Williams DO, Armstrong PW, Antman EM, Fox KA, Hamm CW, Ohman EM, Simoons ML, Poole-Wilson PA, Gurfinkel EP, Lopez-Sendon JL, Pais P, Mendis S, Zhu JR, Wallentin LC, Fernandez-Aviles F, Fox KM, Parkhomenko AN, Priori SG, Tendera M, Voipio-Pulkki LM, Vahanian A, Camm AJ, De Caterina R, Dean V, Dickstein K, Filippatos G, Funck-Brentano C, Hellemans I, Kristensen SD, McGregor K, Sechtem U, Silber S, Widimsky P, Zamorano JL, Morais J, Brener S, Harrington R, Morrow D, Lim M, Martinez-Rios MA, Steinhubl S, Levine GN, Gibler WB, Goff D, Tubaro M, Dudek D, Al-Attar N. Universal definition of myocardial infarction. *Circulation*. 2007;116:2634-2653

51. Schuster A, Morton G, Chiribiri A, Perera D, Vanoverschelde JL, Nagel E. Imaging in the management of ischemic cardiomyopathy: Special focus on magnetic resonance. *J Am Coll Cardiol*. 2012;59:359-370
52. Kim HW, Farzaneh-Far A, Kim RJ. Cardiovascular magnetic resonance in patients with myocardial infarction: Current and emerging applications. *J Am Coll Cardiol*. 2009;55:1-16
53. Perazzolo Marra M, Lima JA, Iliceto S. Mri in acute myocardial infarction. *Eur Heart J*. 2011;32:284-293
54. Figtree GA, Lonborg J, Grieve SM, Ward MR, Bhindi R. Cardiac magnetic resonance imaging for the interventional cardiologist. *JACC Cardiovasc Interv*. 2011;4:137-148

55. Sosnovik DE, Nahrendorf M, Weissleder R. Molecular magnetic resonance imaging in cardiovascular medicine. *Circulation*. 2007;115:2076-2086

56. Sinusas AJ, Bengel F, Nahrendorf M, Epstein FH, Wu JC, Villanueva FS, Fayad ZA, Gropler RJ. Multimodality cardiovascular molecular imaging, part i. *Circ Cardiovasc Imaging*. 2008;1:244-256

57. Nahrendorf M, Sosnovik DE, French BA, Swirski FK, Bengel F, Sadeghi MM, Lindner JR, Wu JC, Kraitchman DL, Fayad ZA, Sinusas AJ. Multimodality cardiovascular molecular imaging, part ii. *Circ Cardiovasc Imaging*. 2009;2:56-70

58. Twieg DB. The k-trajectory formulation of the nmr imaging process with applications in analysis and synthesis of imaging methods. *Medical Physics*. 1983;10:610-621

59. Bloch F, Hansen WW, Packard M. Nuclear induction. *Phys Rev*. 1946;69:680-680

60. Purcell EM, Torrey HC, Pound RV. Resonance absorption by nuclear magnetic moments in a solid. *Phys Rev*. 1946;69:37-38

61. Haacke EM, Brown RW, Thompson MR, Venkatesan R. Magnetic resonance imaging, physical principles and sequence design. *A John Wiley and Sons*. 1999

62. Finn JP, Nael K, Deshpande V, Ratib O, Laub G. Cardiac mr imaging: State of the technology. *Radiology*. 2006;241:338-354

63. Verberne HJ, Dibbets-Schneider P, Spijkerboer A, Stokkel M, van Eck-Smit BL, Sokole EB. Multicenter intercomparison assessment of

consistency of left ventricular function from a gated cardiac spect phantom. *J Nucl Cardiol*. 2006;13:801-810

64. Vallejo E, Dione DP, Bruni WL, Constable RT, Borek PP, Soares JP, Carr JG, Condos SG, Wackers FJ, Sinusas AJ. Reproducibility and accuracy of gated spect for determination of left ventricular volumes and ejection fraction: Experimental validation using mri. *J Nucl Med.* 2000;41:874-882

65. Moon JC, Lorenz CH, Francis JM, Smith GC, Pennell DJ. Breath-hold flash and fisp cardiovascular mr imaging: Left ventricular volume differences and reproducibility. *Radiology*. 2002:789-797

66. Bellenger NG, Burgess MI, Ray SG, Lahiri A, Coats AJ, Cleland JG, Pennell DJ. Comparison of left ventricular ejection fraction and volumes in heart failure by echocardiography, radionuclide ventriculography and cardiovascular magnetic resonance; are they interchangeable? . *Eur Heart J*. 2000;21:1387-1396

67. Cerqueira MD, Weissman NJ, Dilsizian V, Jacobs AK, Kaul S, Laskey WK, Pennell DJ, Rumberger JA, Ryan T, Verani MS. Standardized myocardial segmentation and nomenclature for tomographic imaging of the heart: A statement for healthcare professionals from the cardiac imaging committee of the council on clinical cardiology of the american heart association. *Circulation*. 2002;105:539-542

68. Gerber BL, Rochitte CE, Melin JA, McVeigh ER, Bluemke DA, Wu KC, Becker LC, Lima JA. Microvascular obstruction and left ventricular remodeling early after acute myocardial infarction. *Circulation* 2000;101:2734-2741

69. Fishbein MC, J YR, Lando U, Kanmatsuse K, Mercier JC, Ganz W. The relationship of vascular injury and myocardial hemorrhage to necrosis after reperfusion. *Circulation*. 1980;62:1274-1279

70. Mather AN, Fairbairn TA, Ball SG, Greenwood JP, Plein S. Reperfusion haemorrhage as determined by cardiovascular mri is a predictor of adverse left ventricular remodelling and markers of late arrhythmic risk. *Heart*. 2011;97:453-459

71. Bekkers SC, Smulders MW, Passos VL, Leiner T, Waltenberger J, Gorgels AP, Schalla S. Clinical implications of microvascular obstruction and intramyocardial haemorrhage in acute myocardial infarction using cardiovascular magnetic resonance imaging. *Eur Radiol*. 2010;20:2572-2578

72. Ganame J, Messalli G, Dymarkowski S, Rademakers FE, Desmet W, Van de Werf F, Bogaert J. Impact of myocardial haemorrhage on left ventricular function and remodelling in patients with reperfused acute myocardial infarction. *Eur Heart J*. 2009;30:1440-1449

73. Bogaert J, Kalantzi M, Dymarkowski S, Janssens S. Importance of intramyocardial hemorrhage in acute myocardial infarction: Assessment with mri. *J. Cardiovasc Magn Reson*. 2006;8:76-77

74. Mahrholdt H, Wagner A, Holly TA, Elliott MD, Bonow RO, Kim RJ, Judd RM. Reproducibility of chronic infarct size measurement by contrast-enhanced magnetic resonance imaging. *Circulation* 2002;106

75. Wagner A, Mahrholdt H, Thomson L, Hager S, Meinhardt G, Rehwald W, Parker M, Shah D, Sechtem U, Kim RJ, Judd RM. Effects of time, dose, and inversion time for acute myocardial infarct size measurements based

on magnetic resonance imaging-delayed contrast enhancement. *J Am Coll Cardiol*. 2006;47:2027-2033

76. Wagner A, Mahrholdt H, Holly TA, Elliott MD, Regenfus M, Parker M, Klocke FJ, Bonow RO, Kim RJ, Judd RM. Contrast-enhanced mri and routine single photon emission computed tomography (spect) perfusion imaging for detection of subendocardial myocardial infarcts: An imaging study. *Lancet*. 2003;361:374-379

77. Simonetti OP KR, Fieno DS, Hillenbrand HB, Wu E, Bundy JM, Finn JP, Judd RM. An improved mr imaging technique for the visualization of myocardial infarction. *Radiology*. 2001;218:215-223

78. Bogaert J, Kalantzi M, Rademakers FE, Dymarkowski S, Janssens S. Determinants and impact of microvascular obstruction in successfully reperfused st-segment elevation myocardial infarction. Assessment by magnetic resonance imaging. *Eur Radiol*. 2007;17:2572-2580

79. Nijveldt R, Beek AM, Hirsch A, Stoel MG, Hofman MB, Umans VA, Algra PR, Twisk JW, van Rossum AC. Functional recovery after acute myocardial infarction: Comparison between angiography, electrocardiography, and cardiovascular magnetic resonance measures of microvascular injury. *J Am Coll Cardiol*. 2008;52:181-189

80. Husser O, Monmeneu JV, Sanchis J, Nunez J, Lopez-Lereu MP, Bonanad C, Chaustre F, Gomez C, Bosch MJ, Hinarejos R, Chorro FJ, Riegger GA, Llacer A, Bodi V. Cardiovascular magnetic resonance-derived intramyocardial hemorrhage after stemi: Influence on long-term prognosis, adverse left ventricular remodeling and relationship with microvascular obstruction. *Int J Cardiol* 2012;

http://dx.doi.org/10.1016/j.ijcard.2012.05.055

81. Ochiai K, Shimada T, Murakami Y, Ishibashi Y, Sano K, Kitamura J, Inoue S, Murakami R, Kawamitsu H, Sugimura K. Hemorrhagic myocardial infarction after coronary reperfusion detected in vivo by magnetic resonance imaging in humans: Prevalence and clinical implications. . *J Cardiovasc Magn Reson* 1999;1:247-256

82. Aletras AH, Tilak GS, Natanzon A, Hsu LY, Gonzalez FM, Hoyt RFJ, Arai AE. Retrospective determination of the area at risk for reperfused acute myocardial infarction with t2-weighted cardiac magnetic resonance imaging: Histopathological and displacement encoding with stimulated echoes (dense) functional validations. *Circulation*. 2006;113:1865-1870

83. Jugdutt BI. Ventricular remodeling after infarction and the extracellular collagen matrix: When is enough enough? . *Circulation*. 2003;108:1395-1403

84. Jacobs RE, Fraser SE. Magnetic resonance microscopy of embryonic cell lineages and movements. *Science* 1994;263:681-684

85. Modo M, Cash D, Mellodew K, Williams SC, Fraser SE, Meade TJ, Price J, Hodges H. Tracking transplanted stem cell migration using bifunctional, contrast agent-enhanced, magnetic resonance imaging. *Neuroimage* 2002;17:803-811

86. Modo M, Mellodew K, Cash D, Fraser SE, Meade TJ, Price J, Williams SC. Mapping transplanted stem cell migration after a stroke: A serial, in vivo magnetic resonance imaging study. *Neuroimage* 2004;21:311-317

87. Aime S, Barge A, Cabella C, Crich SG, Gianolio E. Targeting cells with mr imaging probes based on paramagnetic gd(iii) chelates. *Curr Pharm Biotechnol*. 2004;5:509-518

88. Daldrup-Link HE, Rudelius M, Metz S, Piontek G, Pichler B, Settles M, Heinzmann U, Schlegel J, Oostendorp RA, Rummeny EJ. Cell tracking with gadophrin-2: A bifunctional contrast agent for mr imaging, optical imaging, and fluorescence microscopy. *Eur J Nucl Med Mol Imaging*. 2004;31

89. Aoki I, Takahashi Y, Chuang KH, Silva AC, Igarashi T, Tanaka C, Childs RW, Koretsky AP. Cell labeling for magnetic resonance imaging with the t1 agent manganese chloride. *NMR Biomed*. 2006;19:50-59

90. Tannous B, Grimm J, Perry KF, Chen JW, Weissleder R, Breakefield XO. Metabolic biotinylation of cell surface receptors for in vivo imaging. *Nat Methods*. 2006;3:391-396

91. Cohen B, Dafni H, Meir G, Harmelin A, Neeman M. Ferritin as an endogenous mri reporter for noninvasive imaging of gene expression in c6 glioma tumors. *Neoplasia*. 2005;7:109-117

92. Genove G, DeMarco U, Xu H, Goins WF, Ahrens ET. A new transgene reporter for in vivo magnetic resonance imaging. *Nat Med*. 2005;11:450-454

93. Gilad AA, McMahon MT, Walczak P, Winnard PTJ, Raman V, van Laarhoven HW, Skoglund CM, Bulte JW, van Zijl PC. Artificial reporter gene providing mri contrast based on proton exchange. *Nat Biotechnol*. 2007;25:217-219

94. Ahrens ET, Flores R, Xu H, Morel PA. In vivo imaging platform for tracking immunotherapeutic cells. *Nat Biotechnol*. 2005;23:983-987

95. Corot C, Robert P, Idee JM, Port M. Recent advances in iron oxide nanocrystal technology for medical imaging. *Adv Drug Deliv Rev*. 2006;58:1471-1504

96. Stuckey DJ, Carr CA, Martin-Rendon E, Tyler DJ, Willmott C, Cassidy PJ, Hale SJ, Schneider JE, Tatton L, Harding SE. Iron particles for noninvasive monitoring of bone marrow stromal cell engraftment into, and isolation of viable engrafted donor cells from, the heart. *Stem Cells* 2006;24:1968-1975

97. McLachlan SJ, Morris MR, Lucas MA, Fisco RA, Eakins MN, Fowler DR, Scheetz RB, Olukotun AY. Phase i clinical evaluation of a new iron oxide mr contrast agent. *J Magn Reson Imaging* 1994;4:301-307

98. Li W, Tutton S, Vu A, Pierchala L, Li BS, Lewis JM, Prasad PV, Edelman RR. First-pass contrast-enhanced magnetic resonance angiography in humans using ferumoxytol, a novel ultrasmall superparamagnetic iron oxide (uspio)-based blood pool agent. *J Magn Reson Imaging*. 2005;21:46-52

99. Clement O, Siauve N, Cuenod CA, Frija G. Liver imaging with ferumoxides (feridex): Fundamentals, controversies, and practical aspects. *Top Magn Reson Imaging*. 1998;9:167-182

100. Reimer P, Marx C, Rummeny EJ, Muller M, Lentschig M, Balzer T, Dietl KH, Sulkowski U, Berns T, Shamsi K. Spio-enhanced 2d-tof mr angiography of the portal venous system: Results of an intraindividual comparison. *J Magn Reson Imaging*. 1997;7:945-949

101. Shapiro EM, Skrtic S, Koretsky AP. Sizing it up: Cellular mri using micron-sized iron oxide particles. *Magn Reson Med*. 2005;53:329-338

102. Reimer P, Tombach B. Hepatic mri with spio: Detection and characterization of focal liver lesions. *Eur Radiol*. 1998;8:1198-1204

103. Reimer P, Tombach B. Hepatic mri with spio: Detection and characterization of focal liver lesions. *Eur Radiol* 1998;8:1198-1204

104. Dardzinski BJ, Schmithorst VJ, Holland SK, Boivin GP, Imagawa T, Watanabe S, Lewis JM, Hirsch R. Mr imaging of murine arthritis using ultrasmall superparamagnetic iron oxide particles. *Magn Reson Imaging*. 2001;19:1209-1216

105. Turetschek K, Roberts TP, Floyd E, Preda A, Novikov V, Shames DM, Carter WO, Brasch RC. Tumor microvascular characterization using ultrasmall superparamagnetic iron oxide particles (uspio) in an experimental breast cancer model. *J Magn Reson Imaging*. 2001;13:882-888

106. Berry I, Benderbous S, Ranjeva JP, Gracia-Meavilla D, Manelfe C, Le Bihan D. Contribution of sinerem used as blood-pool contrast agent: Detection of cerebral blood volume changes during apnea in the rabbit. *Magn Reson Med*. 1996;36:415-419

107. Heyn C, Ronald JA, Ramadan SS, Snir JA, Barry AM, MacKenzie LT, Mikulis DJ, Palmieri D, Bronder JL, Steeg PS. In vivo mri of cancer cell fate at the single-cell level in a mouse model of breast cancer metastasis to the brain. *Magn Reson Med*. 2006;56:1001-1010

108. Hombach V, Grebe O, Merkle N, Waldenmaier S, Hoher M, Kochs M, Wohrle J, Kestler HA. Sequelae of acute myocardial infarction regarding

cardiac structure and function and their prognostic significance as assessed by magnetic resonance imaging. *Eur Heart J.* 2005;26:549-557

109. Albert TS, Kim RJ, Judd RM. Assessment of no-reflow regions using cardiac mri. *Basic Res Cardiol.* 2006;101:383-390

110. Tarantini G, Cacciavillani L, Corbetti F, Ramondo A, Marra MP, Bacchiega E, Napodano M, Bilato C, Razzolini R, Iliceto S. Duration of ischemia is a major determinant of transmurality and severe microvascular obstruction after primary angioplasty: A study performed with contrast-enhanced magnetic resonance *J Am Coll Cardiol* 2005;46:1229-1235

111. van den Bos EJ, Baks T, Moelker AD, Kerver W, van Geuns RJ, van der Giessen WJ, Duncker DJ, Wielopolski PA. Magnetic resonance imaging of haemorrhage within reperfused myocardial infarcts: Possible interference with iron oxide-labelled cell tracking? *Eur Heart J.* 2006;27:1620-1626

112. Kraitchman DL, Heldman AW, Atalar E, Amado LC, Martin BJ, Pittenger MF, Hare JM, Bulte JW. In vivo magnetic resonance imaging of mesenchymal stem cells in myocardial infarction. *Circulation* 2003;107:2290-2293

113. Kustermann E, Roell W, Breitbach M, Wecker S, Wiedermann D, Buehrle C, Welz A, Hescheler J, Fleischmann BK, Hoehn M. Stem cell implantation in ischemic mouse heart: A high-resolution magnetic resonance imaging investigation. *NMR Biomed.* 2005;18:362-370

114. Tallheden T, Nannmark U, Lorentzon M, Rakotonirainy O, Soussi B, Waagstein F, Jeppsson A, Sjogren-Jansson E, Lindahl A, Omerovic E. In

vivo mr imaging of magnetically labeled human embryonic stem cells. *Life Sci* 2006;79:999-1006

115. Ahrens ET, Flores R, Xu H, Morel P. In vivo imaging platform for tracking immunotherapeutic cells. *Nat Biotechnol*. 2005;23:983-987

116. Bulte JW. Hot spot mri emerges from the background. *Nat Biotechnol*. 2005;23:945-946

117. Partlow KC, Chen J, Brant JA, Neubauer AM, Meyerrose TE, Creer MH, Nolta JA, Caruthers SD, Lanza GM, Wickline SA. 19f magnetic resonance imaging for stem/progenitor cell tracking with multiple unique perfluorocarbon nanobeacons. *FASEB J*. 2007;21:1647-1654

118. McNab JA, Yung AC, Kozlowski P. Tissue oxygen tension measurements in the shionogi model of prostate cancer using 19f mrs and mri. *Magma* 2004;17:288-295

119. Riess JG. Perfluorocarbon-based oxygen delivery. *Artif Cells Blood Substit Immobil Biotechnol*. 2006;34:567-580

120. Noth U, Morrissey SP, Deichmann R, Jung S, Adolf H, Haase A, Lutz J. Perfluoro-15-crown-5-ether labelled macrophages in adoptive transfer experimental allergic encephalomyelitis. *Artif Cells Blood Substit Immobil Biotechnol*. 1997;25:243-254

121. Flogel U, Ding Z, Hardung H, Jander S, Reichmann G, Jacoby C, Schubert R, Schrader J. In vivo monitoring of inflammation after cardiac and cerebral ischemia by fluorine magnetic resonance imaging. *Circulation*. 2008;118:140-148

122. Ebner B, Behm P, Jacoby C, Burghoff S, French BA, Schrader J, Flogel U. Early assessment of pulmonary inflammation by 19F MRI in vivo. *Circ Cardiovasc Imaging*. 2010;3:202-210

123. Flogel U, Su S, Kreideweiss I, Ding Z, Galbarz L, Fu J, Jacoby C, Witzke O, Schrader J. Noninvasive detection of graft rejection by in vivo(19) f mri in the early stage. *Am J Transplant*. 2011

124. Srinivas M, Morel PA, Ernst LA, Laidlaw DH, Ahrens ET. Fluorine-19 mri for visualization and quantification of cell migration in a diabetes model. *Magn Reson Med*. 2007;58:725-734

125. Ruiz-Cabello J, Walczak P, Kedziorek DA, Chacko VP, Schmieder AH, Wickline SA, Lanza GM, Bulte JW. In vivo "hot spot" mr imaging of neural stem cells using fluorinated nanoparticles. *Magn Reson Med*. 2008;60:1506-1511

126. Metz S, Bonaterra G, Rudelius M, Settles M, Rummeny EJ, Daldrup-Link HE. Capacity of human monocytes to phagocytose approved iron oxide mr contrast agents in vitro. *Eur Radiol* 2004;14:1851-1858

127. Fleige G, Seeberger F, Laux D, Kresse M, Taupitz M, Pilgrimm H, Zimmer C. In vitro characterization of two different ultrasmall iron oxide particles for magnetic resonance cell tracking. *Invest Radiol*. 2002;37:482-488

128. Frank JA, Anderson SA, Kalsih H, Jordan EK, Lewis BK, Yocum GT, Arbab AS. Methods for magnetically labeling stem and other cells for detection by in vivo magnetic resonance imaging. *Cytotherapy*. 2004;6

129. Thu MS, Bryant LH, Coppola T, Jordan EK, Budde MD, Lewis BK, Chaudhry A, Ren J, Varma NR, Arbab AS, Frank JA. Self-assembling

nanocomplexes by combining ferumoxytol, heparin and protamine for cell tracking by magnetic resonance imaging. *Nat Med*. 2012;18:463-467

130. Kostura L, Kraitchman DL, Mackay AM, Pittenger MF, Bulte JW. Feridex labeling of mesenchymal stem cells inhibits chondrogenesis but not adipogenesis or osteogenesis. *NMR Biomed*. 2004;17:513-517

131. Arbab AS, Yocum GT, Rad AM, Khakoo AY, Fellowes V, Read EJ, Frank JA. Labeling of cells with ferumoxides-protamine sulfate complexes does not inhibit function or differentiation capacity of hematopoietic or mesenchymal stem cells. *NMR Biomed*. 2005;18:553-559

132. Bulte JW, Kraitchman DL, Mackay AM, Pittenger MF. Chondrogenic differentiation of mesenchymal stem cells is inhibited after magnetic labeling with ferumoxides. *Blood*. 2004;104:3410-3412; author reply 3412-3413

133. Bulte JW, Zhang S, van Gelderen P, Herynek V, Jordan EK, Duncan ID, Frank JA. Neurotransplantation of magnetically labeled oligodendrocyte progenitors: Magnetic resonance tracking of cell migration and myelination. *Proc Natl Acad Sci USA*. 1999;96:15256-15261

134. Walczak P, Kedziorek DA, Gilad AA, Lin S, Bulte JW. Instant mr labeling of stem cells using magnetoelectroporation. *Magn Reson Med*. 2005;54:769-774

135. Walczak P, Ruiz-Cabello J, Kedziorek DA, Gilad AA, Lin S, Barnett B, Qin L, Levitsky H, Bulte JW. Magnetoelectroporation: Improved labeling of neural stem cells and leukocytes for cellular magnetic resonance imaging using a single fda-approved agent. *Nanomedicine*. 2006;2:89-94

136. Suzuki Y, Zhang S, Kundu P, Yeung AC, Robbins RC, Yang PC. In vitro comparison of the biological effects of three transfection methods for magnetically labeling mouse embryonic stem cells with ferumoxides. *Magn Reson Med* 2007;57:1173-1179

137. Stroh A, Faber C, Neuberger T, Lorenz P, Sieland K, Jakob PM, Webb A, Pilgrimm H, Schober R, Pohl EE. In vivo detection limits of magnetically labeled embryonic stem cells in the rat brain using high-field (17.6 t) magnetic resonance imaging. *Neuroimage* 2005;24:635-645

138. Wu YL, Ye Q, Foley LM, Hitchens TK, Sato K, Williams JB, Ho C. In situ labeling of immune cells with iron oxide particles: An approach to detect organ rejection by cellular mri. *Proc Natl Acad Sci USA* 2006;103:1852-1857

139. Baklanov DV, Demuinck ED, Thompson CA, Pearlman JD. Novel double contrast mri technique for intramyocardial detection of percutaneously transplanted autologous cells. *Magn Reson Med*. 2004;52:1438-1442

140. Kraitchman DL, Tatsumi M, Gilson WD, Ishimori T, Kedziorek D, Walczak P, Segars WP, Chen HH, Fritzges D, Izbudak I. Dynamic imaging of allogeneic mesenchymal stem cells trafficking to myocardial infarction. *Circulation*. 2005;112:1451-1461

141. Mani V, Briley-Saebo KC, Itskovich V, Samber DD, Fayad ZA. Gradient echo acquisition for superparamagnetic particles with positive contrast (grasp): Sequence characterization in membrane and glass superparamagnetic iron oxide phantoms at 1.5t and 3t. *Magn Reson Med* 2006;55

142. Cunningham CH, Arai T, Yang PC, McConnell MV, Pauly JM, Conolly SM. Positive contrast magnetic resonance imaging of cells labeled with magnetic nanoparticles. *Magn Reson Med*. 2005;53:999-1005

143. Nahrendorf M, Sosnovik D, Chen JW, Panizzi P, Figueiredo JL, Aikawa E, Libby P, Swirski FK, Weissleder R. Activatable magnetic resonance imaging agent reports myeloperoxidase activity in healing infarcts and noninvasively detects the antiinflammatory effects of atorvastatin on ischemia-reperfusion injury. *Circulation*. 2008;117:1153-1160

144. Spuentrup E, Buecker A, Katoh M, Wiethoff AJ, Parsons EC, Jr., Botnar RM, Weisskoff RM, Graham PB, Manning WJ, Gunther RW. Molecular magnetic resonance imaging of coronary thrombosis and pulmonary emboli with a novel fibrin-targeted contrast agent. *Circulation*. 2005;111:1377-1382

145. Sirol M, Fuster V, Badimon JJ, Fallon JT, Moreno PR, Toussaint JF, Fayad ZA. Chronic thrombus detection with in vivo magnetic resonance imaging and a fibrin-targeted contrast agent. *Circulation*. 2005;112:1594-1600

146. Sosnovik DE, Schellenberger EA, Nahrendorf M, Novikov MS, Matsui T, Dai G, Reynolds F, Grazette L, Rosenzweig A, Weissleder R, Josephson L. Magnetic resonance imaging of cardiomyocyte apoptosis with a novel magneto-optical nanoparticle. *Magn Reson Med*. 2005;54:718-724

147. Helm PA, Caravan P, French BA, Jacques V, Shen L, Xu Y, Beyers RJ, Roy RJ, Kramer CM, Epstein FH. Postinfarction myocardial scarring in mice: Molecular mr imaging with use of a collagen-targeting contrast agent. *Radiology*. 2008;247:788-796

148. Su HS, Nahrendorf M, Panizzi P, Breckwoldt MO, Rodriguez E, Iwamoto Y, Aikawa E, Weissleder R, Chen JW. Vasculitis: Molecular imaging by targeting the inflammatory enzyme myeloperoxidase. *Radiology*. 2012;262:181-190

149. Oostendorp M, Douma K, Wagenaar A, Slenter JM, Hackeng TM, van Zandvoort MA, Post MJ, Backes WH. Molecular magnetic resonance imaging of myocardial angiogenesis after acute myocardial infarction. *Circulation*. 2010;121:775-783

150. Cheung JY, Bonventre JV, Malis CD, Leaf A. Calcium and ischemic injury. *N Engl J Med*. 1986;314:1670-1676

151. Ochi R. The slow inward current and the action of manganese ions in guinea-pig's myocardium. *Pflugers Arch*. 1970;316:81-94

152. Hunter DR, Haworth RA, Berkoff HA. Cellular manganese uptake by the isolated perfused rat heart: A probe for the sarcolemma calcium channel. *J Mol Cell Cardiol*. 1981;13:823-832

153. Waghorn B, Edwards T, Yang Y, Chuang KH, Yanasak N, Hu TC. Monitoring dynamic alterations in calcium homeostasis by t (1)-weighted and t (1)-mapping cardiac manganese-enhanced mri in a murine myocardial infarction model. *NMR Biomed*. 2008;21:1102-1111

154. Krombach GA, Saeed M, Higgins CB, Novikov V, Wendland MF. Contrast-enhanced mr delineation of stunned myocardium with administration of mncl(2) in rats. *Radiology*. 2004;230:183-190

155. Bremerich J, Saeed M, Arheden H, Higgins CB, Wendland MF. Normal and infarcted myocardium: Differentiation with cellular uptake of manganese at mr imaging in a rat model. *Radiology*. 2000;216:524-530

156. Delattre BMA, Braunersreuther V, Gardier S, Hyacinthe JN, Crowe LA, Mach F, Vallee JP. Manganese kinetics demonstrated double contrast in acute but not in chronic infarction in a mouse model of myocardial occlusion reperfusion. *Nmr in Biomedicine*. 2012;25:489-497

157. Hu TC, Pautler RG, MacGowan GA, Koretsky AP. Manganese-enhanced mri of mouse heart during changes in inotropy. *Magn Reson Med*. 2001;46:884-890

158. Waghorn B, Yang Y, Baba A, Matsuda T, Schumacher A, Yanasak N, Hu TC. Assessing manganese efflux using sea0400 and cardiac t1-mapping manganese-enhanced mri in a murine model. *NMR Biomed*. 2009;22:874-881

159. Panizzi P, Swirski FK, Figueiredo JL, Waterman P, Sosnovik DE, Aikawa E, Libby P, Pittet M, Weissleder R, Nahrendorf M. Impaired infarct healing in atherosclerotic mice with ly-6c(hi) monocytosis. *J Am Coll Cardiol*. 2010;55:1629-1638

160. O'Regan DP, Ahmed R, Karunanithy N, Neuwirth C, Tan Y, Durighel G, Hajnal JV, Nadra I, Corbett SJ, Cook SA. Reperfusion hemorrhage following acute myocardial infarction: Assessment with t2* mapping and effect on measuring the area at risk. *Radiology*. 2009;250:916-922

161. Asanuma T, Tanabe K, Ochiai K, Yoshitomi H, Nakamura K, Murakami Y, Sano K, Shimada T, Murakami R, Morioka S, Beppu S. Relationship between progressive microvascular damage and intramyocardial hemorrhage in patients with reperfused anterior myocardial infarction: Myocardial contrast echocardiographic study. *Circulation*. 1997;96:448-453

162. Niccoli G, Burzotta F, Galiuto L, Crea F. Myocardial no-reflow in humans. *J Am Coll Cardiol*. 2009;54:281-292

163. Ye Y, Bogaert J. Cell therapy in myocardial infarction: Emphasis on the role of mri. *Eur Radiol*. 2008;18:548-569

164. Rich L, Whittaker P. Collagen and picrosirius red staining: A polarized light assessment of fibrillar hue and spatial distribution. *Braz. J. morphol. Sci*. 2005;22:97-104

165. Shapiro EM, Skrtic S, Sharer K, Hill JM, Dunbar CE, Koretsky AP. Mri detection of single particles for cellular imaging. *Proc Natl Acad Sci U S A*. 2004;101:10901-10906

166. Janjic JM, Srinivas M, Kadayakkara DK, Ahrens ET. Self-delivering nanoemulsions for dual fluorine-19 mri and fluorescence detection. *J Am Chem Soc*. 2008;130:2832-2841

167. Lotan CS, Bouchard A, Cranney GB, Bishop SP, Pohost GM. Assessment of postreperfusion myocardial hemorrhage using proton nmr imaging at 1.5 t. *Circulation*. 1992;86:1018-1025

168. Kloner RA, Ellis SG, Lange R, Braunwald E. Studies of experimental coronary artery reperfusion. Effects on infarct size, myocardial function, biochemistry, ultrastructure and microvascular damage. *Circulation*. 1983;68:I8-15

169. Bulkley BH, Roberts WC. Steroid therapy during acute myocardial infarction. A cause of delayed healing and of ventricular aneurysm. *Am J Med*. 1974;56:244-250

170. Fishbein MC, Maclean D, Maroko PR. Experimental myocardial infarction in the rat: Qualitative and quantitative changes during pathologic evolution. *Am J Pathol*. 1978;90:57-70

171. Sutton MG, Sharpe N. Left ventricular remodeling after myocardial infarction: Pathophysiology and therapy. *Circulation*. 2000;101:2981-2988

172. van Amerongen MJ, Harmsen MC, van Rooijen N, Petersen AH, van Luyn MJ. Macrophage depletion impairs wound healing and increases left ventricular remodeling after myocardial injury in mice. *Am J Pathol*. 2007;170:818-829

173. Jaffe R, Dick A, Strauss BH. Prevention and treatment of microvascular obstruction-related myocardial injury and coronary no-reflow following percutaneous coronary intervention: A systematic approach. *JACC Cardiovasc Interv*. 2010;3:695-704

174. O'Regan DP, Ariff B, Neuwirth C, Tan Y, Durighel G, Cook SA. Assessment of severe reperfusion injury with t2* cardiac mri in patients with acute myocardial infarction. *Heart*. 2010;96:1885-1891

175. Higginson LA, White F, Heggtveit HA, Sanders TM, Bloor CM, Covell JW. Determinants of myocardial hemorrhage after coronary reperfusion in the anesthetized dog. *Circulation*. 1982;65:62-69

176. Barry WH, Bridge JH. Intracellular calcium homeostasis in cardiac myocytes. *Circulation*. 1993;87:1806-1815

177. Bolli R. Mechanism of myocardial "stunning". *Circulation*. 1990;82:723-738

178. Bito V, Heinzel FR, Weidemann F, Dommke C, van der Velden J, Verbeken E, Claus P, Bijnens B, De Scheerder I, Stienen GJ, Sutherland GR, Sipido KR. Cellular mechanisms of contractile dysfunction in hibernating myocardium. *Circ Res*. 2004;94:794-801

179. Bodi I, Mikala G, Koch SE, Akhter SA, Schwartz A. The l-type calcium channel in the heart: The beat goes on. *J Clin Invest*. 2005;115:3306-3317

180. Mendoncadias MH, Gaggelli E, Lauterbur PC. Paramagnetic contrast agents in nuclear magnetic-resonance medical imaging. *Semin Nucl Med*. 1983;13:364-376

181. Hu TC, Chuang KH, Yanasak N, Koretsky A. Relationship between blood and myocardium manganese levels during manganese-enhanced mri (memri) with t(1) mapping in rats. *NMR Biomed*. 2010

182. Brady TJ, Goldman MR, Pykett IL, Buonanno FS, Kistler JP, Newhouse JH, Burt CT, Hinshaw WS, Pohost GM. Proton nuclear magnetic resonance imaging of regionally ischemic canine hearts: Effect of paramagnetic proton signal enhancement. *Radiology*. 1982;144:343-347

183. Goldman MR, Brady TJ, Pykett IL, Burt CT, Buonanno FS, Kistler JP, Newhouse JH, Hinshaw WS, Pohost GM. Quantification of experimental myocardial infarction using nuclear magnetic resonance imaging and paramagnetic ion contrast enhancement in excised canine hearts. *Circulation*. 1982;66:1012-1016

184. Pomeroy OH, Wendland M, Wagner S, Derugin N, Holt WW, Rocklage SM, Quay S, Higgins CB. Magnetic resonance imaging of acute myocardial ischemia using a manganese chelate, mn-dpdp. *Invest Radiol*. 1989;24:531-536

185. Skjold A, Amundsen BH, Wiseth R, Stoylen A, Haraldseth O, Larsson HB, Jynge P. Manganese dipyridoxyl-diphosphate (mndpdp) as a viability marker in patients with myocardial infarction. *J Magn Reson Imaging*. 2007;26:720-727

186. Paul C Lauterbur MHMD, Andrew M Rudin. Augmentation of tissue water proton spin-lattice relaxation rates by in vivo addition of paramagnetic ions. *Front Biol Energ Pap Int Symp*. 1978;1:8

187. Waller C, Kahler E, Hiller KH, Hu K, Nahrendorf M, Voll S, Haase A, Ertl G, Bauer WR. Myocardial perfusion and intracapillary blood volume in rats at rest and with coronary dilatation: Mr imaging in vivo with use of a spin-labeling technique. *Radiology*. 2000;215:189-197

188. Deichmann R, Haase A. Quantification of t1 values by snapshot-flash nmr imaging. *Journal of Magnetic Resonance*. 1992;96:608-612

189. Atkins HL, Som P, Fairchild RG, Hui J, Schachner E, Goldman A, Ku T. Myocardial positron tomography with manganese-52m. *Radiology*. 1979;133:769-774

190. Mendonca-Dias MH, Gaggelli E, Lauterbur PC. Paramagnetic contrast agents in nuclear magnetic resonance medical imaging. *Semin Nucl Med*. 1983;13:364-376

191. Storey P, Danias PG, Post M, Li W, Seoane PR, Harnish PP, Edelman RR, Prasad PV. Preliminary evaluation of evp 1001-1: A new cardiac-specific magnetic resonance contrast agent with kinetics suitable for steady-state imaging of the ischemic heart. *Invest Radiol*. 2003;38:642-652

Acknowledgements

Pursuing this doctorate in the past years is an important chapter of my life and career. On the last page of it, I would like to express my gratitude to those people who made this possible and unforgettable.

First of all, I would like to thank my supervisors, Prof. Dr. Dr. Wolfgang R. Bauer, Prof. Dr. Peter M. Jakob and Prof. Dr. Roland Jahns. They gave me the opportunity to perform my doctoral research in their laboratories, provided valuable advice and guidance on my research and career development. Particularly, I am grateful that they trusted me and always gave me enormous freedom to pursue my scientific interests.

In addition, thanks to my dear colleagues who supported the research. Xavier Helluy, Thomas C. Basse-Luesebrink and Thomas Kampf helped tremendously in MR physics, computer programming and data analysis. I benefited from insightful discussions with them and I was inspired by their great enthusiasm for MR research. Elisabeth Bauer offered her expertise in histology and immunohistochemistry. Paula Arias generously spent time to perform animal operations for my projects, as well as helped me to set up important methods. Vladimir Kocoski set up the protocol of flow cytometry experiments and trained me to perform the experiments and data analysis. Yuejiang Liang helped with the particle size measurements. Gang Qiang did fluorescent confocal microscopy. Stefanie Sparka helped in NMR experiments. Philipp Kagerbauer and Sonngard Vay both offered great assistance in my experiments. Sabine Voll has always been supportive in providing creative technical assistance. Many experiments might not have been done without her excellent organizing skills. Moreover, I'm thankful for Dr. Andreas Beilhack for his generosity in allowing me access to facilities in his lab. Thanks to Anagha Deshmane for proof-reading the summary of this thesis. Natalja Damatova, Sabine Voll and Alexander Gotschy kindly helped to translate it into German.

I feel very fortunate to have dear friends accompanying me through this journey. Thanks to Paola Ponce, Natalja Damatova, Anna Vita, Jochen Schmieg, Daniel Neumann, Valerie Jahns, Angela Schlipp, Marta Michalska, Zuoquan Zhang, Weifeng Liu, Pengtao Sun, Fei Gao and so many others. The friendship with you made this adventure so much enjoyable and cherishable. Special thanks give to Siping Tan, who introduced me to the fascinating world of experimental radiology and encouraged me to pursue an academic career in medical imaging, when I was a junior resident in radiology. I would also like to thank Min Zou, who has influenced me profoundly.

Finally, I would like to thank my parents, Zhuohong and Zhiqi, and my sister, Weiwei, for their love, understanding, encouragement and constant support. They always believe in me and give me absolute freedom to pursue my dreams since I was a child. This is invaluable and probably the best gift from them.

Affidavit

I hereby confirm that my thesis entitled Molekulare und zelluläre Magnetresonanztomographie der Wundheilung nach Myokardinfarkt (in German)/ Molecular and Cellular Magnetic Resonance Imaging of Myocardial Infarct Healing (in English) is the result of my own work. I did not receive any help or support from commercial consultants. All sources and / or materials applied are listed and specified in the thesis.

Furthermore, I confirm that this thesis has not yet been submitted as part of another examination process neither in identical nor in similar form.

Wuerzburg, 08.08.2012
Place, Date Signature

Eidesstattliche Erklärung

Hiermit erkläre ich an Eides statt, die Dissertation Molekulare und zelluläre Magnetresonanztomographie der Wundheilung nach Myokardinfarkt (in German)/ Molecular and Cellular Magnetic Resonance Imaging of Myocardial Infarct Healing (in English) eigenständig, d.h. insbesondere selbständig und ohne Hilfe eines kommerziellen Promotionsberaters, angefertigt und keine anderen als die von mir angegebenen Quellen und Hilfsmittel verwendet zu haben.

Ich erkläre außerdem, dass die Dissertation weder in gleicher noch in ähnlicher Form bereits in einem anderen Prüfungsverfahren vorgelegen hat.

Wuerzburg, 08.08.2012
Ort, Datum Unterschrift